ABSTRACT

Title of Document: CHARACTERIZATION OF FLUORESCENCE FROM QUANTUM DOTS ON NANOSTRUCTURED METAL SURFACES

Ehren Hwang, Ph.D., 2011

Directed By: Professor Christopher C. Davis, Department of Electrical and Computer Engineering

The behavior of fluorescent materials coupled to surface plasmon supporting surfaces and structures is an area of active research due to their fluorescence enhancing properties. The inherent field enhancements present near structures and interfaces where surface plasmons are excited provide great potential for increasing the response of many optical interactions. While many studies focus on the application of plasmonic nanoparticles or finite metallic structures the use of dielectric structures on a continuous metallic film has received little attention. A comprehensive experimental study using dielectric gratings on gold films is presented illustrating the fundamental properties of fluorescence enhancement on such structures. A process for fabrication of samples using Electron Beam Lithography is demonstrated and comparisons between various quantum dot deposition methods are made to determine the best conditions for surface coating. Conditions for optimization of the fluorescence enhancement phenomena for practical application are explored for

gratings with square function profile illustrating the influence of gratings on fluorescence behavior and identifying conditions for optimal enhancement. Complementing these results, an understanding of the underlying physical phenomena is developed by differentiation between enhanced emission and enhanced absorption effects using measurements of fluorescence decay lifetime and emission spectra. Using these observations a thorough description of these systems and the requirements for their practical application is illustrated.

CHARACTERIZATION OF FLUORESCENCE FROM QUANTUM DOTS ON NANOSTRUCTURED METAL SURFACES

By

Ehren Hwang

Dissertation submitted to the Faculty of the Graduate School of the
University of Maryland, College Park, in partial fulfillment
of the requirements for the degree of
Doctor of Philosophy
2011

Advisory Committee:
Professor Christopher C. Davis, Chair
Professor Mario Dagenais
Professor Martin Peckerar
Professor Edo Waks
Professor H. Dennis Drew

This thesis is dedicated in memory of Carolyn Wands
who took me under her wing as a child just like her own son.
She taught me life, love, and the belief that I could accomplish anything.

Acknowledgements

The road to completing this thesis has been long and involved and has been made possible in part by contributions from many others besides myself. While it would be difficult to recognize everyone who has influenced this work in some way I would like to take this time to acknowledge some of those who have played a significant role in creating this work.

First and foremost I want to thank my advisor Professor Christopher C. Davis without whom the entirety of this work would not have been possible. His insight and dedication to the education and welfare of his students are unparalleled and I have been most fortunate to have him as a mentor in these past years. It is not possible to thank him enough for taking in a wayward graduate student like myself and guiding him through the trials and tribulations of doctorate study to this final outcome. This is not to mention the monumental amount of patience such a task must have required when referring to this particular student. I wish him the best of luck in his continuing research endeavors for many years to come.

I would also like to thank Dr. Igor I. Smolyaninov who has sadly left our group to pursue a more lucrative career at BAE Systems. The design and interpretation of the experimental results were greatly influenced by his observations and his contribution to the work was indispensable. I hope that he enjoys continued success in his new career and look forward to seeing what kind of novel concepts he has to present in the future.

No acknowledgements would be complete without my parents, and our close friend Carolyn Wands, who have raised me and supported my academic endeavors. It is unfortunate that she has passed away recently but I believe she would have been proud to see these results. None of this would have been possible without the strong foundation of values and the drive for achievement which they have all instilled into me. I would also like to thank my girlfriend, the love of my life, for her support and patience throughout the course of my degree.

As the majority of the work presented here has been executed in the cleanroom and SEM imaging facilities I would like to express my profound gratitude for the assistance I have received from the Maryland Nanocenter staff. From the Fablab facility I would like to thank Jonathan A. Hummel, Thomas Loughran, John Abrahams, and James O'Connor for their insight into many of the microfabrication related obstacles which I have encountered throughout this work as well as many productive conversations over lunch. I believe they will breathe a sigh of relief that they can finally enjoy their lunch in peace and wish them the best. Additionally, I want to express my gratitude to Larry Lai from NISPLab for his assistance in scheduling and operation of the SU70 SEM which allowed me to performed detailed characterization of my samples.

Various aspects of the work I have done during my tenure here have involved a significant amount of machining to develop mechanical apparatus. I would like to thank John Rzasa from our lab along with John "J" Pyle at the IREAP machine shop for helping me to design and fabricate many of the fixtures used in the experiments. On a more personal note, developing the skills necessary to do high quality

fabrication in the machine shop would not have been possible for me without the assistance of Dr. Stephen Henderson who took time from his personal agenda to share his knowledge and enthusiasm for mechanical fabrication with me. I would like to thank him and wish him the best of luck in his future research endeavors.

I would like to thank Professor Edo Waks for graciously allowing me access to the Lumerical FDTD Solutions simulation software and for the use of his TCSPC measurement system. Additionally, the studies of fluorescence lifetime behavior would not have been possible without the assistance of Shilpi Gupta from his group. I would like to thank them both for their help in completing this work and hope they continue to enjoy success in their future research.

Finally, I would like to thank Professor McAfee from Rutgers University, my undergraduate instructor in electromagnetic wave phenomena. It was through her teachings and many unscheduled discussions that my fascination with optics began. Though it has been many years I still remember that time fondly and give her my best wishes for none of this would have been possible without her early mentorship.

Table of Contents

List of Figures

1 Introduction

Since their theoretical description by Ritchie [1] in 1957, the study of surface plasmon polaritons (SPPs) has advanced over the subsequent decades to become one of the most active research and development areas. A subset of more general surface wave phenomena known as surface polaritons, surface plasmons arise from interaction between electromagnetic waves and charge oscillation near the interface of metal and dielectric regions. Over the past decade these surface excitations have been linked to many novel concepts of significant scientific importance such as surface enhanced Raman scattering [2,3,4,5], negative index materials and superlenses [6,7], enhanced transmission through subwavelength apertures [8,9,10], and surface enhancement of nonlinear optical effects [11]. Not limited to such fundamental studies, surface plasmons have also found application across a range of more immediately practical areas from biodetection and telecommunications to semiconductor optical sources and spectrographic analysis. Due to strong confinement of the surface plasmon fields to the interface, the field amplitude is strongly enhanced over micrometer scale distances directly adjacent to the interface the effect of which is the observation of surface enhanced behaviors such as SERS [2,3,4,5] and enhanced second harmonic generation [11]. With the development of techniques that take advantage of this special property it is important that a greater understanding of how surface plasmons interact with optically active materials that have been placed in close proximity to the boundary region be developed. Unfortunately, effective excitation of surface plasmons requires special coupling apparatus or structures to overcome the inherent phase mismatch between waves

incident from vacuum and surface plasmons at the interface. One simple way to overcome this problem is through the use of periodic corrugations in the plane of the interface, which allow relaxation of the phase matching condition. The work presented herein will attempt to address some aspects of this complex problem. In order to examine the interaction between grating coupled surface plasmons and materials in close proximity to the interface quantum dots will be deposited onto the surface of samples that have had surface corrugations defined on them using electron beam lithography. This allows us to study how surface plasmons interact with the quantum dots on the surface and also evaluate what effect the surface structures have on the emission behavior of the particles. Due to the close proximity of the surface plasmon fields the quantum dots can experience strong enhancement of their fluorescence intensity and the conditions under which this effect can be observed are presented to explore the more practical aspects of the problem. Coupled to this is the presence of a metallic interface, required for surface plasmon propagation, which strongly affects the relaxation behavior of excited fluorophores at such short distances from the interface. This will be observed using both the fluorescence intensity as well the behavior of fluorescence lifetime measurements under varying conditions. Finally, in addition to the previous points, quantum dots are rising in popularity as a fluorescent source with the potential to augment or supplant fluorescent dyes in coming years and studies of their behavior in this context will be of interest for development in upcoming applications.

2 Surface Plasmon Polaritons

2.1 Basic Theory

Surface plasmon polariton modes can be derived directly by examining classical solutions to Maxwell's equations that are confined to the boundary between two different dielectric materials. To begin, consider the interface between two semi-infinite dielectric regions with dielectric constants $\varepsilon_1(\omega)$ and $\varepsilon_2(\omega)$ respectively.

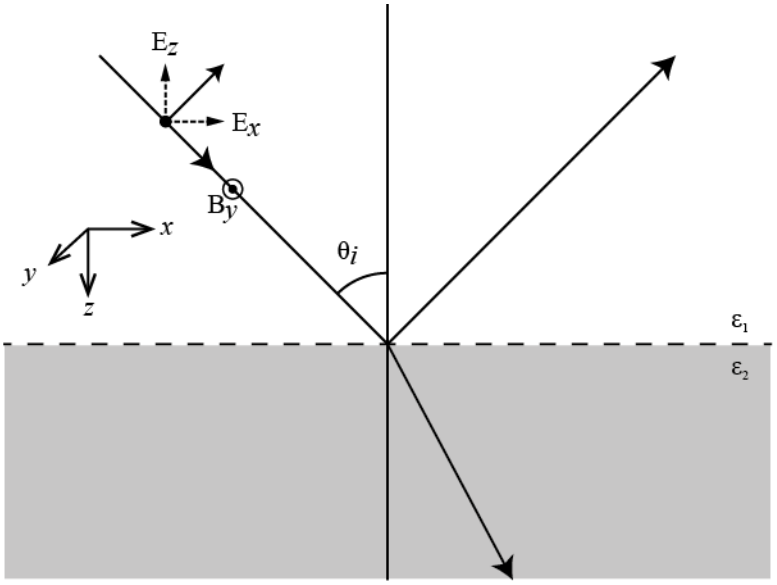

Figure 1 Graphical representation of the basic interface construction and orientation of electric and magnetic fields for P-polarized electromagnetic radiation

The boundary conditions at the interface of the two media are well known, and in the absence of free charges and currents are expressed in terms of the electric and magnetic field components as:

$$\begin{aligned} \overline{D}_{1n} &= \overline{D}_{2n} & \overline{B}_{1n} &= \overline{B}_{2n} \\ \overline{E}_{1t} &= \overline{E}_{2t} & \overline{H}_{1t} &= \overline{H}_{2t} \end{aligned} \qquad [2.1.1]$$

For a boundary along the x-direction the tangential fields are conserved and so the field component in the x-direction E_x is continuous across the interface. Along the normal direction however, continuity of the electric displacement $\bar{D}$ dictates that the electric field E_z be discontinuous across the boundary according to the relation $\varepsilon_1 \varepsilon_o E_{z1} = \varepsilon_2 \varepsilon_o E_{z2}$. When the electric displacement is expressed in an equivalent form as $\bar{D} = \varepsilon_o \bar{E} + \bar{P}$, where $\bar{P}$ is the macroscopic polarization density it becomes apparent that the electric field discontinuity gives rise to polarization changes at the interface. From this simple analysis it becomes clear that incident light which is S-polarized will not normally cause the creation of charge located at the interface. P-polarized light, on the other hand, will clearly produce surface charge at the boundary directly due to the inherent boundary conditions of the system. Thus, to a first approximation the excitation of surface plasmons would be anticipated primarily for light which is P-polarized in nature. Now consider the situation illustrated in Figure 1 for P-polarized light incident onto the interface between two media with different dielectric constants ε_1 and ε_2. If the positive z half space is taken to be the region within medium 2 then the electric and magnetic fields for a wave propagating solely in the x-direction will take the form

$$\begin{aligned} E_1 &= [E_{x1}, 0, E_{z1}] e^{i(k_x x - \omega t)} e^{ik_{z1} z} \\ H_1 &= [0, H_{y1}, 0] e^{i(k_x x - \omega t)} e^{ik_{z1} z} \\ E_2 &= [E_{x2}, 0, E_{z2}] e^{i(k_x x - \omega t)} e^{ik_{z2} z} \\ H_2 &= [0, H_{y2}, 0] e^{i(k_x x - \omega t)} e^{ik_{z2} z} \end{aligned} \qquad [2.1.2]$$

The expressions relating the different field components to one another are obtained by applying Maxwell's equations to [2.1.2]. Applying Gauss's law gives the relationships between the electric field components

$$\nabla \cdot \bar{E} = 0 \Rightarrow \frac{\partial E_x}{\partial x} + \frac{\partial E_y}{\partial y} + \frac{\partial E_z}{\partial z} = 0 \qquad [2.1.3]$$

$$\boxed{\begin{aligned} E_{z1} &= -E_{x1}\frac{k_x}{k_{z1}} \\ E_{z2} &= -E_{x2}\frac{k_x}{k_{z2}} \end{aligned}} \qquad [2.1.4]$$

Then, applying Faraday's law results in the relations linking the electric and magnetic fields

$$\nabla \times \bar{E} = -\frac{\partial B}{\partial t} \Rightarrow \left(\frac{\partial E_x}{\partial z} - \frac{\partial E_z}{\partial x}\right)\hat{j} = -\mu_o \frac{\partial H_y}{\partial t}\hat{j} \qquad [2.1.5]$$

$$\boxed{\begin{aligned} H_{y1} &= \frac{\omega E_{x1}\varepsilon_1\varepsilon_o}{c^2 k_{z1}} \\ H_{y2} &= \frac{\omega E_{x2}\varepsilon_2\varepsilon_o}{c^2 k_{z2}} \end{aligned}} \qquad [2.1.6]$$

Finally, from equation [2.1.1] the boundary conditions at $z = 0$ dictate that the tangential fields of both the electric and magnetic fields are continuous across the boundary. This leads to a simple relationship between the relative permittivity and the normal components of the wavevectors in both media

$$E_{x1} = E_{x2} \qquad H_{y1} = H_{y2} \qquad [2.1.7]$$

$$\frac{\omega E_{x1}\varepsilon_1\varepsilon_o}{c^2 k_{z1}} = \frac{\omega E_{x2}\varepsilon_2\varepsilon_o}{c^2 k_{z2}} \Rightarrow \boxed{\frac{\varepsilon_1}{k_{z1}} = \frac{\varepsilon_2}{k_{z2}}} \qquad [2.1.8]$$

In order to obtain a bound solution to the equations it is necessary for the fields in both media to decay with increasing distance away from the boundary. The result of this restriction is a set of conditions on the z-components of the wavevector such that $ik_{z1} > 0$ and $ik_{z2} < 0$. This constrains the z-components k_z in both media to be simultaneously imaginary and of opposite sign and therefore, from equation [2.1.8] the dielectric constants of the media must also be of opposite sign. Decomposing the wavevectors in each medium and expressing k_z in terms of the other components gives the following expressions when $\mu_r = 1$ as is the case for many materials at optical wavelengths.

$$\varepsilon_i k_o^{\,2} = k_x^{\,2} + k_z^{\,2} \qquad k_z = \left(k_x^{\,2} - \varepsilon_i k_o^{\,2}\right)^{1/2} \tag{2.1.9}$$

$$\begin{aligned} k_{z1} &= -i\left(k_x^{\,2} - \varepsilon_1 k_o^{\,2}\right)^{1/2} \Rightarrow \quad \boxed{k_x^{\,2} > \varepsilon_1 k_o^{\,2}} \\ k_{z2} &= i\left(k_x^{\,2} - \varepsilon_2 k_o^{\,2}\right)^{1/2} \Rightarrow \quad \boxed{k_x^{\,2} > \varepsilon_2 k_o^{\,2}} \end{aligned} \tag{2.1.10}$$

As the analysis has already indicated that the dielectric constants of the two media are of opposite sign the positive sign can be assigned to medium 1 in the upper region and the negative sign to the lower region of medium 2 without loss of generality. The relations derived in [2.1.10] then tell us that the magnitude of the surface mode wavevector k_x is greater than $n_1 k_o$, the maximum photon wavevector available in the upper dielectric. To look at this another way, if we express the in-plane wavevector as $k_x = n_{eff} k_o > n_1 k_o$ then the surface mode experiences an effective index that is higher than either of the component indices in the system. At the same time the effective wavelength of the surface mode λ_{sp} is shorter than that of radiation propagating in both of the semi-infinite media. The difference can be very significant

depending on how large the deviation from the light line the dispersion relation is at the point of interest. The second condition will be satisfied automatically in region 2 with $\varepsilon_2 < 0$. This is a very important result because it specifies that it is not possible to excite a surface plasmon directly from a dielectric medium using light incident on the boundary from medium 1 into medium 2. The momentum mismatch is a fundamental consideration in the application of surface plasmons to any practical situation as it necessitates the use of additional phase matching apparatus to enable coupling between the incident radiation and the surface mode of interest. Substituting equation [2.1.10] into [2.1.8] yields the expression for the dispersion relation of surface plasmons propagating along the boundary between the two regions

$$k_x = k_o \left(\frac{\varepsilon_1 \varepsilon_2}{\varepsilon_1 + \varepsilon_2} \right)^{1/2} \qquad [2.1.11]$$

In order to obtain a propagating mode the in-plane wavevector k_x must be real, which from the expression above leads to the additional condition that $|\varepsilon_2| > \varepsilon_1$. This analysis provides the fundamental basis for the conditions under which surface plasmon polariton excitation can occur. It is important to note that the relations above are valid for an arbitrary combination of dielectric constants for both the upper and lower regions and are valid for both solely real valued as well as complex dielectric constants and so can be used to consider the dielectric constants of real materials, which are characterized with an imaginary component describing absorption. When considering complex valued dielectric constants the propagation length is defined as the distance over which the intensity decays by a factor of $1/e$.

The intensity varies as the square of the electric field and so it decays at a rate proportional to $e^{-2k_x^{"}x}$. The propagation length of the surface wave is then

$$L = \frac{1}{2k_x^{"}} \qquad [2.1.12]$$

2.2 Dispersion

As indicated earlier the dispersion relation given in [2.1.11] is subject to two important constraints. These are $|\varepsilon_2| > \varepsilon_1$ and $\varepsilon_2 < 0$ both of which must be satisfied in order for the interface to support surface plasmon propagation at a wavelength of interest. At optical wavelengths both of these conditions can be satisfied by using a metal such as gold, silver or aluminum as the medium characterized by ε_2. The Drude model of electrical conduction is a simple model, which is commonly used to illustrate the behavior of the surface plasmon dispersion relation. It models electron transport through the medium using a classical analog of light electrons bouncing off of heavier immobile positive ions. Using this model in the limit where the product of the radial frequency and electron relaxation time $\omega\tau \gg 1$ the dispersion relation for the metal dielectric function reduces to

$$\varepsilon_m = 1 - \left(\frac{\omega_p}{\omega}\right)^2 \qquad [2.2.1]$$

The plasma frequency ω_p is the frequency above which electrons are no longer able to respond quickly enough to the incident field causing the metal to behave like a dielectric for frequencies above this point. For an ideal layer of gold, the plasma frequency occurs at ω_p = 9eV however it is important to note that in practice this value varies widely depending on the quality and properties of the deposited film and

has been shown to vary to values as low as 6eV due to the presence of defects in the material[12]. Substituting [2.2.1] into [2.1.11] for ε_2 and taking the bounding medium to be air so that $\varepsilon_1 \to \varepsilon_d = 1$ allows us to plot the dispersion behavior for a surface plasmon propagating along the interface of such a metal under these simplified conditions. The dispersion relation then becomes

$$k_{sp} = k_o \left(\varepsilon_d \left(1 - \frac{\omega^2}{\omega_p{}^2} \right) \Big/ \left(\varepsilon_d - \left(1 - \omega_p{}^2 \Big/ \omega^2 \right) \right) \right)^{1/2} \qquad [2.2.2]$$

Examining this expression shows that the resulting dispersion curve will tends towards infinity as the frequency approaches point where the denominator goes to zero which will occur when $\omega = \omega_p \Big/ \sqrt{1+\varepsilon_d}$.

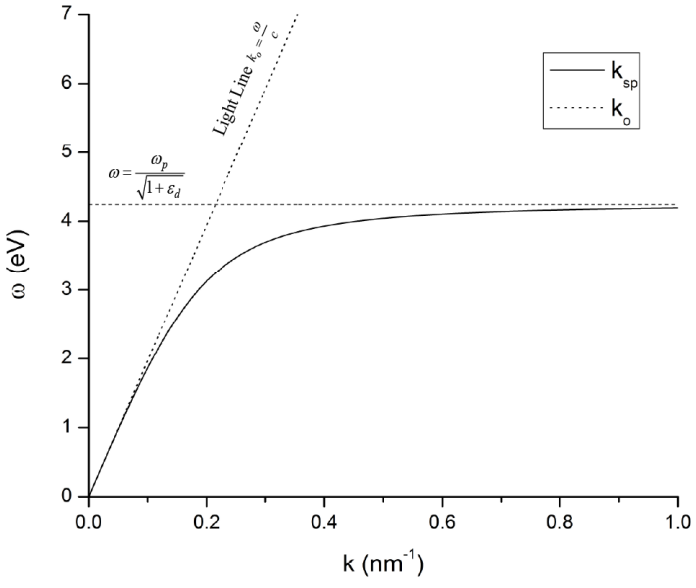

Figure 2 Dispersion relation for surface plasmon using Drude model for dielectric constant of gold, $\varepsilon_d = 3.5$ and $\omega_p = 9$eV

Examination of the resulting curve illustrates the general behavior of the surface plasmon resonance. At lower frequencies the dispersion curve closely follows the light line and gradually diverges at higher values frequencies always remaining to the right of the light line as dictated by the previous analysis. In spite of the presence of the singularity mentioned earlier, which causes the results to be unphysical near the asymptote, this model is useful for describing the behavior of surface plasmons in general terms, especially for examining coupling from an outside medium into surface waves.

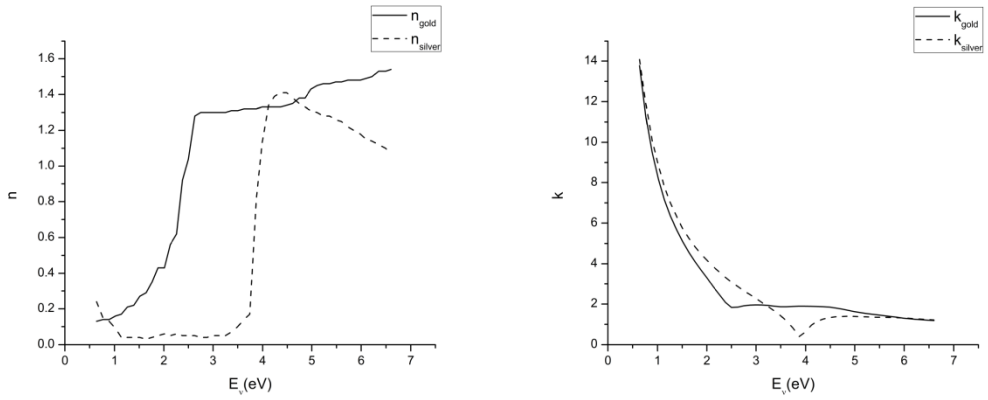

Figure 3 Complex index of refraction for gold and silver from Johnson and Christy [13]

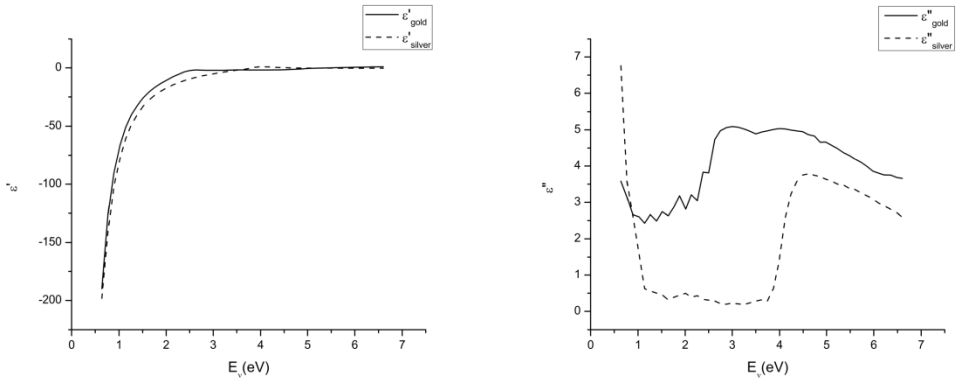

Figure 4 Complex dielectric constant calculated from Johnson and Christy data [13]

In practice, the dielectric properties of metals are complex-valued parameters, which vary according with wavelength in a fashion not completely described by the simple Drude model. Measurements of these properties for metals have been performed by many groups and accepted values have been used widely in the literature, most notably from the work of Johnson and Christy [13] and compiled data from the *Handbook of Optical Constants of Solids* by Palik [14]. The complex index of refraction is represented as $\tilde{n} = n + ik$ and is related to the dielectric constant by $\tilde{n}^2 = \tilde{\varepsilon}$ where $\tilde{\varepsilon} = \varepsilon' + i\varepsilon''$. The components of the dielectric constant can therefore be calculated from the complex index by the relations $\varepsilon' = n^2 - k^2$ and $\varepsilon'' = 2nk$. As mentioned in the previous section complex valued dielectric properties can be handled easily by direct substitution into the dispersion relation of equation [2.1.11].

$$k_x = k_o \left(\frac{\varepsilon_1(\varepsilon_2' + i\varepsilon_2'')}{\varepsilon_1 + \varepsilon_2' + i\varepsilon_2''} \right)^{1/2} \qquad [2.2.3]$$

Including the complex nature of the dielectric constant result in the wavevector for the surface excitation also taking on a complex form $k_x = k_x' + ik_x''$ where the propagation constant for the surface wave along the interface is k_x' and absorption as the wave travels is described by k_x''. The conditions for surface plasmon excitation under these conditions are slightly modified to account for the additional complex component so that $\varepsilon_2' < 0$ and $\left|\varepsilon_2'\right| > \varepsilon_1$ with an additional condition that for the two components of the in-plane wavevector $k_x' \gg k_x''$ in order for the surface wave to

propagate a significant distance across the interface. By defining a material for the upper layer the dispersion relation can be plotted just as before for the case of the Drude model. Calculations of the dispersion curves for gold and chromium are plotted in Figure 5. Including the imaginary components of the dielectric constant into the analysis results in the formation of an additional region in the dispersion relation, this can be seen as a reverse bending in the curve for gold. In this case, the dispersion relation can be divided into three regions. For energy below the region of anomalous dispersion surface plasmon modes can be considered just as previously described and the only additional consideration is attenuation of the surface wave as it propagates across the surface.

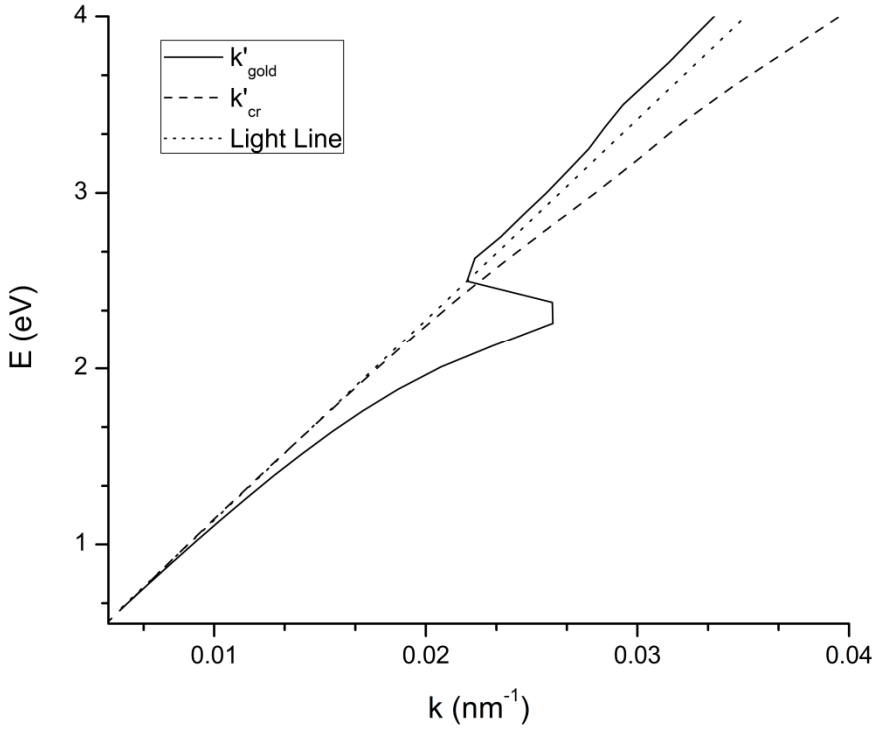

Figure 5 Surface plasmon dispersion curve calculated using measured values for gold [13] and chromium [15] as well as the light line for a dielectric overlayer with index n = 3

At energies above the anomalous dispersion feature the surface waves are able to couple to radiation in the surrounding media and behave as radiative plasmon polaritons. This same behavior appears when considering the Drude model although it has not been explicitly included in Figure 2. Within the region of anomalous dispersion are a set of modes that have mathematically real components and exhibit negative phase velocity. These modes are often labeled as quasi-bound modes and are of interest for study of backward wave propagation and associated effects such as negative refraction. Adding the imaginary components of the dielectric constant to the analysis causes the surface plasmon wavevector to take on a complex valued form. As a result absorption of the wave as it propagates is a significant consideration, as a large portion of the mode's energy propagates within the confines of the absorptive metal layer. In addition to the dispersion curve for the surface plasmon modes it is important to consider the relative magnitude of the real and imaginary components of the wavevector. An example of this can be seen when comparing the propagation of surface plasmons on the surface of gold and chromium layers. From Figure 5 it would appear that both chromium and gold are capable of supporting viable surface plasmon modes with chromium lacking the distinctive region of anomalous dispersion observed in gold. However, further examination of the complex components of the wavevector shows that chromium is actually not an effective medium for observation of surface plasmon related phenomena. The ratio between the real and imaginary components for these two materials is plotted in Figure 6 and illustrates that despite the apparent compatibility of chromium to support

surface plasmon propagation the imaginary component is significantly large such that propagation is not possible and any excited modes decay rapidly.

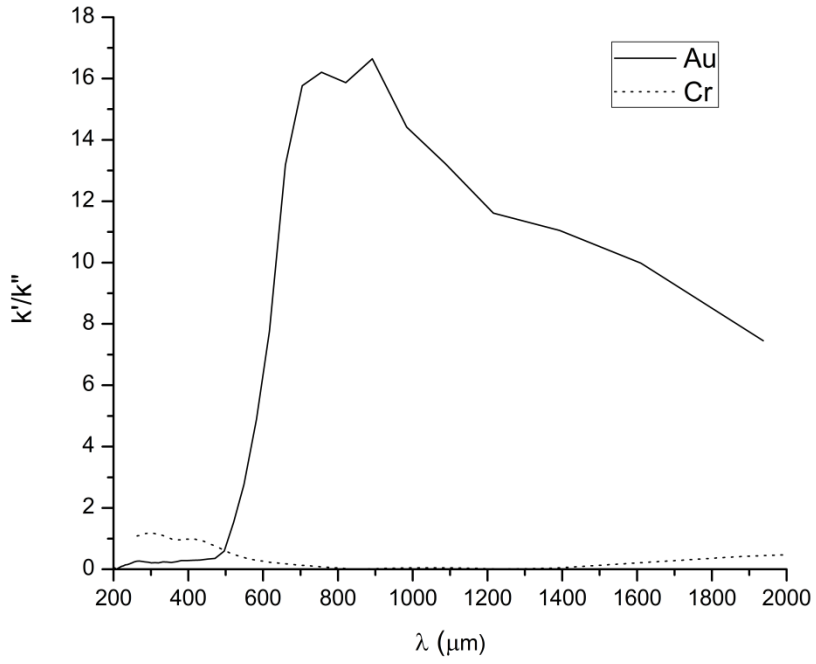

Figure 6 Ratio of the real and imaginary components of the surface plasmon wavevector calculated using measured values for gold [13] and chromium [15] and a surrounding dielectric of index n = 3.

2.3 Coupling to Surface Plasmon Polaritons

2.3.1 Prism Coupling

In order to take advantage of the special properties that surface plasmons possess, the first obstacle that must be overcome is satisfying the conditions for coupling of radiation into the surface mode. To solve this problem requires the use of additional structures or apparatus through which sufficient additional quasi-momentum is provided to the incident waves to offset the momentum mismatch. One of the oldest and most widely used methods for exciting surface plasmons on a surface is through

the use of a high index prism which has been coated on one face with a material that supports surface plasmon propagation at the outer interface.

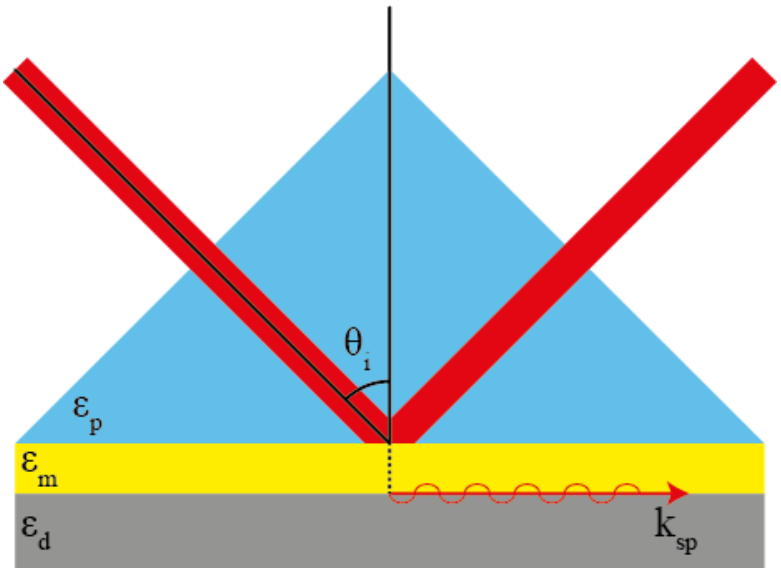

Figure 7 Simple schematic of prism coupling geometry for surface plasmon excitation using a prism with dielectric constant ε_p, metal film with ε_m, and dielectric overlayer of ε_d

The basic geometry for prism mediated surface plasmon coupling is illustrated above in Figure 7. It is well established that a wave incident onto the prism-dielectric interface at an angle greater than the critical angle experiences total reflection off of the interface. For these angles the magnitude of the incident wavevector within the prism is too large to be supported in the lower index medium outside. As a consequence the incident wave is totally reflected from the interface and the fields in the second region take on an exponentially decaying form in the direction normal to the interface. These two properties provide a means by which it is possible to realize excitation of surface plasmon waves by conversion from incident radiation. The analysis presented earlier demonstrates that according to the dispersion relation for

surface plasmon propagation the in-plane wavevector is always of greater magnitude than a wave propagating in either medium. For angles greater than the critical angle the wave momentum in the x-direction is $n_1 \hbar k \sin\theta_i$. Above the critical angle $\sin\theta_i > \sin\theta_c = {}^{n_2}\!/_{n_1}$, this corresponds to the momentum relation $n_1 \hbar k \sin\theta_i > n_2 \hbar k$ which results in an enhancement of the in-plane momentum above the limit for a wave propagating outside of the prism. This increase in momentum can be used to provide phase matching between the incident waves and surface modes provided that the material selection falls within the appropriate ranges. In addition to the momentum shift, the evanescent field structure at the boundary provides a partial match to the evanescent nature of the surface fields. This allows the field from the first interface to couple evanescently to a surface plasmon wave at the interface between the metal and the outer dielectric. Coupling using this method can be accomplished in several configurations with the prevalent methods being the Otto geometry, where the prism is separated from the metal by a small gap, and Kretschmann-Raether, where the film is deposited directly onto the prism face. In the Kretschmann geometry the film itself forms an evanescent tunneling barrier between the two interfaces of the metal. Since the field couples evanescently between the two surfaces of the metal film the thickness of the metal layer plays a critical role and must be thin enough for fields on one interface to reach across through the film. The basic reasoning behind this coupling behavior can be seen graphically by considering the dispersion curve for plasmons propagating on the upper interface along with the light lines for light propagating in the dielectric media bounding the metal film.

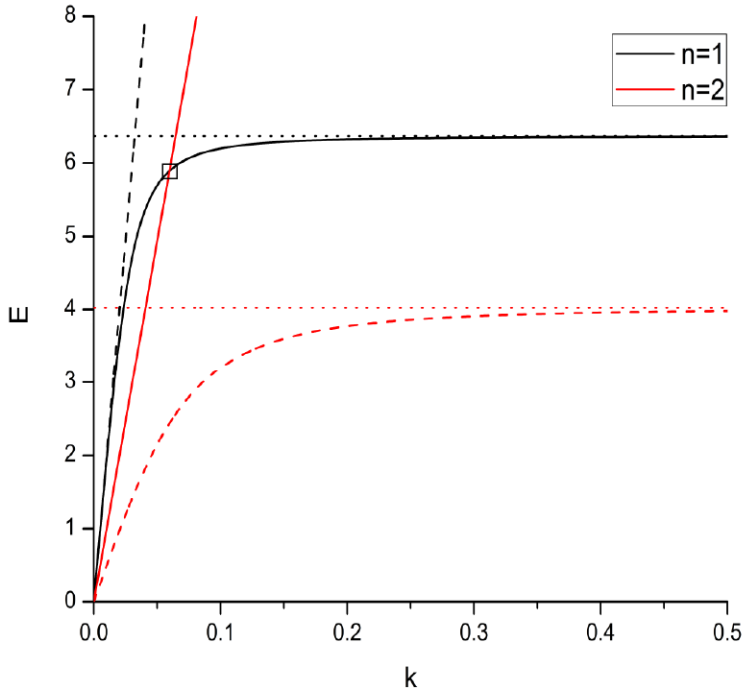

Figure 8 Dispersion relation for surface plasmons at the interface between gold and dielectric layers of index n = 1 (black) and n = 2 (red) using dielectric constants from the Drude model. Coupling can occur in a prism geometry when the light line in the higher index material matches the surface plasmon wavevector at the metal interface to the lower index. This point is denoted by the box.

This graphical relationship can be seen in Figure 8 using the Drude model for a prism with an index of 2 and air as the dielectric overlayer. Within the high index prism the light line shifts towards higher momentum values and moves to the right of the plasmon dispersion curve at the metal-air interface. At the point within the box this light line and the plasmon dispersion curve intersect indicating the point where phase matching between light propagating through the prism and surface waves on the upper interface is possible. Modulating the angle of incidence θ_i modifies the slope of the line and shifts the coupling point along the dispersion curve. The limits of this

coupling range are defined by the lines for $k = {}^{c}/_{\sin\theta_i}$ and $k = {}^{c}/_{n_p}$ representing the values at the critical angle and normal incidence respectively. This results in different angular coupling behavior for different wavelengths. For a single wavelength the reflection measured for light exiting the prism at the face opposite the input plane is used to examine the surface plasmon coupling behavior of the prism-film system. Unlike the analyses presented earlier, which assumed an interface between two semi-infinite media the configuration here requires consideration of a finite metal layer bounded by the prism below and a dielectric above. For simplicity the software WINSPALL [16] is used in Figure 9 to plot the resulting reflectivity curves.

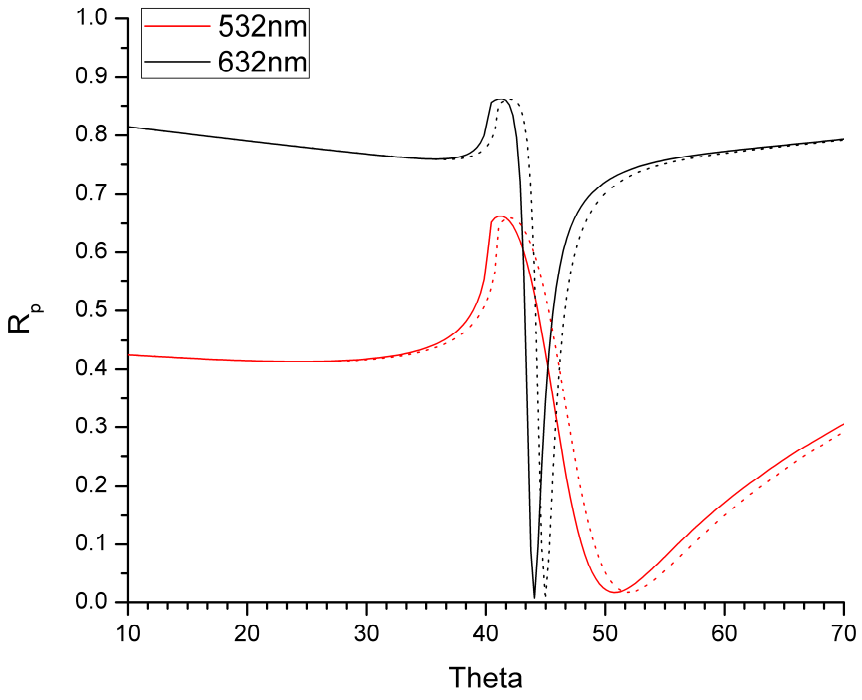

Figure 9 Reflectivity curves for 50nm thick gold film deposited onto a prism with a refractive index of 1.5. Curves are plotted for 532nm and 632nm P-polarized light in red and black respectively. The dielectric constant of the bounding dielectric is taken as n=1 for air (solid) and n=1.01 (dotted).

The reflectivity of this system can be calculated using Fresnel's equations for a three-layer system (see Section 2.4). For a film of thickness d the reflectivity R for P-polarized light can be written as:

$$R = \left|\rho_{012}\right|^2 = \left|\frac{E_{o-}}{E_{0+}}\right|^2 = \left|\frac{\rho_{01} + \rho_{12} e^{-2j\delta_1}}{1 + \rho_{01}\rho_{12} e^{-2j\delta_1}}\right|^2 \qquad [2.3.1]$$

$$\rho_{ij} = \frac{\frac{n_i}{\cos\theta_i} - \frac{n_j}{\cos\theta_j}}{\frac{n_i}{\cos\theta_i} + \frac{n_j}{\cos\theta_j}} \qquad [2.3.2]$$

Here the layer indices are organized with the prism as layer 0, the metal layer 1, and the overlying dielectric layer 2. The angle at which coupling to the surface plasmon resonance occurs can be clearly distinguished from the associated reflectivity curves as sharp dip in the reflectivity curves. Comparing different wavelengths it is clear that the quality and position of the resonance is strongly dependent on the wavelength used to excite the surface waves. Under appropriate conditions the resonance can be quite sharp, as in the curve shown above for 632nm. By changing the dielectric constant of the bounding dielectric layer we can also see that the position of the resonance dip is very sensitive to the value of the surrounding index with a clearly defined shift resulting from an index change of 0.01. This has made the prism geometry popular in many applications, especially for sensing where high sensitivity is required [17,18]. However, these beneficial properties are not without cost and utilization of prism coupled surface plasmon techniques often requires construction of relatively complicated apparatus, especially when the ability to scan with angle is necessary.

2.3.2 Coupling by Gratings

For applications where space is limited or it is desirable to integrate plasmonic effects into existing systems the prism type of apparatus may be too cumbersome or complex for implementation. An alternative method for surface plasmon coupling which provides the capability for plasmon excitation without the requirement for such complex apparatus is to use a periodic surface corrugation to provide phase matching to the surface mode. In this configuration, instead of using the intrinsic properties of a second medium to overcome the momentum mismatch the properties of the interface are modified by the introduction of surface structures that interact with incident radiation. If the structures on the surface are distributed randomly in such a way that each site may be considered as a point defect surface plasmon excitation can occur without any additional arrangements [19]. In this case, the conversion is facilitated by the presence of diffracted components with all wavevectors in the near field due to diffraction at the defect location. Unfortunately the random nature of the distribution means that the coupling condition is ill defined so that coupling occurs in a random uncontrollable fashion resulting in low efficiency. This problem can be alleviated by imposing control over the characteristics of the surface geometry and introducing periodic corrugations at the interface rather than a random distribution. A grating defined this way can then be used to provide the additional in-plane momentum through constructive reinforcement along the direction of its periodicity. Due to the translational symmetry of the periodic structure, phase matching to surface plasmons can occur when the sum of the incident in-plane wavevector, $k_{o,}$ combined with an integer multiple of the grating vector, $k_{G,}$ matches the momentum of surface

plasmon k_{sp}. For a grating with period Γ this condition is expressed mathematically as:

$$\bar{k}_o \sin\theta_i + n\bar{k}_G = \bar{k}_{sp}$$
$$\left|\bar{k}_G\right| = \frac{2\pi}{\Gamma} \qquad [2.3.3]$$

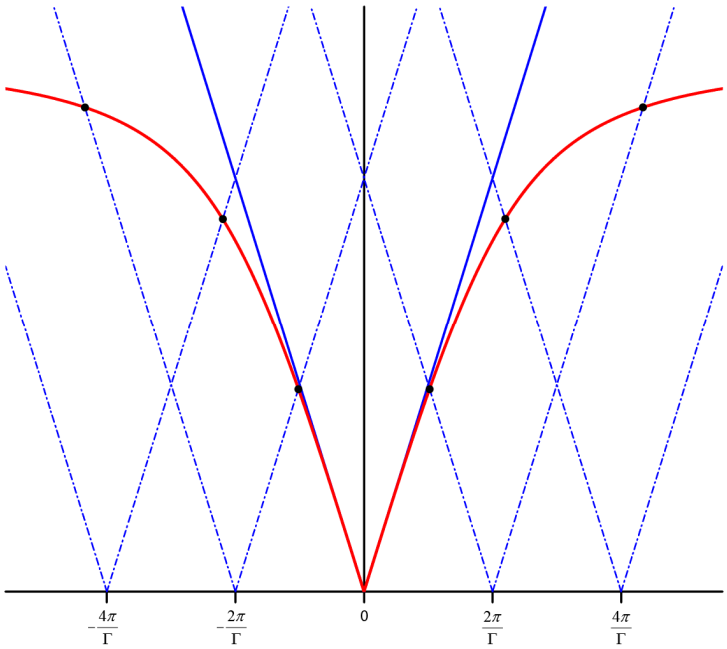

Figure 10 Momentum space representation of surface plasmon coupling via grating. The light line for incident light (—) is matched to surface plasmon dispersion curve (—) by repetition due to the translational symmetry of the surface structure (□•). Coupling occurs at the points where the repeated light line intersects with the dispersion plasmon dispersion curve (•).

The principles of this coupling condition can be seen graphically in Figure 10. The effect of the grating's translational symmetry is to repeat the dispersion relation of the light line by spacing equal to the magnitude of the grating vector k_G. The result of this replication is that the light line for incident radiation, which is normally unable to intersect the dispersion curve for surface plasmons, is offset to momentum values outside its normal range. As a result of this shift additional intersection points arise

between the plasmon dispersion curve and the offset light line. Unlike the prism coupling geometry where the angle required for conversion is fixed by the dielectric properties of the materials bounding the interface, excitation of surface plasmons via a grating is dependent on the periodicity and relative orientation of the surface structure as well as the angle of incidence. For a prism coated with a planar metal film, coupling occurs coplanar to incident excitation with no additional preference imposed on the plasmon propagation direction in the plane of the film besides the plane of incidence. In the case of grating coupling, phase matching is represented in momentum k-space as the vector sum of the incident wave and grating vectors. As a result, propagation of the surface plasmon wave excited by this interaction is constrained to the direction dictated by the orientation of the grating vector to the plane of incidence. For a particular wavelength, the angle that the surface plasmon wave propagates at with respect to the grating vector can be determined by considering the vector diagram for the coupling process. Light incident onto the grating with in-plane component k_x can couple to surface plasmons by satisfying the condition from [2.3.3]. Graphically the possible values for the vector combination of contributions from the grating and incident light are represented by the black circle. The possible values for the surface plasmon wavevector occur along the path outlined by the red circle. Coupling occurs at the points of intersection between the two circles shown in Figure 11 with the allowed directions for surface plasmon propagation illustrated by the red vectors. The vector that satisfies the coupling condition is defined by the wavelength, amplitude of the in-plane component of the incident light, and the orientation of the grating.

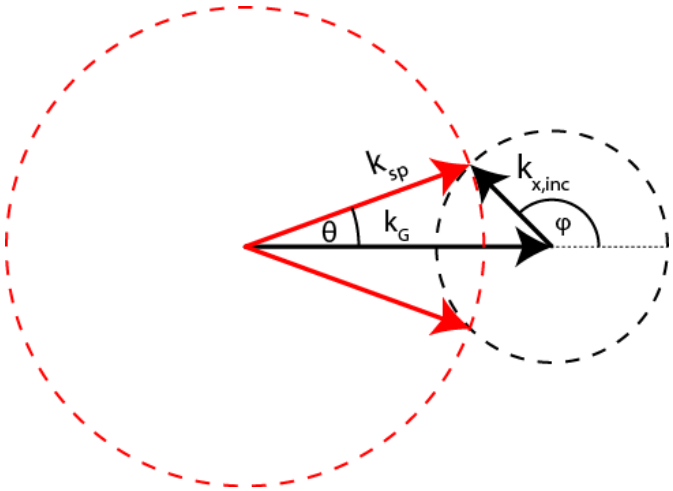

Figure 11 Vector diagram for surface plasmon excitation by phase matching via grating. Light is incident onto the grating with in-plane component k_x. Coupling is allowed at the intersection points for light incident at an angle φ relative to the grating line and excites plasmons travelling at angle θ.

Results to this effect have been presented in the literature to produce structures which focus excited surface plasmons [20] as well as the use of gratings to provide phase matching for surface plasmon enhanced second harmonic generation [11]. It is important to note that the coupling to surface plasmons in this way is a reciprocal problem. Just as it is possible for incident photons to couple into surface waves at the grating, surface waves propagating across the grating can undergo the reverse transition and transfer their energy into radiating photons. This interaction occurs under the same conditions described previously for the in-coupling process except that the photons generated travel at angles defined by Equation [2.3.3]. Unlike the prism coupling method, which requires the excitation to be incident on the interface from a higher index medium, grating coupling can be performed from either the upper or lower dielectric medium provided that a suitable match can be found by combination with the grating vector. This can provide a significant reduction in

system complexity by removing the need for additional apparatus aside from requirements for fabrication of the surface structure. The cost of this reduction comes in the form of additional complexity in sample preparation to produce a controlled surface rather than the normal planar interface. The additional coupling restrictions described above also introduce the need for careful design and characterization to properly control the properties of the structure and facilitate practical application.

2.4 Field Enhancement

In many applications the practical advantages of using surface plasmon waves derive from the special field structure they possess due to their character as bound wave solutions. The electric field of the surface plasmon perpendicular to the interface decays exponentially into both media in an asymmetric fashion defined by the dielectric properties of the media on either side of the interface. A direct consequence of this field structure is that the majority of the energy propagating in the surface wave is bound to the region closest to the interface on either side of the boundary. For the case of two semi-infinite media the z-components of the wave vector can be expressed in terms of the dielectric constants of the two materials. This is accomplished by simply considering the vector relation between the incident wave and the x and z components of the surface wave from [2.1.10]. The contribution from the y-component of the wavevector is removed by orienting the coordinate system appropriately without loss of generality due to isotropic symmetry in the material geometry. For the interface between two semi-infinite regions with the metal occupying the half-space $z < 0$ the relations take the form:

$$\varepsilon_i k_o^2 = k_x^2 + k_{zi}^2 \qquad [2.4.1]$$

$$k_{zi}^2 = \varepsilon_i k_o^2 - k_o \sqrt{\frac{\varepsilon_m \varepsilon_d}{\varepsilon_m + \varepsilon_d}} \Rightarrow \boxed{\begin{cases} \dfrac{k_o \varepsilon_d}{\sqrt{\varepsilon_m + \varepsilon_d}} & z > 0 \\ -\dfrac{k_o \varepsilon_m}{\sqrt{\varepsilon_m + \varepsilon_d}} & z < 0 \end{cases}} \qquad [2.4.2]$$

$$E = E_o e^{i(wt - k_x x - k_z z)} = E_o e^{-k_z'' z} e^{i(wt - k_x x - i k_z' z)} \qquad [2.4.3]$$

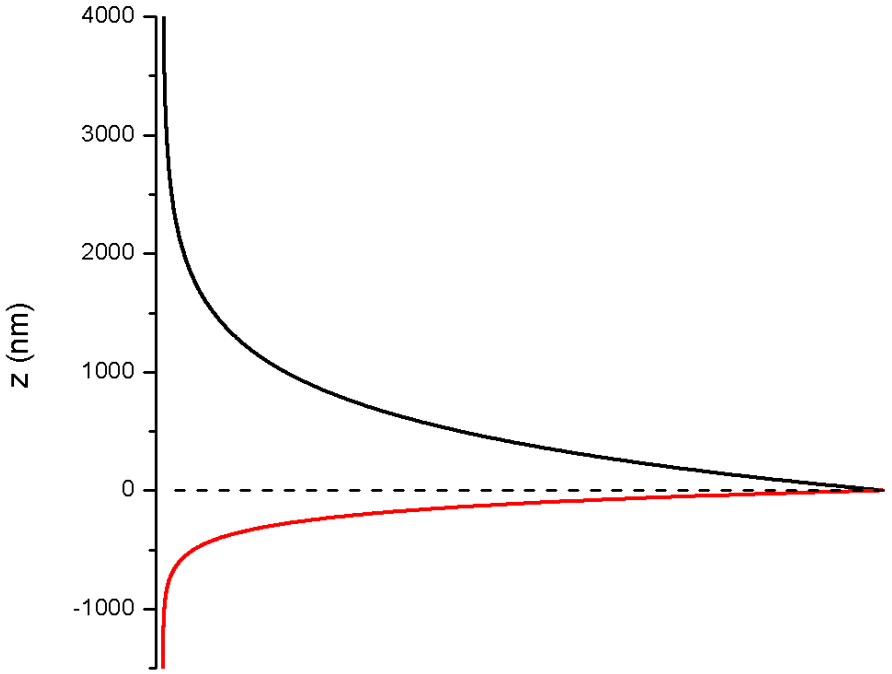

Figure 12 Decay characteristics of surface plasmon field away from metal-dielectric interface for air-gold at λ = 640nm. It is clear that the field resides primarily in the upper dielectric medium (black) and decays rapidly within the metal (red).

The transverse field decay characteristics for an air-gold interface are plotted in Figure 12 for light with a wavelength of 640nm. It is clear from the figure that most of the energy propagates on the upper side of the interface within the air. As expected the component of the field within the metal decays rapidly away from the interface and penetrates less than 500nm into the lower region. The choice of upper dielectric affects the relative penetration into the two media and higher index

materials push the field towards the interface and further into the metal layer. This can play an important role in the propagation length as the majority of the losses occur from attenuation in the metal. Regardless of the material selection, the field is clearly at maximum value directly on the interface which makes it important to examine the value of the electric field at this point. In order to provide a comparison between the amplitude of an incident wave and the peak surface plasmon field let us return to the three layer system described previously for the prism coupling geometry. If the reflectivity of the incident wave reaches its lowest value the intensity of the electromagnetic field at the surface reaches a maximum. A comparison of the incident and peak surface fields can be obtained by examining the ratio of the field intensity at the dielectric side of the metal-dielectric interface to the incident field intensity. This can be accomplished by considering the transmission and reflection for a thin dielectric film bounded between two semi-infinite dielectric media.

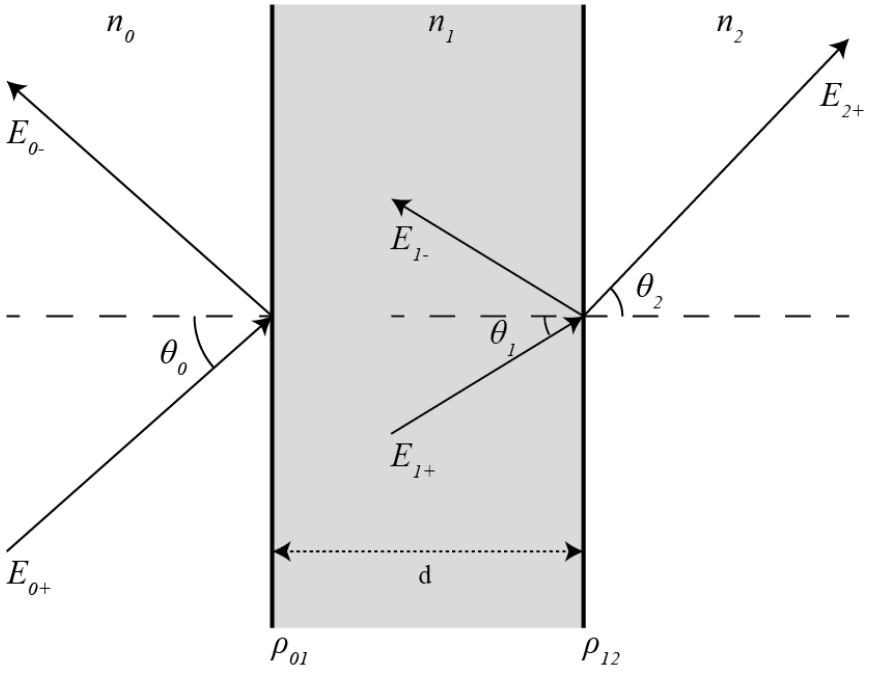

Figure 13 Oblique incidence onto a thin dielectric layer

The solution for a wave propagating at oblique incidence through a thin dielectric layer can be obtained through the use of layer recursions to transform the fields exiting the layer in medium 2 back towards the input in medium 0. This solution accounts for both the forward and backward propagating components within each layer and the sum of all reflection and transmission from each interface. Here the analysis will be limited to the case of propagation of P-polarized light as this is the only polarization that is capable of exciting surface plasmons directly on a plane interface. Assuming that no fields are incident onto the structure from the right, the only fields in medium 2 are propagating away from the interface in the positive direction. The reflection and refraction angles at each interface are related to one another by Snell's law applied to each interface.

$$n_i \sin\theta_i = n_{i+1} \sin\theta_{i+1} \qquad [2.4.4]$$

It is convenient here to define the thickness of the layer in terms of the phase thickness that wave experiences as it propagates.

$$\delta_i = k_{zi} d_i \qquad [2.4.5]$$

The field transmission and reflection coefficients at each interface can be derived from the boundary conditions for P-polarized light and can be expressed in terms of the angles and refractive indices.

$$\rho_{ij} = \frac{\frac{n_i}{\cos\theta_i} - \frac{n_j}{\cos\theta_j}}{\frac{n_i}{\cos\theta_i} + \frac{n_j}{\cos\theta_j}} = \frac{\frac{k_{zi}}{\varepsilon_i} - \frac{k_{zj}}{\varepsilon_j}}{\frac{k_{zi}}{\varepsilon_i} + \frac{k_{zj}}{\varepsilon_j}} \qquad \tau_{ij} = 1 + \rho_{ij} \qquad [2.4.6]$$

The layer recursion is implemented by taking the fields to the left of interface i+1 and applying a propagation matrix to transfer them to the right of interface i. A matching

matrix is then applied to pass the fields back across the interface to the left side of interface *i* where the process can be repeated for successive layers.

$$\begin{bmatrix} E_{i+} \\ E_{i-} \end{bmatrix} = \frac{1}{\tau_{ij}} \begin{bmatrix} 1 & \rho_{ij} \\ \rho_{ij} & 1 \end{bmatrix} \begin{bmatrix} e^{j\delta_i} & 0 \\ 0 & e^{-j\delta_i} \end{bmatrix} \begin{bmatrix} E_{j+} \\ E_{j-} \end{bmatrix} \qquad [2.4.7]$$

For the case of a single layer the recursion process requires only a few steps beginning with the transformation of the forward propagating fields in the rightmost layer back across the last interface.

$$\begin{bmatrix} E_{i+} \\ E_{i-} \end{bmatrix} = \frac{1}{\tau_{12}} \begin{bmatrix} 1 & \rho_{12} \\ \rho_{12} & 1 \end{bmatrix} \begin{bmatrix} E_{2+} \\ 0 \end{bmatrix} = \frac{1}{\tau_{12}} \begin{bmatrix} E_{2+} \\ \rho_{12} E_{2+} \end{bmatrix} \qquad [2.4.8]$$

The fields can then be propagated across layer 1 and back across the first interface to obtain the expressions for the overall transmitted and reflected fields.

$$\begin{bmatrix} E_{1+} \\ E_{1-} \end{bmatrix} = \frac{1}{\tau_{01}\tau_{12}} \begin{bmatrix} 1 & \rho_{01} \\ \rho_{01} & 1 \end{bmatrix} \begin{bmatrix} e^{j\delta_1} & 0 \\ 0 & e^{-j\delta_1} \end{bmatrix} \begin{bmatrix} E_{2+} \\ \rho_{12} E_{2+} \end{bmatrix} \qquad [2.4.9]$$

$$\begin{bmatrix} E_{1+} \\ E_{1-} \end{bmatrix} = \frac{1}{\tau_{01}\tau_{12}} \begin{bmatrix} E_{2+} e^{j\delta_1} + \rho_{01}\rho_{12} E_{2+} e^{-j\delta_1} \\ \rho_{01} E_{2+} e^{j\delta_1} + \rho_{12} E_{2+} e^{-j\delta_1} \end{bmatrix} \qquad [2.4.10]$$

$$\boxed{\begin{aligned} R &= \left|\rho_{012}\right|^2 = \left|\frac{E_{o-}}{E_{0+}}\right|^2 = \left|\frac{\rho_{01} + \rho_{12} e^{-2j\delta_1}}{1 + \rho_{01}\rho_{12} e^{-2j\delta_1}}\right|^2 \\ T &= \left|\tau_{012}\right|^2 = \left|\frac{E_{2+}}{E_{0+}}\right|^2 = \left|\frac{\tau_{01}\tau_{12} e^{-j\delta_1}}{1 + \rho_{01}\rho_{12} e^{-2j\delta_1}}\right|^2 \end{aligned}} \qquad [2.4.11]$$

The intensity enhancement at the right of interface 2 can be observed by calculating the value of the transmission coefficient T. Values of T using gold as the medium are shown in Figure 14 for light incident from inside a prism for light with a 632nm wavelength. The field is strongly enhanced for angles close to the minimum

reflection point of the resonance dip and exhibits a peak value of 10.49 at the angle coinciding with minimum reflection. This value can be increased or decreased depending on the properties of the metal layer at the wavelength of interest. The capability to produce strongly enhanced fields near the metal surface has driven interest in surface plasmons for many applications which rely on optical fields for excitation. Interest in studying the effect of the local field on the behavior of optical materials and devices has resulted in the publication of scientific results in many areas such as surface enhanced Raman scattering [2,3,4,5], enhanced fluorescence [21,22,23], nonlinear optics [11], and more recently plasmon enhanced solar cells [24,25]. It is the interplay between this enhanced surface field and effects which occur due to the presence of the metallic interface that provides part of the motivation for the study which will be presented here.

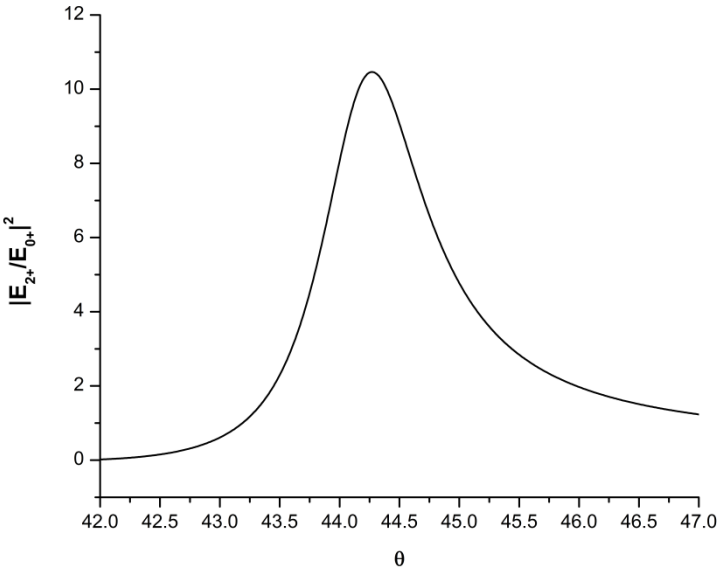

Figure 14 Transverse magnetic field intensity enhancement at metal-air interface for 50nm gold layer on a prism of index 1.5 with air above. The index of gold is taken to be .18508-3.42329i at a wavelength of 632nm.

3 Quantum Dots

Over the past two decades great strides have been made in the fabrication and characterization of nano-structured materials and nano-scale features on surfaces. Progressive development and proliferation of commercially available high resolution fabrication and imaging technologies such as electron-beam lithography, ion-beam lithography, and various scanning probe technologies, along with improvements in SEM and TEM capabilities have expanded our ability to manipulate devices and materials on a near atomic scale. An important consequence of this progress has been the realization of quantum confinement structures where modulation of structural dimensions has a direct impact on the electronic states of materials. While two dimensional quantum wells have been used in devices for some time, one dimensional quantum lines and zero dimensional quantum dots are currently an active source of ongoing research. In particular, quantum dots are of great interest for use in optics applications as they exhibit many desirable traits compared to bulk materials. These typically consist of semiconductor nanocrystals, which can be synthesized using a variety of techniques [26,27,28,29]. Quantum dots fabricated through colloidal techniques are easily obtained commercially and have been studied extensively by many groups. In a bulk semiconductor electron-hole pairs generated by injection of energy into the material will dissociate from one another to a degree where their separation exceeds the exciton Bohr radius which is determined by the strength of the electron-hole coulomb interaction. This results in delocalization of the carriers within the bulk of the material and decoupling of the individual charges such that the electron and hole which have been cogenerated are considered to be

independent of one another. Unlike the bulk case, in a quantum confinement structure the dimension of the semiconductor material are reduced until the physical dimensions of the structure are confined to an area smaller than the Bohr radius of generated carrier pairs. As a result, the electron and hole are no longer able to escape from one another after generation and instead form an exciton due to their opposite charges, which is similar to a hydrogen atom where the mass of the positive charge is given by the hole effective mass rather than a proton. Instead of the conduction and valence bands of the bulk semiconductor material the coupled interaction of the carriers results in the formation of a series of excitonic energy states, which derive their characteristics from the overlap of the electron-hole wave functions within the nanoparticle. Due to the strong spatial confinement of the carriers in all three dimensions these energy states are directly correlated to the physical dimensions of the material system and this is known as the quantum size effect. The result is that the energy gap as well as the absorption and emission properties of these materials can be directly modified by exercising control over the physical dimensions of the particle rather than being directly correlated only to the properties of the constituent materials. As in an atomic system, the energy states for excitonic interactions within the particle are characterized by a series of discrete energy levels which replace the continuum of states which would normally be observed. This property along with their size dependent absorption and emission behavior has led to the analogy of quantum dots as materials which simulate designer atoms. This ability to control their optical properties as well as their physical characteristics has made quantum dots popular as a potential substitute for fluorescent dyes in many applications.

3.1 Quantum Dot Fundamentals

The basic structure of a colloidal quantum dot consists of a small nanocrystal of semiconductor material containing roughly 100-10,000 atoms which is typically encapsulated using surfactant molecules for passivation and stabilization of the surface chemistry. Synthesis of the particles using chemical techniques has become a relatively mature technology with solutions containing suspended crystallites widely available from commercial sources. Using these methods various research groups have been able to demonstrate fabrication of nanoparticles in a variety of shapes such as spherical [27,30], elongated rods [31], and other more complex shapes such as tetrapods [32]. Due to the ultra-small dimensions of the particles, carriers generated within the core of the quantum dot experience strong interaction with the surface of the particle as a result of the extension of the carrier wave functions beyond the physical boundaries of the crystalline core material. As a consequence, the performance quality and internal carrier dynamics in these materials is especially sensitive to perturbation at the interface between the crystallite and the surrounding material. Surface regions have difficult surface chemistry, which is often complicated by the presence of dangling bonds and uncontrolled attachment of various undesirable substances, which can introduce local traps and perturbations that serve to interfere with the performance of the bulk material. The presence of the surfactant molecules can also introduce additional complications if carriers within the core are able to couple into the various molecular states present in the chains. In particular, the presence of local traps presents an avenue for non-radiative carrier loss that can result in reduction of the particle's quantum efficiency as well as

modifications in the carrier decay dynamics measured during experiments. In order to avoid these complications it is desirable to confine the carriers within the core material of the quantum dot as much as possible in order to isolate them from the effects of surface imperfections. This has led to the development of core-shell quantum dots which alleviate many of the surface related problems [33]. These consist of the quantum dot core, which is subsequently encapsulated inside a shell of material with a wider bandgap, onto which the surfactant layer is then added for stabilization. This shell facilitates the formation of a multi-step potential well, which increases confinement of the carriers within the core material and isolates them from the outer surface encouraging efficient light emission and significantly reducing nonradiative contributions to the lifetime originating at the surface. Surface passivation is typically achieved by attachment of various capping layers to the outer surface can be used to alter the solubility properties of the particles in different solvents notably to provide solubility in water rather than organic solvents such as toluene or chlorobenzene.

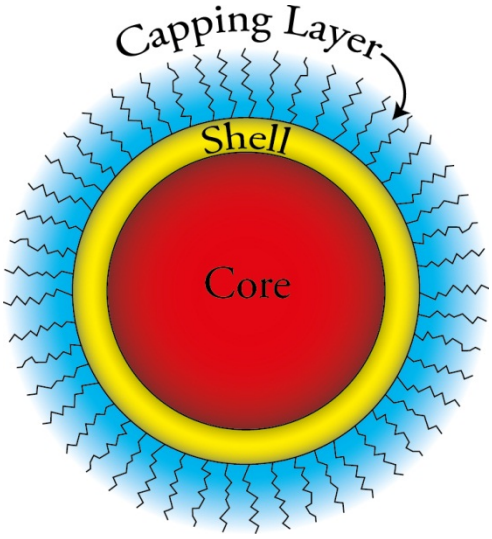

Figure 15 Simple depiction of a typical colloidal quantum dot.

3.2 Electronic Structure and Carrier Dynamics

The electronic structure within a quantum dot differs significantly from the conduction and valence band structure of its bulk constituents due to size dependent quantum effects, which modify the behavior of the electron and hole wave functions. The behavior of carriers confined within these semiconductor nanocrystals has been studied by several groups in recent years, leading to significant developments in understanding the underlying carrier physics, and the study of various multiexciton dynamics continues to be an active area of current research. If band-mixing effects can be neglected each bulk energy band gives rise to a series of quantized energy states. Early work in this area by Efros [34] using spherical Bessel functions to characterize spherically shaped crystallites demonstrated that for a simple model these states can be classified using two quantum numbers. The first quantum number, L, describes the angular momentum of the carrier envelope wave function and the other, n, denotes the energy of the state within a given symmetry. This nomenclature can be considered as analogous to the electronic states within a hydrogen atom and a similar naming convention may be adopted for state numbering with angular momentum indicated by letter (L=0 is S, L=1 is P, etc.). This basic model provides a reasonable approximation to the nanocrystal conduction band however given the complex multi-subband characteristics of the valence band in most semiconductors description of the valence-band structure in quantum dots requires consideration of confinement induced inter-subband mixing [35,36].

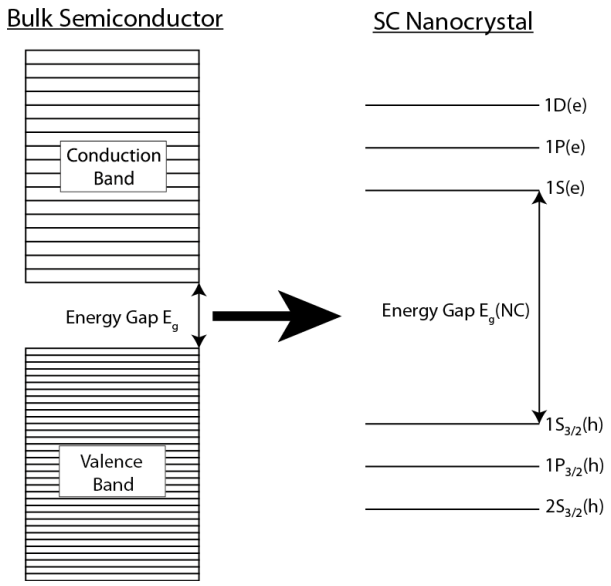

Figure 16 In a bulk semiconductor the electronic structure results in the formation of large bands of electron and hole states which from the conduction and valence bands. These bands are separated by the energy gap E_g which is derived from the lattice properties of the crystal structure. Reduction of the material to a nanocrystal geometry modifies this structure into a series of discrete energy levels. The new electron and hole states are separated by a larger gap E_g(NC) which is related to the spatial dimensions of the crystal through quantum size effects. Energy levels for CdSe are shown.

In this case, the angular momentum quantum number from the simplified model is replaced by the quantum number describing the total angular momentum, $\vec{F}$, which is the sum of the Bloch function orbital momentum from the crystal lattice, $\vec{J}$, and the orbital momentum of the hole envelope function, $\vec{L}$. With this modification the valence band states are now denoted by their energy and total angular momentum n_{LF}. The size dependent hole energies in CdSe have been calculated by Ekimov et al. [36] with the inclusion of mixing between the heavy, light, and spin-orbit split-off valence subbands. According to these calculations the lowest hole states are characterized by total angular momentum of $\vec{F} = 3/2$ and subsequently the three lowest hole states are $1S_{3/2}$, $1P_{3/2}$, and $2S_{3/2}$. The presence of these states has been experimentally

confirmed by Klimov et al. through transient absorption measurements of carrier relaxation dynamics [37]. The energy of the electron-hole interaction is proportional to the electron and hole wave function overlap, which is strongly enhanced in the close confines of a quantum dot. Consequently, in the presence of this strong exchange interaction the lower energy states within the nanoparticle are coupled and cannot be considered independently, and should be considered as combined exchange-correlated excitons with a combined total angular momentum. This situation is further complicated in non-spherical nanocrystals where the energy structure due to breaking of symmetry results in splitting of the band-edge exciton fine structure. This results in perturbation of the energy state degeneracy which splits the exciton ground state into an optically "dark" triplet state and a "bright" singlet state [38,39]. The presence of this additional fine structure in the excitonic bands of the nanoparticle can be used to explain the strong temperature dependence observed in time resolved photoluminescence decay measurements made at various temperatures. At liquid helium temperatures the decay lifetime ranges from hundreds of nanoseconds up to approximately 1 microsecond, whereas this value decreases at room temperature to a value around 20ns [38,40,41]. The presence of the "dark" triplet state, which lies at a lower energy state than the "bright" singlet state acts as a trap for carriers when the phonon population in the lattice is low. This restriction is relaxed as temperatures are increased both through thermal promotion of carriers up into the singlet state as well as increased phonon meditated relaxation of the triplet state down to the ground level. Under conditions of intense excitation it has also been shown that relaxation of photo generated multiexcitons is strongly influenced by

nonradiative energy loss via Auger recombination [42]. At suitably high excitation intensities this can be seen as a rapid decay of the carrier populations, which is very quickly changed to a much slower decay after the initial onset of relaxation. In practice the intrinsic radiative decay properties of the quantum dot core are further complicated by the presence of various defects within the semiconductor structure, as well as the close proximity of the surface, which lies within range of the electron and hole wave functions. Impurities, defects and other trapping sites at the core-shell interface as well as vacant bonds and surface attachment of undesirable elements can significantly perturb quantum dot behavior if not carefully controlled. The intrinsically rich excitonic structure of the quantum dot combined with these additional effects results in complex decay dynamics, which can only be described by simultaneous contributions from multiple sources.

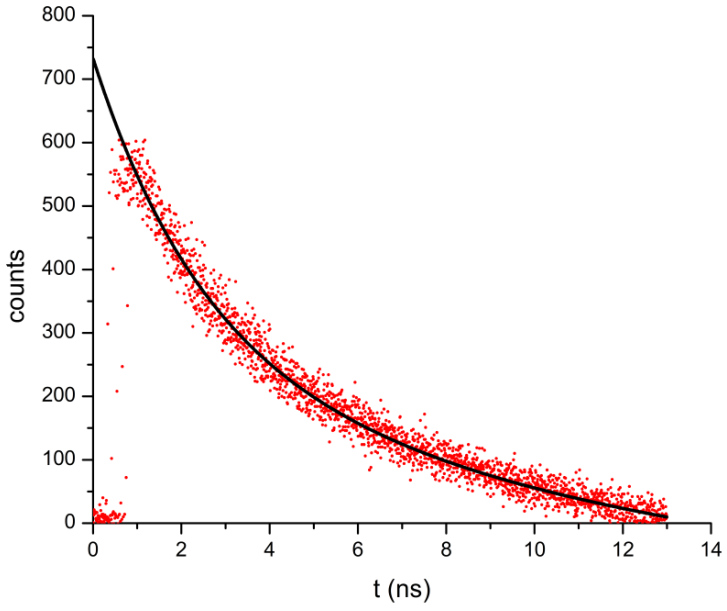

Figure 17 Radiative decay curve measured using time correlated confocal fluorescence microscopy. Measured data shown in red exhibits clear multiexponential behavior and correlates well to a biexponential fit illustrated in black. A short lifetime of of 2.4ns and long lifetime of 13.3ns are extracted from the fit.

Figure 17 illustrates the complex nature of quantum dot relaxation dynamics typically observed in optical measurements of their decay lifetimes. Many groups have reported fluorescence lifetime measurements supporting this behavior and efforts to fully understand the origin of the various decay dynamics at work in these nanoparticles are a continuing area of investigation [43,44]. As previously stated contributions to the lifetime from "dark" and "bright" exciton states have been experimentally demonstrated using low temperature measurements of the Stokes shift between absorption and emission as well as the magnetic field dependence of the decay behavior [38,39]. Temperature dependence measurements have shown that while extended lifetimes are observed at temperatures in the liquid helium range (~3-9K) the component of the lifetime that can be attributed to relaxation of these excitonic states is significantly reduced at increased temperatures [41,45]. The lifetime has been observed to increase for temperatures up to 70K above which the value saturates and remains fixed [41] which is consistent with emission from a three level system with a weakly emitting lower state and a strongly emitting higher state as in the "bright" and "dark" exciton model. This can be attributed to thermalization of the lower state, which occurs more efficiently at higher temperatures and on a shorter time scale relative to the long triplet relaxation lifetime. The effects of surface morphology on the decay lifetime components has been studied by many groups and correlations between longer lifetime contributions and modification of the surface have been illustrated in many of these results [45,46,47,48,49]. Deliberate exposure of nanocrystals to oxygen [48] and controlled photooxidation [46] have shown that longer lifetime components of the radiative decay are likely associated with migration

of delocalized carriers inside the core to the outer surfaces of the particle where they are affected by the presence of defects and other surface effects. This is in contrast to the shorter contributions, which are typically associated with the intrinsic excitonic structure and are unperturbed by deliberate surface perturbation [48]. Other results have shown that the surface ligands that are used for passivation to terminate loose bonds at the surface can strongly affect quantum dot relaxation properties [49]. These types of behavior suggest that while recombination within the core of these particles can be well explained by exciton spin states, the overall particle dynamics are a complex mixture of intrinsic properties along with empirical effects derived from the quality of synthesis, as well as less controllable factors such as adsorption of impurities at the dot surface. These effects can be further complicated by effects such as the Quantum-confined Stark effect, which has been observed to modify the emission properties of quantum dots based on the presence of internal fields generated by carriers distributed within the core [50,51]. Finally, it has been shown that the quantum yield and lifetime of individual quantum dots can vary over time for the same particle [52] on short time scales. While a basic theoretical description of quantum dot decay mechanics has been presented in the literature for some time and verified by many experimental results, the dynamical and multifaceted nature of the overall decay process has prevented the emergence of a comprehensive description. This has important consequences for many applications including the use of quantum dots as substitutes for fluorescent dyes which will be discussed in Section 3.3.

3.3 Comparison to Fluorescent Dye

Fluorescent materials have found widespread application in the life sciences for their ability to provide fast and consistent detection of biomolecular interaction in a reliable and reproducible fashion. The majority of materials used for this application have normally included small organic dyes, metal-ligand complexes, lanthanide chelates, and biologically derived fluorophores such as fluorescent proteins like green fluorescent protein (GFP). Over the course of their use, these materials have been studied extensively and a complex understanding of their mechanics and properties has been developed. Unfortunately, these studies have also illustrated some of the shortcomings that can lead to undesirable effects or make them difficult to work with. The optical properties of fluorescent dyes are dependent on the electronic and vibrational transitions involved in the absorption and emission process. Emission in most common dyes originates primarily from singlet S_1 to singlet S_0 transitions of π electrons in ring structures in the molecule, or intramolecular charge transitions in CT dyes [53]. Ring-based dyes encompass most of the commonly used organic dyes and are characterized by closely spaced asymmetrical emission and absorption peaks, which are spaced by a small Stokes shift and emission spectra that are broadened on the red-shifted side. Unfortunately, due to the discrete nature of the transitions involved in organic dye photo-dynamics the spectrum of usable pump wavelengths is limited to a relatively small region around the absorption peak. In addition, for most common dyes the spacing between the absorption and emission peaks is only around 50-100 nm with some overlap occurring for wavelengths falling in the region between the peaks, which favors cross-talk between individual dye molecules [53].

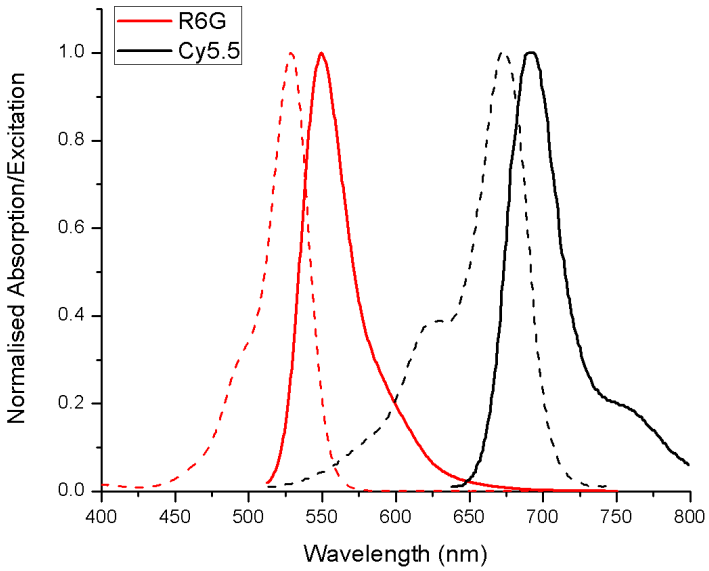

Figure 18 Absorption (dotted) and emission (solid) spectra for Rhodamine 6G (red) and Cyanine 5.5 (black) from [54].

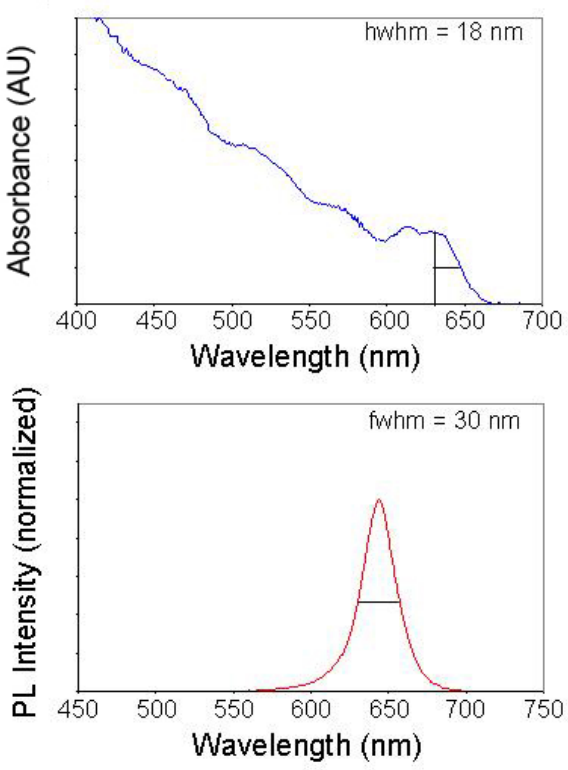

Figure 19 Absorption and emission spectra for CdSe/ZnS core/shell quantum dots. From NN-Labs CZ640 [55].

These features are evident in the spectra of Rhodamine 6G and Cyanine 5.5 and are presented in Figure 18 where the close spacing of the absorption and emission peaks is clearly visible along with the asymmetry of the peaks. A direct consequence of these properties is difficulty in selecting viable fluorescent dyes for use in spectrally multiplexed applications. For this type of application it is desirable for a single excitation wavelength to be used to excite multiple fluorophores, which can then be distinguished by examining their emission spectra and separating labels by their individual emission wavelengths. Use of organic dyes clearly presents two obstacles in this situation. First, given the close proximity of the absorption and emission spectra of most dyes it is very difficult to find a selection of dyes across a broad range of wavelengths that can all be excited using a single wavelength. This is further complicated by the necessity for the pump signal to be located as far as possible from the emission wavelengths in order to prevent the pump channel from leaking into the desired measurements. Aside from these spectral considerations, in applications where long time exposures are required the inherent susceptibility of organic dye materials to photobleaching under conditions of prolonged exposure to optical stimulus can make it difficult to obtain meaningful data. As an example, emission from the fluorophore Alexa 488 has been experimentally shown to drop off rapidly from the onset of excitation and decays sharply within the first 60 seconds to less than 20% of its initial intensity, which can be seen in Figure 20B.

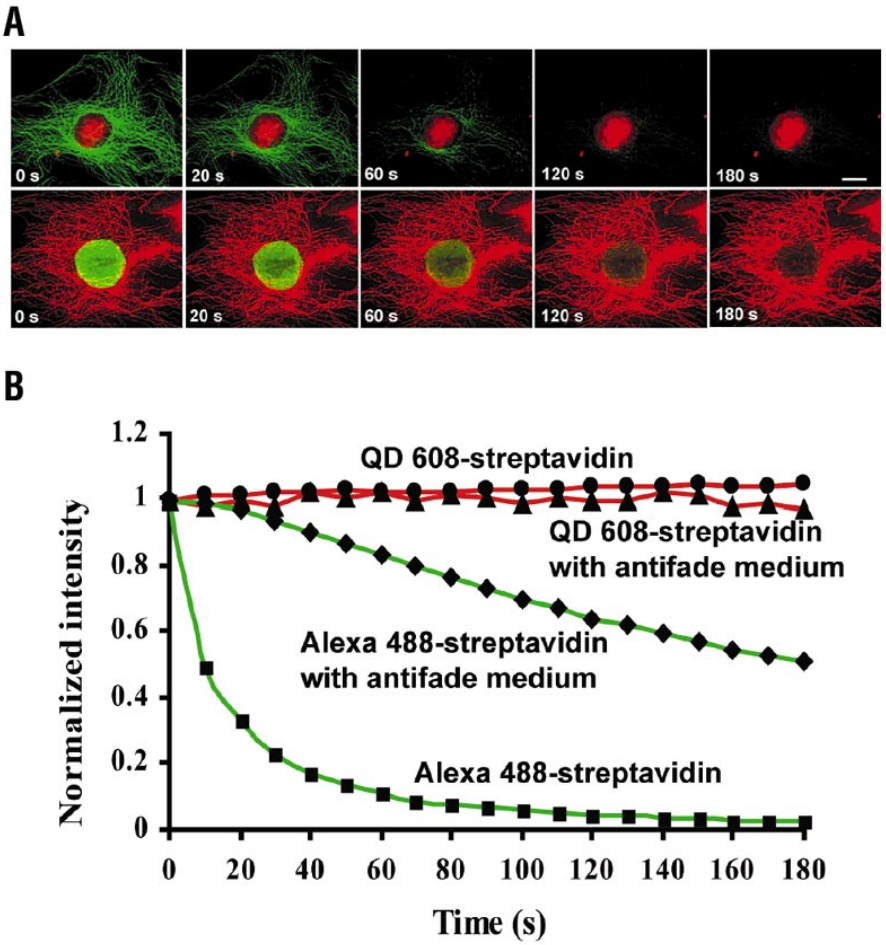

Figure 20 (A) Top row: Nuclear antigens labeled with QD 630–streptavidin (red), and microtubules labeled with AlexaFluor 488 (green) simultaneously in a 3T3 cell. Bottom row: Microtubules labeled with QD 630–streptavidin (red), and nuclear antigens stained green with Alexa 488. (B) Quantitative analysis of changes in intensities of QD 608–streptavidin (stained microtubules) and Alexa 488–streptavidin (stained nuclear antigens) using specimens mounted with glycerol or antifade mounting medium Vectashield. Reprinted from [56]

The use of quantum dots as a substitute for organic dyes in fluorescence imaging applications offers an alternative solution which can address some of these considerations. Quantum dot emission spectra are typically narrow and symmetric without the structure and asymmetric tail associated with many dyes. This is coupled with a small excitonic absorption peak that is blue shifted relative to emission and

more importantly increasing absorption for shorter wavelengths below the first absorption band. Size controlled tunability of the absorption and emission peak positions allows the spectral properties to be tailored to specific applications while still maintaining the same material system. Molar absorption coefficients for quantum dots are also generally large when compared to organic dyes [53,57] and exhibit high quantum yields for wavelengths from the visible all the way to the NIR region. This advantage is particularly pronounced for wavelengths in the NIR band where organic dyes suffer from poor quantum yields and limited photostability [53]. The wide absorption spectrum of quantum dots enables selection of pump sources from a wide variety of wavelengths. This, in turn, makes it much more straightforward to utilize pumps that are spaced spectrally far from the emission peak thereby reducing or eliminating pump signal crossover into the wavelength regime of interest, something which is difficult or impossible to implement using organic dyes. Taking advantage of this capability makes spectrally multiplexed measurements using a single pump wavelength relatively direct compared to dyes, provided that a suitable source can be selected for the emission wavelengths of interest. Photostability in quantum dots is also greatly improved over organic dyes as noted previously. Due to their inorganic surface layers and shielding of the core material by using epitaxial shell layers quantum dots are significantly more resistant to thermal and photochemical degradation as shown in Figure 20. This is especially important for applications requiring high intensity excitation or long term exposure of samples, and has been experimentally verified in various studies [53,58]. The need for surface passivation layers on the surface nanoparticle can be of advantage when

functionalizing the particles to facilitate selective attachment to target analytes both by tailoring the surfactant layer as well as attaching additional molecular chains to whatever layer is already in use. While quantum dots offer many potential advantages, these advancements do not come without corresponding difficulties. Quantum dots are generally characterized by complex carrier dynamics, discussed in Section 3.2, which can introduce severe complications for applications where discrimination of multiple probes through non-spectral means is desirable. In addition, interactions between the dots and their surrounding environment are not fully understood, especially in the context of carrier dynamics occurring at the surface of the particle. Geometrically the dots are much larger than the corresponding dyes and typically range from 1-50nm in diameter in comparison to molecular dyes, which are often dimensionally on the scale of angstroms. This can cause problems for introduction of dyes into cells or other small structures without collateral damage to the target assembly. Additionally, many of the materials used in quantum dot synthesis are highly toxic and care must be taken to prevent leeching of the quantum dot constituents into the surrounding environment. In spite of these considerations quantum dots have found increasing application in many areas thanks to their versatility and capability to provide improvements in stability and spectral output.

4 Fluorescence Enhancement

The presence of strongly enhanced fields near the metal-dielectric interface is one of the properties that make application of surface plasmon effects attractive. As described previously in Section 2.4 if the requirements for surface plasmon excitation can be appropriately satisfied it is possible to achieve field enhancement of several orders of magnitude simply by the presence of surface waves at the interface. The performance of optically active materials placed in close proximity to the interface thus has the potential to subsequently experience enhancement of their performance through exposure to these intense fields. One of the areas which has garnered significant attention in recent years is the application of surface plasmon supporting structures and interfaces for the enhancement of fluorescence yields from dyes and other materials placed near metallic interfaces and nanostructures [21,22,23,59] . However, the study of these effects involving surface plasmons and such materials is fundamentally complicated due to the inherent need to use metallic structures, which perturb the behavior of such emitters by their very presence. It is well known from past studies that emitters placed in close proximity to metallic surfaces can experience quenching of their fluorescence, which occurs as a function of the source-interface separation. It is therefore of critical importance when studying the interaction of surface plasmons and fluorescent emitters that care is taken to consider the complex interplay between the advantages offered by the enhanced surface field and degradation of system performance from the presence of a strongly absorbing medium. In order to understand the results, a basic understanding of how fluorescent materials interact with these surfaces is a logical starting point.

4.1 Fluorescence Near Metallic Interfaces

The behavior of fluorescent materials placed in close proximity to metallic interfaces can be altered drastically in comparison to their behavior in a uniform non-absorbing medium. Depending on the geometry of the system and the surrounding materials decay of the excited fluorophore can exhibit either an increase or decrease in time response as well as radiative efficiency. Interaction with the boundary causes modifications to the way the excited molecule loses energy by altering the local conditions experienced by the emitter. First, by modifying the boundary conditions of the electromagnetic field both the radiative decay rate and spatial distribution of radiation can be altered. Next, the presence of the boundary may provide a route for the excited particle to lose its energy through non-radiative energy transfer. In the simplest case the emission properties of a fluorescent emitter can be considered as an excited dipole, which will relax by converting its energy to a photon or transferring it to another excitation. The effect that the presence of the metal will have depends on both the properties of the material as well as the relative distance and orientation of the dipole with respect to the boundary. Theoretical investigations of dipoles near dielectric and metallic interfaces have been presented in the literature [60,61,62,63,64,65] and have illustrated how the field structure and spatial distribution of emission from a dipole is altered under such conditions. However, more interesting from the standpoint of fluorescence enhancement effects is the effect that the metallic interface has on the decay lifetime of fluorescent emitters. Fluorescence is an example of the spontaneous emission process, which means that the probability of spontaneous emission can be given by Fermi's golden rule [66] as:

$$\Gamma_{ij} \propto \left|M_{ij}\right|^2 \rho\left(\nu_{ij}\right) \qquad [4.1.1]$$

Here Γ_{ij} is the rate for transitions between the excited state i and the lower-energy state j, M_{ij} is the matrix element corresponding to the transition between these energy levels, and $\rho_{ij}(\upsilon_{ij})$ is the density of states at the transition frequency, which we can be referred to as the photonic mode density (PMD). This correlation between spontaneous decay rate and PMD was first pointed out by Purcell in the context of radio frequency emission from nuclear magnetic moment transitions coupled to a resonant electrical circuit [67]. Modification of the matrix elements M_{ij} would require that the interface perturb the emitter wavefunction. While possible, it is highly unlikely that this will occur as such interactions would require angstrom-scale separations. Therefore, it is primarily through modification of the photonic mode density that we would expect the interface effects manifest themselves. Experimental work characterizing the behavior of fluorescent emitters in the presence of a planar interface was pioneered by Drexhage [68,69,70,71,72] in the 1960's with subsequent contributions from other groups in later years [60,73,74,75,76,77]. These measurements demonstrated that significant modification of the spontaneous emission lifetime occurs as well as a strong dependence of the lifetime modification on the emitter-interface separation. Figure 21 illustrates the behavior typically observed in experiments of this type. From the figure it is clear that the emission lifetime has a strong dependence on the interface separation, which approaches a steady state value at larger distances corresponding to the lifetime of emitters in a homogeneous medium.

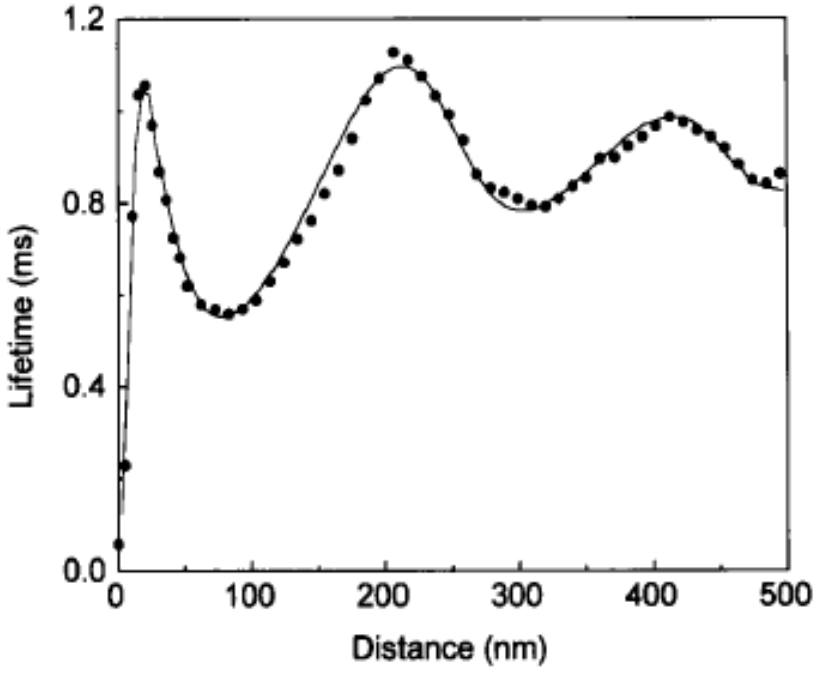

Figure 21 Lifetime of Eu^{3+} ions in front of a silver mirror as a function of separation between Eu^{3+} ions and the mirror. Reprinted from [74]

At shorter distances the lifetime experiences a sharp decrease once the separation drops below 50 nm, which corresponds to strong quenching of the fluorescent emission. For larger separations the spontaneous emission lifetime can clearly be seen to oscillate around the isotropic value and this can be explained by considering constructive and destructive interference between fields emitted by the dipole and fields which are emitted then reflected back by the metallic interface. In order to understand this effect we can consider a dipole placed near a mirror as depicted in Figure 22. The presence of the metallic interface affects both the spatial distribution of radiation as well as the lifetime for emission of radiation. Changes to the spatial distribution of emitted radiation can be described by considering the two cases shown in Figure 22(a) and (b). Radiation emitted from the dipole interferes with part of the emitted light that is reflected by the metal surface.

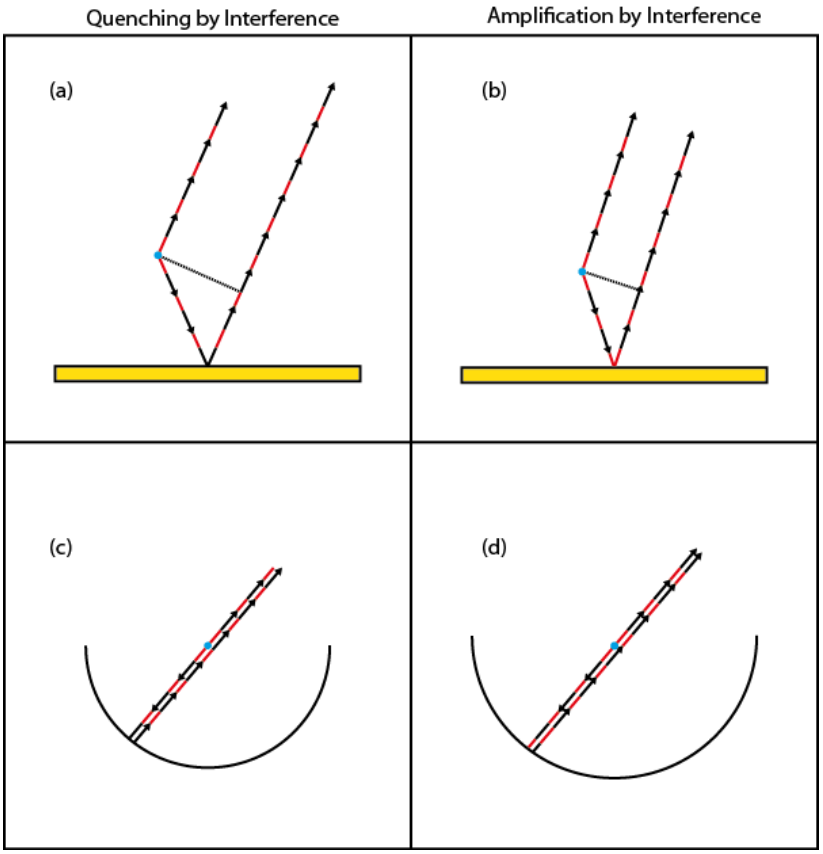

Figure 22 Amplification and quenching of a dipole (shown in blue) near a metal surface. Interference between fields emitted from the dipole and reflected fields causes modification of the angular distribution of emission (a)-(b) as well as the decay lifetime (c)-(d). [68]

If the angle is such that the reflected light returns 180 degrees out of phase from light leaving the dipole as in (a) then radiation from the dipole into that direction is quenched and will not occur. Conversely, if the reflected light returns to the source in-phase then the power radiated in that direction is doubled and emission at such an angle is amplified. A similar argument can be made when considering the lifetime for emission from a dipole near the mirror's surface. If the dipole is placed at the center of a spherical mirror instead of a planar mirror then the same effect can be extended for all points in the upper half-space as in (c) and (d). If the radius of the mirror is an integer multiple of a wavelength light that is reflected from the mirror

surface interferes destructively with emission from the dipole resulting in quenching of all emission in the upper half space outside the mirror. As a result the dipole is unable to radiate its energy and it will remain in its excited state infinitely in the absence of nonradiative deactivation processes. Similarly if the radius of the mirror is instead taken as an odd multiple of a half wavelength then constructive interference occurs resulting in a doubling of the field amplitude at the dipoleand correspondingly the probability for radiation would increase by a factor of four since radiated intensity is proportional to the square of the amplitude. The fluorescent decay of an emitter above a plane mirror is affected in a similar manner and produces the characteristic oscillation of the emitter lifetime observed for larger distances in Figure 21. For small separations between the dipole and metal near-field coupling between the excited dipole and loss channels within the metal has a strong influence on emission lifetime. This effect manifests in Figure 21 as a rapid decrease in fluorescence lifetime as the particle approaches the metal surface and results in strong quenching of emitters residing directly at the interface. For a planar metallic interface the dipole transfers its energy primarily into surface plasmons or lossy evanescent fields depending on the degree of separation and dipole orientation [60]. Here, the presence of the surface plasmon mode increases the photonic mode density by creating an additional pathway for the dipole to lose its energy non-radiatively and contributes to losses in the system. For very small separations the near field of the dipole couples increasingly into evanescent waves propagating into the metal where the energy is dissipated by the material losses.

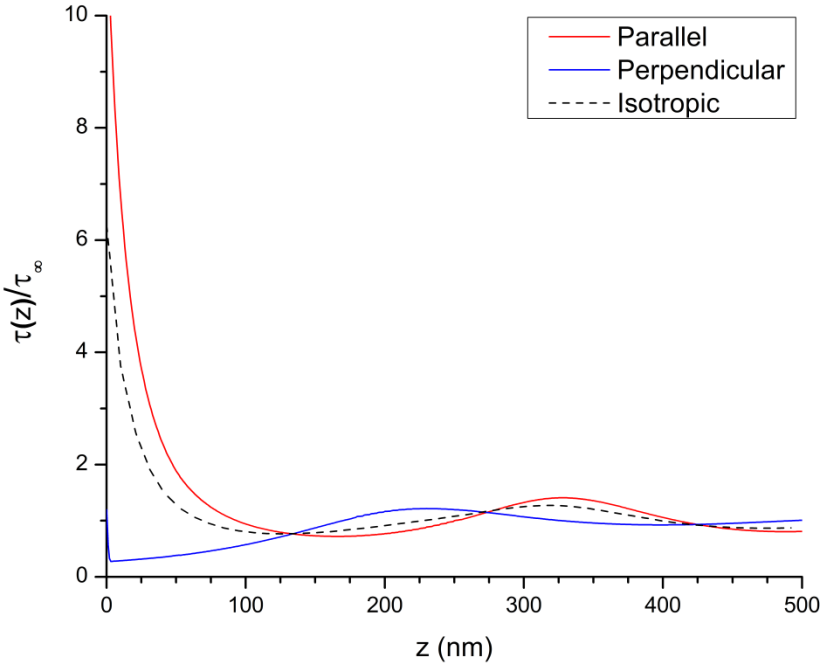

Figure 23 Modification of fluorescence lifetime for a dipole above a gold-air interface emitting at 640nm calculated using Lumerical FDTD simulation software [78].

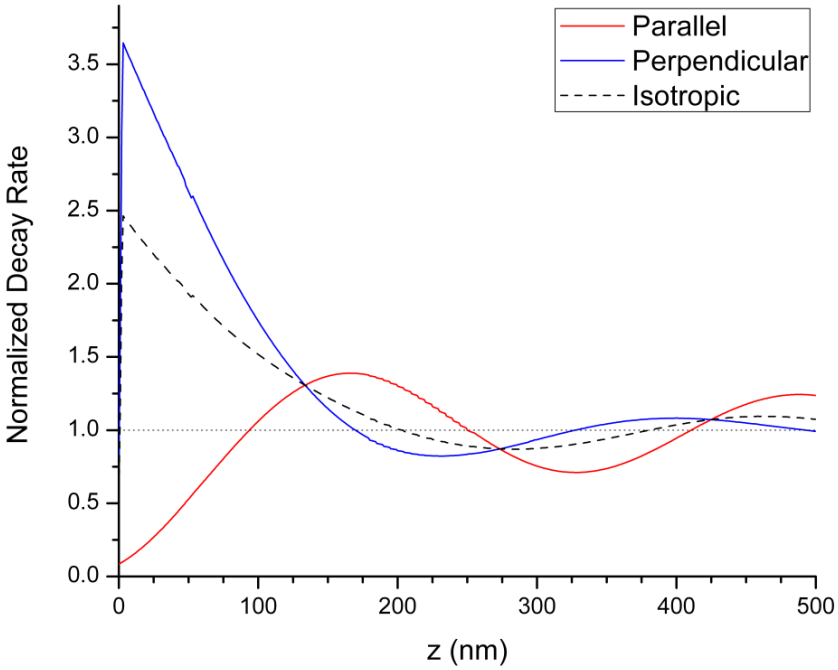

Figure 24 Modification of spontaneous decay rate for a dipole above a gold-air interface emitting at 640nm calculated using Lumerical FDTD simulation software [78].

As a result, the dipole is strongly quenched as it rapidly loses any excitation by conversion to surface plasmons or radiation into the metal. The degree of lifetime modification that a dipole experiences in the presence of a metal or other surface can be determined by examining changes in the power radiated by a dipole in a given configuration. Since the excited dipole has a finite amount of energy its lifetime is inversely proportional to the total radiated power.

$$\tau(z)/\tau_\infty \propto P_\infty/P(z) \qquad [4.1.2]$$

This property allows us to predict the lifetime behavior of a fluorescent emitter as long as the emitted power for a dipole can be determined in the desired configuration. Calculations made using the Lumerical commercial FDTD simulation software [78] are presented in Figure 23 and Figure 24 for a dipole over gold oriented parallel and perpendicular to the interface. In a more practical setting the dipole orientation is often randomly distributed across the surface. Under these conditions an average over the dipole orientations can be obtained by taking the average of the lifetime for a perpendicular orientation plus twice the value for a dipole oriented parallel to the interface which is depicted by the dotted black line.

4.2 Enhanced Emission vs. Enhanced Absorption

The enhancement of fluorescent emission can be separated into two categories based on the nature of the underlying physical phenomena that facilitate the increase in photon flux. As discussed in Section 4.1 modification of the local photonic mode density has a strong effect on the lifetime of emitters. Introduction of additional nonradiative decay channels causes a reduction in the efficiency of radiation from the emitter out into the surrounding media. Under normal circumstances the presence of

these additional losses has a negative impact on the performance of fluorophores and results in a reduction of the net photon flux. However, depending on the properties of the emitter and the geometry of the system it is possible to observe an increase in emission in spite of the additional losses in the system. An example of this can be seen when considering a fluorescent particle with low quantum efficiency and long lifetime near a gold surface. For this type of situation the emitter has a high chance to lose its energy to a non-radiative process instead of by photon emission, but remains excited for an extended period before it can be excited again. When looking at the distance dependence of the fluorescence signal, whether it is enhanced or reduced depends on two competing factors. On one hand the presence of the metal film introduces pathways for nonradiative loss, which reduce the radiative efficiency of the particle. This would most likely be detrimental if the emitter had either high efficiency or a short lifetime or both but in this situation the reduction in the overall lifetime can open up the opportunity for enhancement to occur. Since the lifetime of the source is long, reduction of the lifetime results in increased availability for the emitter to absorb an incoming photon. In this way it can be possible to increase the overall photon flux by increasing the number of opportunities for the emitter to produce a photon despite reductions in the overall efficiency. Alternatively, the presence of a resonant structure can be used to transfer the excitation and either transfer energy back to the emitter or facilitate conversion into a photon by scattering or other processes. If the fluorescence enhancement can be attributed to the influence of the local environment on the emission properties of the source then such an effect can be attributed to enhanced emission. In contrast, it is also possible to increase the

observed fluorescence from a source by modifying the fields to enhance the driving field seen by the emitter. In this case, the observation of enhanced fluorescence signals occurs due to modification of the local environment without perturbation of the fundamental behavior of the source. For such a situation the fluorescence enhancement is said to be caused by enhanced absorption effects. Discrimination between these two effects can be done by examining the spectral and time correlated behavior of fluorescent emission, as well as the conditions under which enhancement is observed. Modification of the source lifetime can be observed using time correlated methods and manifests as an increase or reduction as in the case of an emitter above a mirror. Aside from the case of a planar interface the additional photonic modes are often introduced by the presence of a cavity or structure that has its own frequency dependent response. In such a situation, coupling between the source and structure occurs only when the spectral output matches the frequency response of the structure. Measurements of the spectral emission will then exhibit increased signal at frequencies corresponding to the optical response of the structure. Experimental [21,22] and theoretical [79,80,81,82] studies of enhanced emission effects have shown that appreciable enhancements can be obtained for low efficiency sources but that high efficiency sources exhibit little benefit from such techniques. High efficiency sources can, however, benefit from enhanced absorption type effects depending instead on how efficiently they are able to absorb incident radiation. This can be an important consideration when observing the performance of quantum dots, as core/shell configurations typically exhibit high quantum efficiency compared to bare cores which can have very poor efficiency due to carrier dissociation to the

interface. Finally, since enhanced emission effects arise due to interaction between the emitter and its local environment they should occur consistently regardless of the orientation of the exciting source provided that selectivity in the emitter's absorption properties is taken into account. As a consequence distinction between the two effects can be made by observing the effect that orientation of the sample has on the observed fluorescence signal.

5 Surface Plasmon Enhanced Fluorescence on Nanostructured Gold Surfaces

5.1 Introduction

Over the course of the past decade surface plasmon polaritons (SPP's) have garnered increasing attention in the scientific community. These surface wave solutions to Maxwell's Equations at the boundary between semi-infinite dielectric and metallic regions are localized and propagate in the plane of the interface. The characteristic strongly enhanced fields near the boundary, which decay exponentially away from the surface, offer an attractive means for enhancing the performance of optical interactions. Field enhancement near the boundary plays a critical role in surface enhanced effects with enhancements reaching up to 100 times or greater compared to propagating waves in either medium [83]. This strong local field enhancement near plasmonic structures and surfaces supporting SPPs is capable of significantly enhancing optical effects which take place in the vicinity of the boundary. Fluorescent materials have found widespread application in the life sciences as probes that provide fast and consistent detection of biomolecular interactions in a reliable and reproducible fashion. Regardless of the measurement technique used, the fluorescence intensity produced by a fluorescent probe is of key importance in determining its capability to provide specific detection of materials of interest in the presence of unknown amounts of other substances. Techniques that enhance fluorescent emission can reduce measurement times, increase sensitivity, or reduce the amount of material required for accurate detection. It is well known that the

presence of a metal surface in close proximity to a fluorophore can significantly modify its emission [60,84]. This has been attributed to several factors but depends strongly on the distance separating the fluorophore and metal. For large separations, fluorescence is not affected and behaves as it would in free space. As separation decreases, increased nonradiative relaxation of the excited fluorophore occurs as energy is coupled into surface plasmons (SPPs or localized plasmons) on the surface of the metal. For very small separations, quenching of emission is well known and is attributed to damping of dipole oscillators and coupling of energy into evanescent waves at the surface of the metal. While coupling to surface plasmons is viewed as an undesirable loss mechanism for experiments that rely on emission from fluorophores, the interaction of surface plasmons with fluorophores may be used to modify and enhance their utility. Coupling of excited fluorophores into surface plasmons is well known to occur for intermediate metal-particle separations [60]. This effect is the basis for surface plasmon coupled emission (SPCE) [85,86,87] which takes advantage of coupling between excited emitters and surface plasmons to excite surface plasmons that are then scattered into photons and detected. By placing emitters in close proximity to surface plasmon-supporting substrates it is also possible to increase their emission by taking advantage of localized high surface fields. Fluorescent enhancement by localized plasmons excited in metallic nanoparticles has also been a topic of active research for several years [23,88,89]. Experimental studies have shown over 20 times enhancement in emission intensity for emitters coupled to surface plasmon supporting nanoparticles compared to sources placed on glass or other non-plasmon supporting substrates [21,22,23,88,89]. SPPs propagating on the

surface of a metal film may also be used to produce a similar enhancement effect if the fluorescent material is placed in close proximity to the films. However, the use of SPPs in this way imposes phase matching restrictions that constrain the conditions for SPP excitation. As explained in previous chapters, the surface plasmon wavevector component parallel to the boundary is greater in magnitude than the wavevector of light in either of the bounding media [90], which requires additional phase matching structures to enabling coupling into SPPs. Surface gratings allow us to provide the additional momentum for coupling incident photons into surface plasmon excitations without the additional complexity required for prism coupling schemes. Fluorescence enhancement using grating-coupled SPPs has been demonstrated previously by Hung *et al* [59] and Tawa *et al* [91] using commonly available fluorescent dyes placed onto substrates patterned with periodic grating structures. In both of these experiments it has been shown that enhancement of fluorescent emission was due to excitation of SPPs propagating along the grating surface. The results detailed here will serve to extend and refine the results of these previous studies by examining the performance of quantum dots placed in close proximity to dielectric gratings patterned onto a planar surface plasmon supporting metallic interface. The purpose of doing so will be to examine the conditions under which enhanced fluorescence can be obtained and to illuminate the underlying physical phenomena which contribute to the effect.

5.2 Experiment Design

In this work PMMA surface gratings defined using EBL patterned onto the surface of gold coated substrates are used to excite surface plasmon polaritons at the metal film surface. The use of such periodic phase matching structures is known to be effective

for exciting surface plasmons as demonstrated in the literature [11,83] and discussed in Section 2.3.2. Samples are fabricated using thin glass cover slips that have been sputtered with a 50nm thick film of gold on one surface to support surface plasmon propagation. Chromium adhesion layers are omitted from fabrication due to sufficient wetting of the surface from plasma cleaning during film deposition. After deposition of the gold film the samples are then spincoated with either PMMA (Microchem PMMA495A4) or a composite mixture consisting of PMMA and CdSe/ZnS QDs in Toluene to a thickness of approximately 150nm. Grating structures are defined using a Raith E-line EBL system and structures are subsequently developed using a 3:1 IPA:MIBK solution, (also from Microchem) as developer. Depending on the sample, introduction of QDs is performed by deposition of a PMMA/QD mixed composite or by low speed spincasting before exposure and development of the grating pattern via EBL. The distinction between these introduction methods will be discussed in more detail later. QDs used for the experiment are obtained commercially from NN-Labs and consisted of CdSe/ZnS (NNLabs CZ640) dots suspended in toluene with emission peak at 640-660nm. These QDs are high quantum efficiency fluorescent emitters with radiative efficiencies in the range of 40-50% as specified by the manufacturer which agrees well with values presented in the literature[92]. Prior to deposition the solution containing QDs is further diluted from its original concentration to 10^{-3} M CdSe in toluene. Because of solubility considerations, QDs that have been deposited onto the surface of the sample prior to electron beam patterning will primarily remain on the sample as they are insoluble in the developer solution and are not carried away. The

resulting samples consist of unpatterned regions consisting of QD-coated resist combined with patterned regions defined in the film with QDs coating both regions. The use of EBL allows the physical parameters of the gratings to be controlled very precisely with nanometer scale precision. When coupled with high resolution nano-imaging techniques such as AFM and SEM individual parameters of the grating structure can be independently varied while maintaining tight control over the remaining properties. This capability is crucial for enabling the isolation of individual physical parameters in order to study their effect on the fluorescence enhancement phenomena.

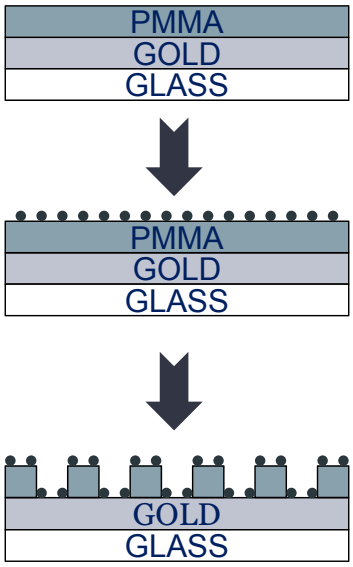

Figure 25 Illustration of fabrication steps used in sample preparation. Gold and PMMA films are deposited onto glass cover slips as substrates. Quantum dots are then spincoated onto the resist surface at low speed from 1mM solution in toluene. Finally, EBL is performed to define patterned regions and create QD-coated linear gratings.

Sample analysis is performed using standard fluorescence optical microscopes (FOMs) with no additional special optics required. For imaging of the samples both a Leica MZFLIII and Leica INM100 FOM are used. Light for fluorescence excitation

on both microscopes is provided by a mercury discharge lamp filtered to provide the appropriate excitation wavelength range. The MZFLIII is equipped with filters for observation using excitation in the green at 400-540 nm and emission in the red at 600-680 nm and uses a 1.0x plano objective with N.A. 0.125. For the INM100 a filter set for red excitation at 596-634 nm and emission at 653-702 nm is used with a 20× Leica Fluotar objective with N.A. 0.4. Image analysis was performed using the Gwyddion [93] AFM image analysis package to extract profiles as well as statistical measurements of image values with associated errors. Samples required no special preparation prior to imaging and proved resilient to long-term exposure for periods of time exceeding three hours without noticeable degradation of fluorescence signal. The application of the nanostructured substrates presented here is straightforward, requiring no special hardware outside commonly available standard fluorescence measurement equipment.

5.3 Quantum Dot Deposition

In order to examine the potential for application of this technique to fluorescence from quantum dots several samples were fabricated using gold, chromium and ITO film substrates in order to distinguish between enhancement due to surface plasmons and other effects such as guided modes and enhancement due to the presence of gratings. The control materials chromium and ITO were selected due to their optical properties at the wavelengths of interest. Examination of the dielectric constant of chromium, -12.33 - 24.53i in the green [15] and -6.90 - 30.35i in the red [14], indicates that while chromium may support surface plasmons at these wavelengths the high absorption of the material in this range causes them to decay rapidly and thus

we treat the material as a non-SPP supporting material. ITO, on the other hand, supports SPPs at longer wavelengths [94] but does not support plasmons in the wavelength region of interest being transparent in this range. The control samples were fabricated by substitution of a 50nm thick chromium layer in place of the usual gold layer for chromium samples. ITO samples used commercially acquired ITO on glass substrates with the ITO layer of indeterminate thickness. Unlike gold and chromium the thickness of the ITO layer is less important as ITO is transparent at the wavelengths of interest. These initial samples were coated using a composite resist solution consisting of a 50:50 combination of PMMA495A4 in anisole and 10 mM quantum dots in toluene. Samples were subsequently patterned with a test pattern consisting of square regions containing linear dielectric strip gratings of various periodicities along with triangular marks denoting the upper edge of the pattern for image recognition under the microscope as depicted in Figure 26a. Observation of the resulting patterns was performed using the MZFLIII fluorescence optical microscope with a camera gain setting of 16. The images, shown in Figure 26, demonstrate a clear distinction between the application of the composite material to surface plasmon supporting substrates and non-plasmon supporting materials. A significantly stronger fluorescence signal can be clearly identified when viewing the sample containing a gold thin film when compared to both of the control substrates. We must note, however, that the chromium coated substrate does exhibit low levels of enhanced fluorescence in the regions where gratings have been fabricated.

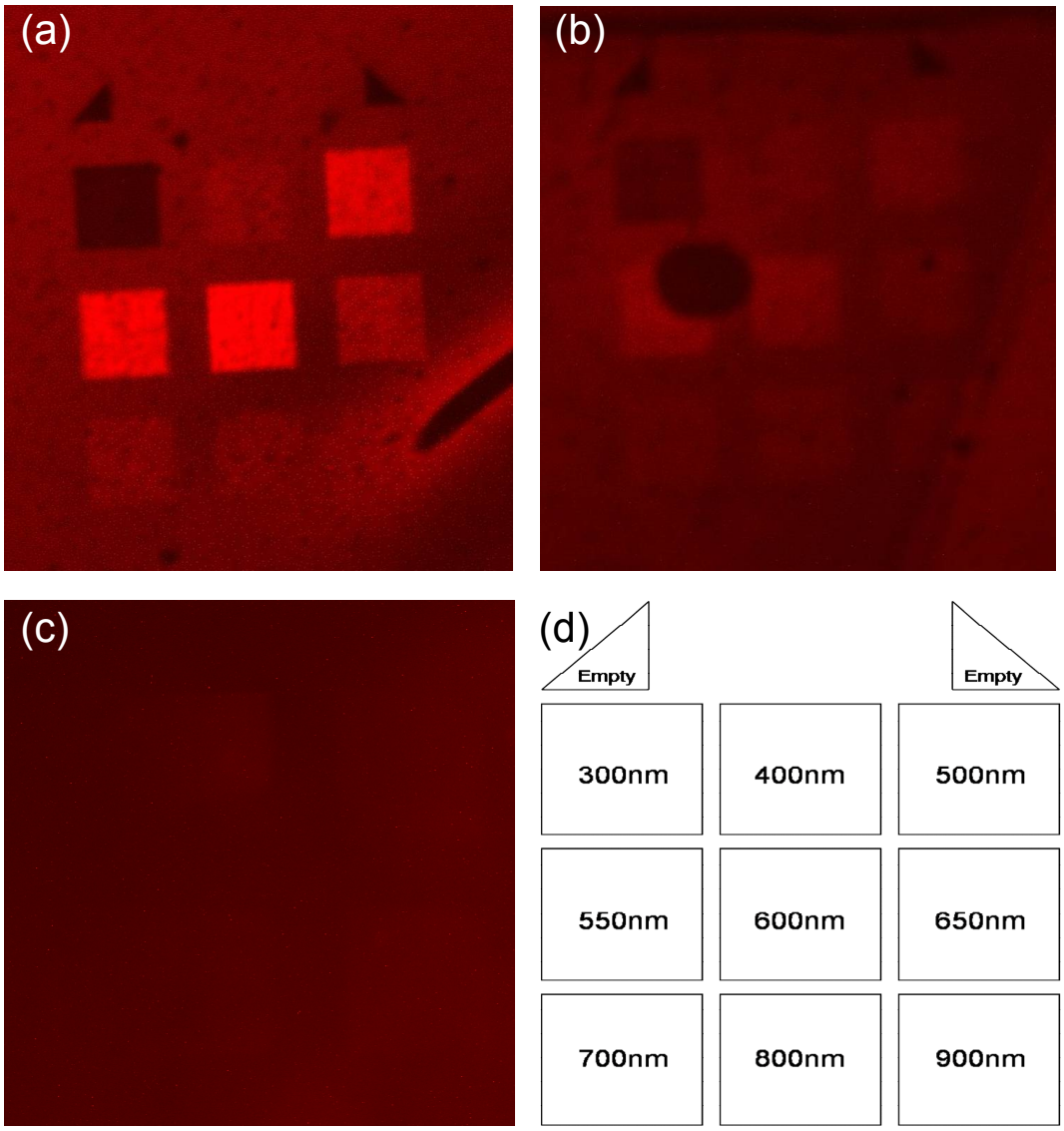

Figure 26 Samples coated with a PMMA/QD composite mixture on different substrates using a CCD camera gain setting of 16. (a) Gold substrate, integration time: 240 s. (b) Cr substrate, Integration time: 300 s. (c) ITO substrate, integration time: 300 s; the gratings visible correspond to the bottom right corner of the pattern. (d) Schematic of test pattern layout with grating periodicities.

This behavior can be attributed to the possibility that the gratings may provide enhancement of fluorescence due to evanescent field interactions from the presence of the corrugated surface, and also to the potential for surface plasmons on the metal surface, however short-lived they may be due to the strong absorption. Finally, for the case of ITO, which is transparent and does not support surface plasmon excitation, the grating regions have very little perceptible effect on the surrounding fluorescence and the grating regions are nearly imperceptible from the surrounding regions. Data values extracted from the images were used to calculate the observed enhancement in the 600nm grating and normalized against the background fluorescence of the ITO sample. The results indicate an enhancement of approximately 13.3 times for the gold sample compared to 5.3 times for chromium and only 1.3 times on ITO, with linear extrapolation used to evaluate enhancement values for gold due to the differing integration times. It is very important to point out that although the images presented in Figure 26 may not appear to show a massive distinction between the three materials, the image taken for a gold substrate represents only 80% of the integration time required to image the other two substrates. The difference in integration time was mandated by the inability of the CCD camera to image both sets of samples using identical imaging conditions. This was a result of intensity saturation for images of the gold sample, coupled with the inability to clearly distinguish images of the control samples using shorter integration. The results from the composite film also illustrate that there is a clear periodicity dependence in the fluorescence enhancement behavior, as well as dark regions where material has been completely removed, which can be observed as dark triangular

regions in the figures above. These results provide good evidence that observed enhancements can be attributed to interaction with surface plasmons rather than simple enhancement from the gratings alone. While fabrication and characterization of samples coated in composite material was successful, several issues with the mixture motivated investigation of further techniques for quantum dot deposition. The volumetric distribution of fluorescent materials is not desirable for studying the mechanics of grating coupled surface plasmon enhanced fluorescence. The nature of the deposition method causes the quantum dots within the composite to be distributed throughout the film thickness, and thus make it unsuitable for detailed examination. Furthermore, the solubility properties of quantum dots suspended within the solution led them to aggregate because of a low solubility of quantum dots in the resist solvent anisole, resulting in spotty emission from the film layer. This type of behavior has been observed previously in the literature and a solution to this problem has been presented by Pang, et al. in [27]. In order to alleviate this problem, samples were fabricated using direct introduction of quantum dots by spincasting from solution. Samples were first coated with gold or chromium followed by spincoating of PMMA. After this, quantum dots were introduced by spincasting onto the sample prior to electron beam exposure, followed by pattern definition and removal of excess resist in developer. Deposited quantum dots were expected to remain on the surface because of their insolubility in the developer solution. For the remainder of this study these samples will be referred to as prespun QD samples. Images from the resulting samples are shown in Figure 27 along with the image for the composite film on gold from Figure 26. Examination of the results shows a stark contrast between the

performance of composite material and direct distribution methods. Direct application of quantum dots onto the sample results in significant reduction of background fluorescence and increased uniformity in observed emission as evinced by the smoother appearance of the image in Figure 27b compared to Figure 27a.

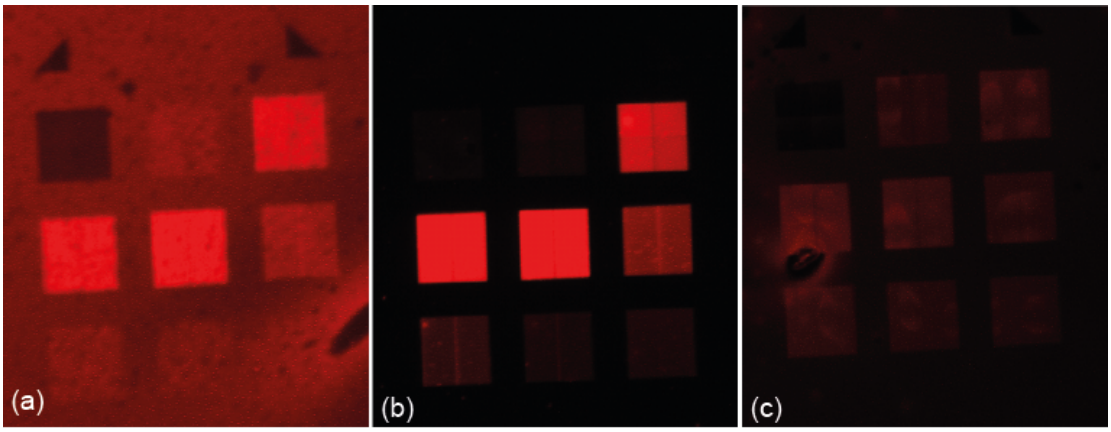

Figure 27 Comparison of different quantum dot deposition methods. All images captured using camera gain setting of 16. (a) PMMA/QD Composite on Gold, Integration time: 240s. (b) Prespun QD on Gold, Integration time: 30s. (c) Prespun QD on Cr, Integration time: 30s.

In addition to the improvements in sample quality, the observed fluorescence from the sample is greatly increased and can be seen from the difference in integration time required for successful imaging. The composite sample requires eight times the integration time at the same gain setting in order to measure an image intensity value slightly less than the prespun sample. While a clear distinction in behavior occurs for the gold substrates, observation of the chromium-coated substrates demonstrates behavior similar to previous samples with only a weak distinction between gratings and flat film regions, along with much lower intensity when compared to gold. The variation between different grating periodicities is also much weaker than for chromium than the distinct variations in fluorescence intensity visible for gold.

Measurements of fluorescence enhancement required correction for camera gain and integration time and avoidance of camera saturation, which resulted in an estimated enhancement of 94 times for the center grating on gold when compared to background from the same image. Similar measurement of the image in Figure 27c produced an enhancement factor of approximately 4 for the chromium-coated sample when measured against sample background.

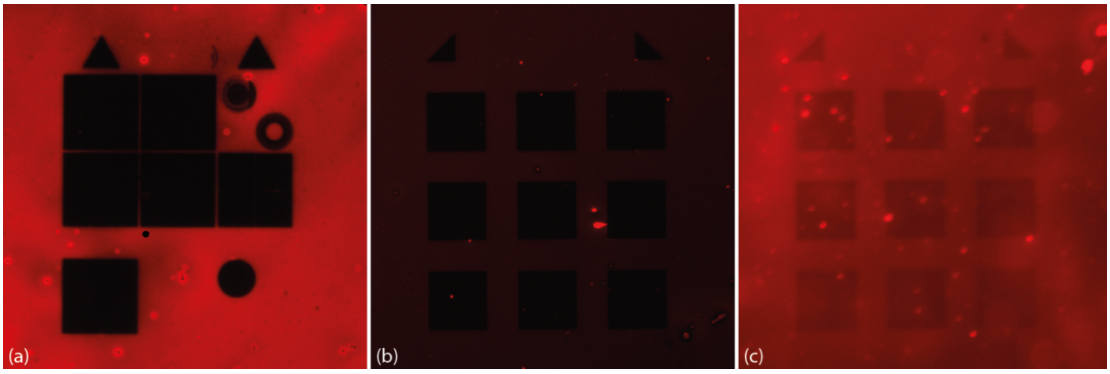

Figure 28 Fluorescence images of quantum dots deposited onto substrates after patterning of surface structures. All samples have been spun with 10^{-3} M QD solution in toluene as in previous samples. (a) Prespun QD on gold film at 16x gain and 15s integration. (b) Prespun QD on chromium film at 16x gain and 120s integration. (c) Prespun QD on ITO film at 16x gain and 240s integration.

The deposition of quantum dots onto substrates which have already been patterned with surface structures was also evaluated to explore the viability of such a process. Fluorescence images of the resulting postspun samples are shown in Figure 28. These images clearly demonstrate that for quantum dots deposited in this fashion, fluorescence within the patterned regions is suppressed even though a high concentration coating is clearly visible in the surrounding film regions. In order to investigate this phenomenon SEM imaging of the samples was performed in order to determine the spatial distribution of the deposited quantum dots.

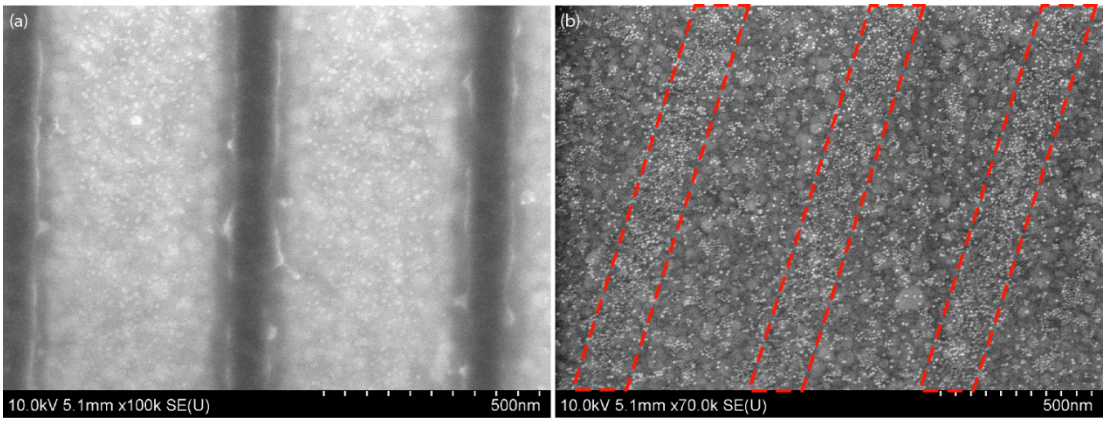

Figure 29 SEM images of (a) prespun and (b) postspun quantum dot samples on gold film substrates. The images illustrate a distinct contrast in the behavior of the two samples in both quantum dot distribution and electron contrast between resist and metal layers. Evenly spaced lines of quantum dots are visible in image (b) (denoted by red dotted lines) and correlate roughly to the intended 500nm grating periodicity.

The images show that the behavior of prespun and postspun samples is very different, with respect to both the properties of the resist and quantum dot distribution within the patterned area. PMMA stripes are clearly visible in images of the prespun sample while they become electron transparent on the postspun substrate. The distribution of quantum dots is also different with strips of clustered quantum dots visible in the image of the postspun sample mostly likely corresponding to the positions of the resist ridges based on the aspect ratio observed on the other sample. For both samples it is clear that quantum dots are distributed within the target region. This is especially interesting for postspun samples due to their lack of observed fluorescence in these areas. Based on this data it is currently unclear what causes the postspun quantum dots to exhibit quenching of their fluorescent emission. Possible explanations include modification of the resist surface during pattern definition which may cause formation of pores which could allow the particles to come into close proximity with the gold film. Alternatively the fabrication process could alter the surface properties,

changing the behavior of quantum dots located at the surface. Explanations regarding this behavior currently fall into the realm of speculation, and having found a successful means of nanoparticle dispersal further discussion of these effects is deferred for later study.

5.4 Quantum Dot Saturation

In order to ensure the validity of the experimental results examinations were made to check for saturation of the quantum dots as well as coupling of light across the metal film layers. Since further investigations of the fluorescence behavior are made based on the observed intensity of the fluorescence signal from various regions on the sample it is important to determine that the exciting source is not causing saturation of the quantum dot layer. In order to determine that there is no saturation samples were observed using the INM300 with neutral density filters inserted into the exciting beam path to attenuate the drive signal for comparison. ND filters with OD of 0.3 and 0.6 were introduced into the beam with individually and in combination to produce transmission of 12.5%, 25%, 50%, and 100% for comparison. Images of the sample through these filters were then compared to determine if the response observed exhibited saturation effects when exposed to the filtered mercury lamp excitation. Camera settings were selected to ensure that images of the sample without ND filters inserted were not saturated by the imaging process so that any observed saturation would be due to saturation of the fluorescent material itself. The resulting images and representative measurements are shown in Figure 30. A set of data points illustrating the behavior observed from these images is presented in Figure 30e.

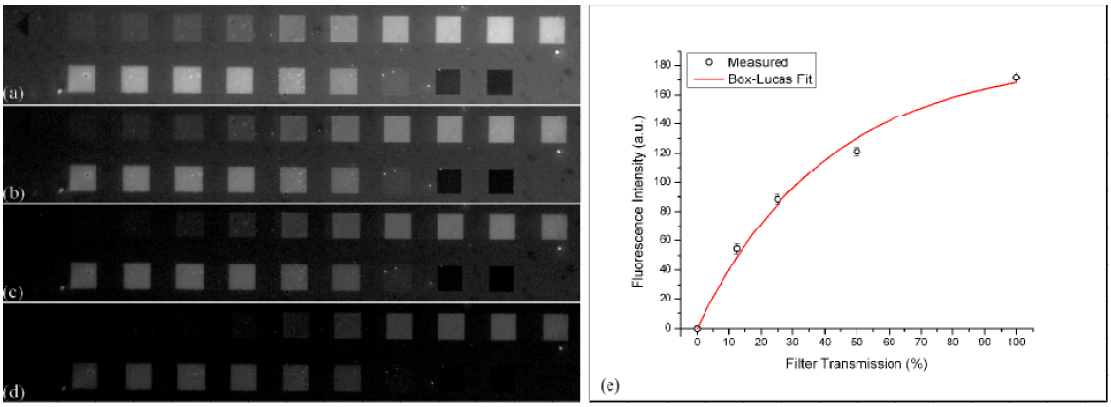

Figure 30 Fluorescence images of QD coated gratings with periodicity of 550nm and varying duty cycle taken with and without neutral density filter attenuation. All images are taken with camera gain of 2 and 20s integration time. (a) No filters inserted. (b) OD 0.3 filter inserted for 50% transmission. (c) OD 0.6 filter inserted for 25% transmission. (d) OD 0.3 and 0.6 filters inserted for 12.5% transmission. (e) Single set of measurements extracted from image align with numerical fit using Box-Lucas expression for saturation behavior.

The measured values demonstrate that the emission from quantum dots on the substrate experiences saturation as the source power is increased to its maximum. This behavior is consistent across measurements taken from each of the gratings visible in Figure 30(a)-(d) indicating that saturation is occurring in a consistent fashion throughout the sample. Additionally, the same behavior is observed when considering a sample where the periodicity of the gratings is varied. Fitting of the data using the Box-Lucas model for saturation effects and the corresponding curve is shown in red with the expression.

$$y(x) = A\left(1 - e^{-bx}\right) \qquad [5.4.1]$$

Based on these results saturation of the sample occurs based on the amount of source power that the sample is exposed to. However, the behavior of emission for at a given power is consistent across the sample and valid comparisons can be made provided that the source power is held at a constant value.

5.5 Metal Film Thickness

Selection of the appropriate metal thickness is important to prevent coupling of light to the back of the sample where it will not interact with the quantum dots and may be lost by scattering from the back side of the metal film. At optical frequencies away from the plasma frequency the skin depth in a metal can be described by using the Drude model for the dielectric constant. In this case the electrons are considered as free and damping is negligible as the oscillation frequency is much greater than the damping rate. Under these conditions the penetration depth for the transverse electric field into the metal is roughly constant until it approaches the plasma frequency where the metal begins acting as a dielectric and increased transmission begins to occur [95]. In this regime the value of the skin depth is related to the plasma frequency as:

$$\delta = \frac{c}{\omega_p} \qquad [5.5.1]$$

For the case of gold a plasma frequency of 9eV results in a skin depth of approximately 22nm. The thicknesses of the gold and chromium layers used in this experiment were selected by considering the optimal thickness for prism coupling of light into surface plasmons in order to retain the flexibility to excite from either the top or bottom of the samples. Since the measurements which were pursued in the study exclusively use topside illumination it was important to determine whether the thickness of the metal films has an effect on the observed fluorescence. If the gold film were to be insufficiently thick it would result in loss of light through to the backside of the sample and produce a lower signal than could be otherwise observed.

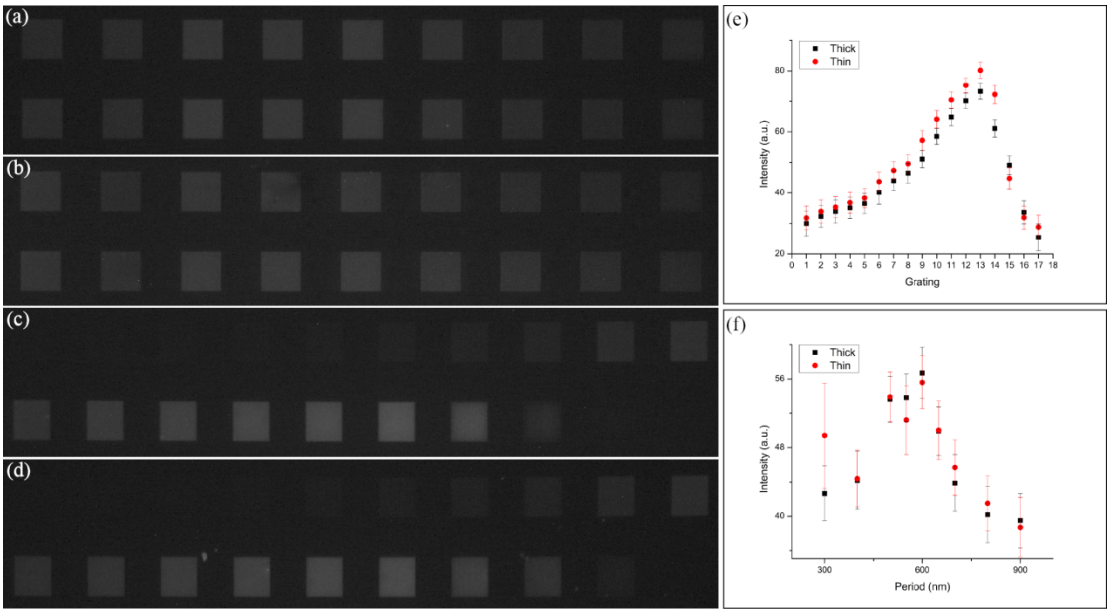

Figure 31 Fluorescence images of samples with 50nm and 100nm thick gold film as the substrate. Images of 550nm gratings with varying duty cycle on thick (a) and thin (b) metal layers as well as gratings of varying periodicity, (c) and (d) respectively, are shown. The images along with data points extracted from the images show that some variation in intensity is evident but that the overall behavior of the samples is unchanged. All images were obtained using camera gain of 2 and 25s integration.

In order to determine whether or not this effect was present in the experimental measurements samples with gold layer thicknesses of 50 and 100nm were fabricated in parallel and subsequently imaged under identical conditions using the INM300. The resulting images are shown in Figure 31 along with measurements extracted from the images for the different thicknesses of gold. Visual examination of the images gives little evidence of significant variation between the two samples. This observation is supported by the extracted values which appear consistent across both samples within experimental error. Indeed the sample with 100nm thick gold deposited even appears to produce a slightly lower fluorescence signal for the measurements in Figure 31e which is in direct contradiction to what would be expected in the case of leakage through the thinner films. Based on these results a

50nm thick gold film is sufficient to prevent significant loss of signal by coupling to the backside of the film.

5.6 Spatial Dependence of Emission

Having determined a suitable process for sample fabrication we now turn to investigating the behavior of QD emission from such systems. Observations from the experimental samples indicated that three distinct types of region could be discerned from the fluorescence images. These regions consisted of areas that were not patterned and contain unmodified resist which remained coated with QDs, regions where electron beam exposure was used to completely remove all resist and form a void, and regions where gratings had been fabricated and modification of fluorescence was observed. These three regions correspond to the background film, the small triangular alignment marks visible above the grating regions, and the grating regions themselves in the previous images. Characterization of these regions was of great importance to determine the origin of the fluorescence observed in the grating regions. Emission from fluorescent particles is modified by proximity to metallic surfaces. The regions within the patterned areas contained a mixture of film coated regions separated by areas consisting essentially of exposed metal upon which the particles would hypothetically be resting. It was therefore expected that most of the observed fluorescence should originate from QDs whose position was some distance from the metal film surface, preferably at the surface of the PMMA film. To make a distinction between these conditions, the behavior of QDs in and around the triangular alignment marks was characterized. The lack of emission apparent in the fluorescence images was taken to indicate either a lack of QDs in the region where

gold had been exposed by the lithography process, or the presence of quenching effects which would prevent emission of any QDs that were present. Scanning electron microscope and atomic force measurements were taken of both the triangular regions and the gratings themselves to determine how QDs remained distributed in regions where the resist layer was removed by the lithographic process. The resulting images are shown in Figure 32 and confirmed that QDs deposited using the prespun dispersal method remain everywhere on the sample after completion of pattern definition. QDs that remain in areas where the resist film has been removed settle onto the surface of the metal and experience quenching of their fluorescence as expected [60,84,85,86]. AFM imagery of the sample indicated that the QDs remain at the surface of the film and are not absorbed into the resist layer as might be anticipated for fluorescent molecules in similar circumstances.

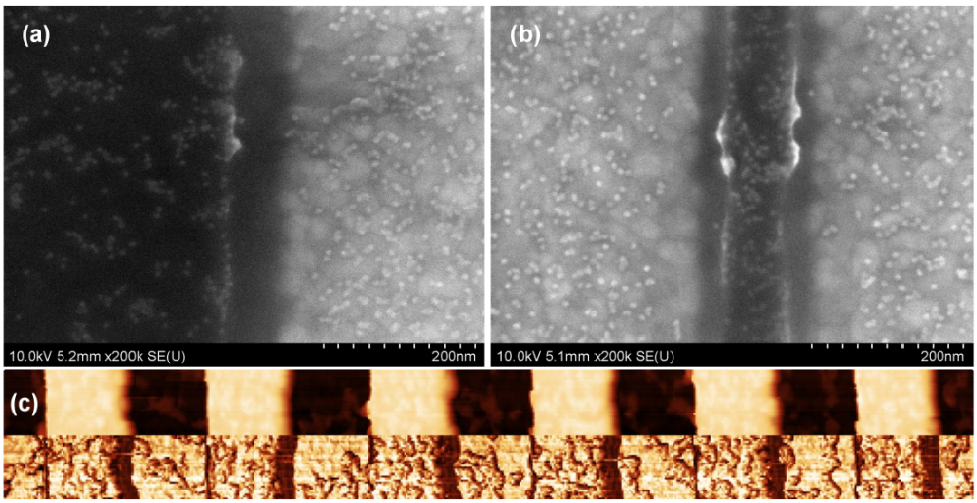

Figure 32 (a) SEM image of the boundary between film and gold regions at the edge of an alignment mark. Note the QDs visible on both sides of the boundary as small white dots. (b) SEM image of a narrow grating line. Once again the QDs are visible throughout the grating region both above PMMA and on the gold surface. (c) AFM amplitude and phase images of a grating similar to (b) illustrating presence of QDs at the surface of the film and gold. QDs on the film surface do not absorb into the dielectric material that forms the grating and remain on the film interface.

From this we can conclude that the fluorescent emission observed in the samples is attributed primarily to QDs that remain at the surface of the PMMA layer and that QDs in close proximity to the metal film no longer contribute to the measured fluorescence signal.

5.7 Variation of Grating Parameters

5.7.1 Periodicity

Having determined how the behavior of quantum dots deposited onto the sample surface relates to the position of the quantum dots relative to the fabricated surface structures we can now examine how the parameters of the grating affect quantum dot fluorescence. The most obvious parameter to begin with which would be of interest here is the effect of grating periodicity. Observation of the periodicity dependence of the enhancement effect is important in optimizing fluorescence signals. Since standard fluorescence microscopes are used for observation of the samples, illumination is performed in a direction normal to the sample surface with light incident from a cone of angles corresponding to the properties of the focusing objective used to couple in the excitation beam. For this portion of the study, both the MZFLIII and INM300 fluorescence microscopes were used to observe the same pattern. The resulting images were analyzed using Gwyddion AFM analysis software in order to extract line scans of enhancement versus grating periodicity, shown in Figure 33. Enhancement of fluorescence peaked for gratings near the wavelength of excitation and diminished gradually as the grating periodicity shifted away from a central value. Although the data indicated that peak enhancements occurred at distinct grating periodicities the effect was found to be broadband in nature with

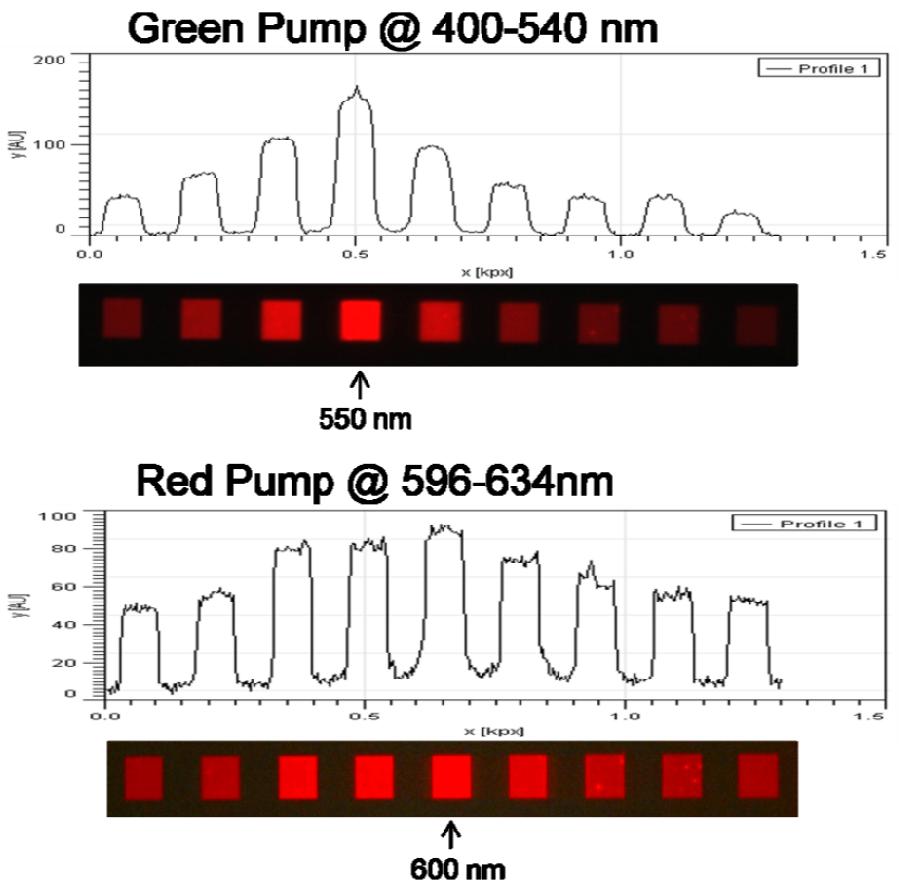

Figure 33 Fluorescence images of a series of gratings fabricated on a gold substrate. (Top) Image and line scan of pattern taken by MZFLII FOM with green exciter. (Bottom) Image and line scan of pattern taken by INM300 FOM with red exciter. Maximum enhancement is observed for gratings with periodicity close to the wavelength of excitation. Broadening occurs due to broadband wavelength sources and angular variation from the microscope objectives. Grating periodicities in nm (left to right), 300, 400, 500, 550, 600, 650, 700, 800, and 900.

gratings to either side of the peak periodicity exhibiting noticeable enhancements, which were lower than the central peak. It was also observed that high enhancement was obtained over a broad range of periodicities when using the INM300 compared to a more clearly defined peak enhancement obtained on the MZFLIII. We attribute these effects to the nature of the sources and optical coupling arrangements in the two microscopes. The broadband nature of the sources and filters used with the

fluorescence microscopes contributes to broadening of the range of periodicities that may provide coupling to SPPs. In addition to this, the focusing optics cause the exciting beam to arrive at the sample within a cone of angles dictated by the properties of the optical input path. In particular, the MZFLIII has a long working distance objective, which has a focal length of 60 mm and an illuminated region of roughly 10 mm diameter for the magnification used in the images. The INM300, on the other hand, uses objectives with sub-millimeter working distance and has a significantly smaller illumination region, on the order of 1 mm in diameter. As a result, the cone of incoming rays on the INM300 system encompasses a larger range of angles, which may allow for coupling via a larger selection of grating periodicities, and part of the more broadband enhancement shown in the lower image of Figure 33 can be attributed to this effect.

5.7.2 Duty Cycle and Height

Earlier measurements placing the participating fluorophores primarily at the surface of the resist film along with the propensity for QDs to remain on the film after processing enabled a more detailed study of the effect of grating parameters on the fluorescence enhancement effect to be performed. While grating periodicity plays an important role in determining the fluorescence enhancing properties of SPP-supporting gratings, the role that grating geometry plays has yet to be investigated. This study has explored the role of grating film thickness and duty cycle in order to ascertain how these parameters could be used in optimizing the grating-enhanced fluorescence signal.

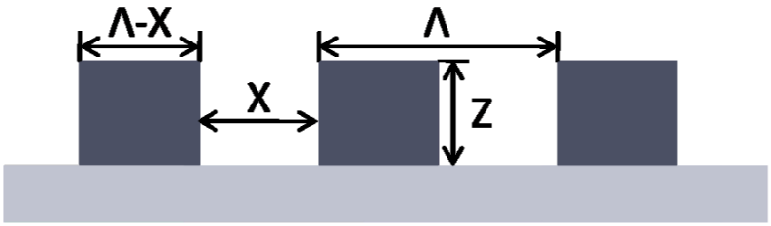

Figure 34 Illustration of the grating parameters of interest in the experiment. The grating period Λ has been shown to be important. The remaining parameters of interest are the grating film thickness Z and the duty cycle, which will be defined using X, the spacing between adjacent ridges.

Figure 34 illustrates the basic parameters of interest that were studied. For simplicity, the grating shape was standardized to a square wave geometry and process parameters were optimized to produce the desired spacing. Control of the film thickness was accomplished by adding a low power O_2 plasma etching step after deposition of the resist layer and before spin-on deposition of QDs on to the film. To reduce surface roughness and obtain low etch rates the plasma etching parameters were adjusted to use low power along with high pressure settings resulting in a slow abrasion of the film. After etching and deposition of QDs onto the resulting film surface, it was found that the adhesion of QDs was significantly increased by the introduction of the plasma treatment. This resulted in a significant increase in fluorescence background signal as will be apparent from subsequent figures and occurs due to oxygenation of the surface, which produces various compounds and renders the film increasingly hydrophilic [92]. Images of identical grating samples with and without O_2 plasma treatment are presented in Figure 35 demonstrating both the increase in background fluorescence and improvement in coating uniformity found after plasma treatment. Comparison of the two images shows that plasma treatment primarily affected the behavior of fluorescence on the background film but did not significantly impact the

intensity of fluorescence within the gratings. Since the increase in fluorescence is specific to regions with continuous PMMA films it is most likely a consequence of SPP excitation from plasma induced surface roughness without significant changes in QD density.

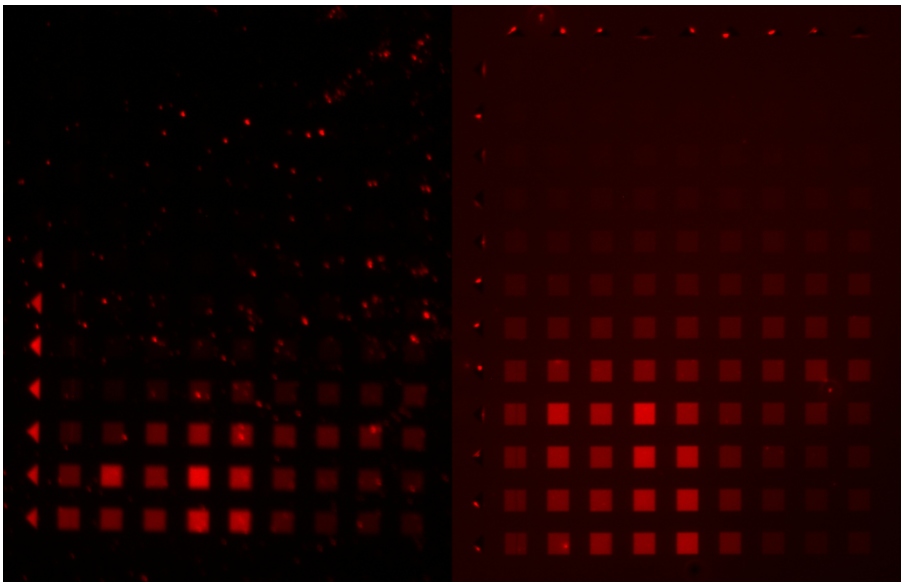

Figure 35 Fluorescence microscope images of grating patterns with (right) and without (left) O_2 plasma treatment prior to quantum dot deposition demonstrating the increased background fluorescence and improved coating uniformity obtained from plasma treatment.

A direct consequence of this was an apparent reduction in the observed fluorescence enhancement due to the increase in background signal relative to the grating regions, with the untreated sample exhibiting an enhancement of 41x compared to a lower enhancement of 5.2x on the treated sample. All of the enhancement measurements were taken using the fluorescence signal from the surrounding film as a reference due to variations in background fluorescence intensity relative to film thickness. This was done to evaluate the effect of the diffraction grating where SPP excitation occurs, compare it to the fluorescence of fluorophores placed upon a similarly treated dielectric spacer layer, and characterize the additional contribution when SPP

coupling was present. Samples were first fabricated using a fixed periodicity and thickness with variations in the width of the lithographically defined strips to evaluate the effect of grating duty cycle. It was anticipated that as the separation was increased the results should reflect a balance between the coupling capability of the grating and removal of the grating film, which reduces the amount of area contributing fluorescence. A grating periodicity of 550 nm was selected for maximum observed fluorescence on the MZFLIII FOM. However, equipment concerns mandated that the images be taken on the INM300 system, which is still capable of excitation and imaging for this grating periodicity. Fluorescence measurements of the sample showed that the fluorescence enhancement has a clear dependence on the duty cycle of the grating. AFM measurements were taken to determine the width of the grating ridges and confirm consistency in the film thickness of 133 nm. At either extreme, the fluorescence signal should approach a uniform resist film for low values of X and an exposed gold film for large values, which is confirmed by the experimental measurements. From the data we can see that there is an optimal point where the enhancement reaches a maximum value and subsequently tapers off to either side in a roughly linear fashion. The optimal design point for grating duty cycle was found to be roughly 50% but the number of measured data points prevents us from making a statement of the precise value. Nevertheless, this value correlates well with other measurements taken on prior samples fabricated during the development of the sample shown here. Finally, samples were prepared with a grating periodicity of 550 nm and duty cycle of 50% and the resist layer thickness was modulated using plasma etching as described earlier. Because of

variation in required electron beam dose for different resist thicknesses the samples contained a series of gratings with varying duty cycle and electron dose. Images of the sample were then taken using the INM300 along with AFM imagery of the structures in order to locate gratings with parameters satisfying the desired criteria.

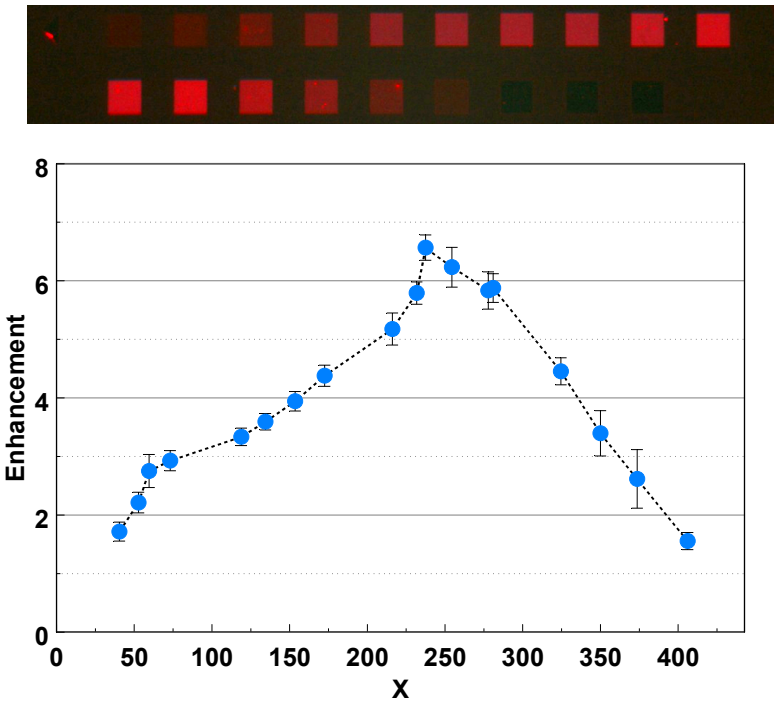

Figure 36 Measurements of sample where duty cycle X has been varied with grating height and periodicity fixed. (Top) Fluorescence image of sample taken on INM300 illustrating a clear dependence of fluorescence on the grating duty cycle. (Bottom) Measured enhancement factor for grating regions relative to surface background.

Observation of the samples illustrated a clear variation in background fluorescence from the resist film surrounding the grating regions. This was most likely due simply to proximity effects from the presence of the metal film as described elsewhere [60,84]. We are primarily interested here in the behavior of fluorescence within the grating regions and observations demonstrated that emission from the areas of interest varied strongly as a function of film thickness. This can be plainly observed from

Figure 37, where the grating regions are clearly recognizable for a film thickness of 128 nm and appear very similar to the samples shown in previous examples. For a film thickness of 51 nm, however, the grating regions do not appear distinct from the surface and exhibit emission that is approximately equal to or less than the surrounding film surface. The fluorescence in regions where QDs reside on the surface of unpatterned PMMA was found to vary with the thickness of the underlying resist layer. This type of variation is well-known and has been observed previously [60,84]. As a simple model, the behavior of the QDs here may be approximated as an excited dipole above a conducting surface. We represent the emission behavior of such a system as a quadrupole, which consists of the dipole and its image charges, and combine this with an exponentially decaying drive field to fit our observed background data. The corresponding fitting expression is given by:

$$y(x) = Ax^2 e^{-2Bz} + C \qquad [5.7.1]$$

The resulting curve is shown in Figure 37 and fits well with the fluorescence values observed experimentally. To separate the effect of the gratings from variations due to simple distance modulation effects enhancement values were calculated and normalized against the intensity from the local film surface. Extraction of the grating enhancement values indicated that the fluorescence enhancement effect exhibits a feature similar to a threshold thickness at approximately 75 nm below which the grating regions perform similar to the surrounding film. Above this thickness the enhancement increases in an exponential or super-exponential fashion and shows no sign of saturation for the measured thicknesses. The nature of these interesting phenomena is not fully understood at this time and further investigation would be

needed in order to gain a better understanding of the observed effects. Based on observations from Figure 35, it is possible that this effect occurs when the grating thickness is reduced to point where it stops providing stronger coupling when compared the surrounding surface roughness. Other possible explanations for this behavior are additional quenching effects and changes in guided modes supported within the PMMA layer. It is also important to note here that the precise nature of the enhancement is difficult to obtain as the film thickness increases. For increasingly thick films the interaction between the grating, SPPs on the surface and guided modes in the film are complex and complicate analysis of the results. Nevertheless, the results presented here are sufficient to provide a preliminary basis for application and further exploration of the fluorescence behavior of quantum dots exposed to surface plasmons that are excited using the grating coupled scheme.

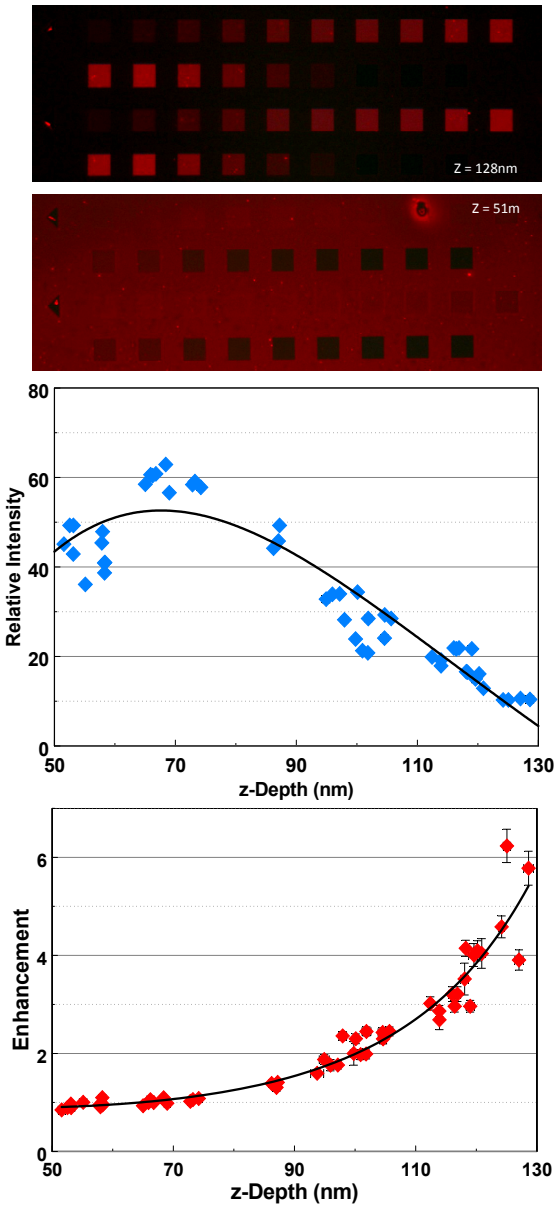

Figure 37 Measurements of grating sample where grating height Z has been varied with duty cycle and grating periodicity fixed at 550nm. (Top) Fluorescence images of samples taken on INM300 illustrating a clear dependence of fluorescence on the grating duty cycle at film thicknesses of 128 and 51 nm. Variation in background fluorescence is clearly visible. (Middle) Background fluorescence intensity from unpatterned resist layer fitted to a simple quadrupole model driven by exponentially decaying field. (Bottom) Measured enhancement factor for grating regions relative to surface background.

6 Fluorescence Lifetime

Investigation of how contributions from enhanced emission and absorption contribute to the fluorescence enhancement effect can help in developing a greater understanding of this behavior by providing further examinations of the underlying phenomena responsible for fluorescence enhancement observed in these experiments. Determining whether one of these processes is the dominant contributor to these enhancement effects is an important step, which will help indicate what types of changes can be expected for different emitters and sample constitutions. In order to obtain a simple discrimination between these two effects samples of gratings with varying periodicity were observed using a Nikon microscope equipped with an Imperx IPX-2M30 CCD camera and an appropriate filter to allow imaging of fluorescence at 640nm. Samples were placed onto a rotation stage and rotated azimuthally while directly illuminated by a DPSS laser operating at 532nm. Discrimination between enhanced emission and enhanced absorption can be obtained in this configuration by observing variations in the fluorescence intensity with respect to the orientation of the grating relative to incident excitation. Enhanced emission behavior should remain consistent regardless of grating rotation while enhanced absorption, which is influenced by the coupling of incident light by the gratings, will vary strongly based on grating orientation. Images of a QD coated grating with a 550nm period and 50% duty cycle are shown in Figure 38 and illustrate the type of behavior observed for gratings excited in this configuration.

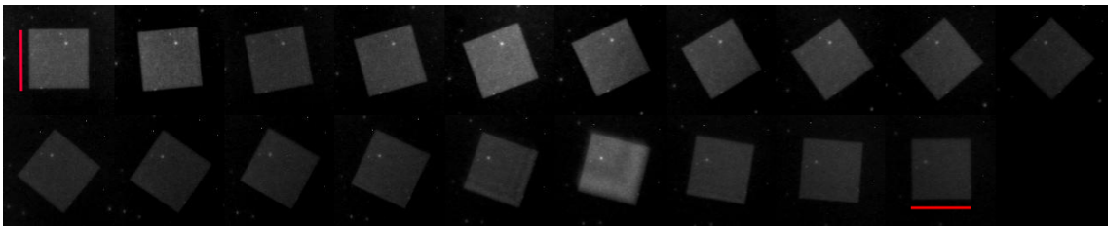

Figure 38 Fluorescence images of a QD coated grating with 550nm period and 50% duty cycle as it is rotated from 0 to 90 degrees in 5 degree increments (increasing from left to right, top to bottom). The images illustrate a clear dependence of fluorescence intensity on source orientation suggesting that enhanced absorption plays a significant role in the fluorescence enhancement behavior.

From the images it is clear that fluorescence from the grating regions is strongly dependent on the angle of incidence of the source, with peaks in fluorescence intensity occurring at clearly defined angles. The observation of such behavior provides initial evidence that enhanced absorption plays a significant role in the fluorescence enhancement phenomenon but does not rule out contributions from enhanced emission effects as the gratings are still clearly distinguishable from the background level at all angles. In order to determine whether the fluorescence enhancement behavior contains significant contributions from enhanced emission effects, measurements of the decay lifetime and emission spectra of emitters can be used to determine how the surface structures perturb their behavior. The presence of significant contributions from emission enhancement can be determined by searching for correlations between shifts in the lifetime and increases in fluorescence intensity, as well as modifications to the emission spectrum from resonant coupling between the surface structure and emitters. Observing the correlation between these factors and the observed fluorescence intensity will enable a determination of the extent to which these processes are expected to influence the behavior of deposited quantum dots.

6.1 FDTD Simulation

Prior to presenting the experimental lifetime measurements, FDTD simulations have been used to provide an idea of what type of behavior can be expected for emitters coupled to surface structures with an ideal pattern geometry. The magnitude of modifications to the fluorescence lifetime is obtained by evaluating the power emitted by a dipole placed near the structure as described in Section 4.1. It is expected that the results of the simulation will, most likely, not accurately describe the observed behavior since the technique is only able to consider a single dipole source located at a fixed location relative to the surface geometry, and with a clearly defined orientation. In reality, the samples under consideration contain a random distribution of dipole orientations and geographical positions which can significantly alter the behavior of measured quantities. In spite of these limitations, the development of these simulation results can be of use in determining what kind of impact the position and orientation of the dipole has on its lifetime. It will also provide an illustration of how the physical parameters of the grating influence the decay dynamics of the emitters. The effectiveness of these simulations in emulating the response of dipoles in close proximity to surfaces is demonstrated in Figure 39. The plotted field intensities accurately represent the behavior of a dipole in free space (a) and over a dielectric half-space (b). From (c) – (f) we can see clearly that the addition of a grating significantly modifies the response and depends on the specific dipole position. The simulations also illustrate the lack of surface plasmons propagating on Cr compared to Au as described previously.

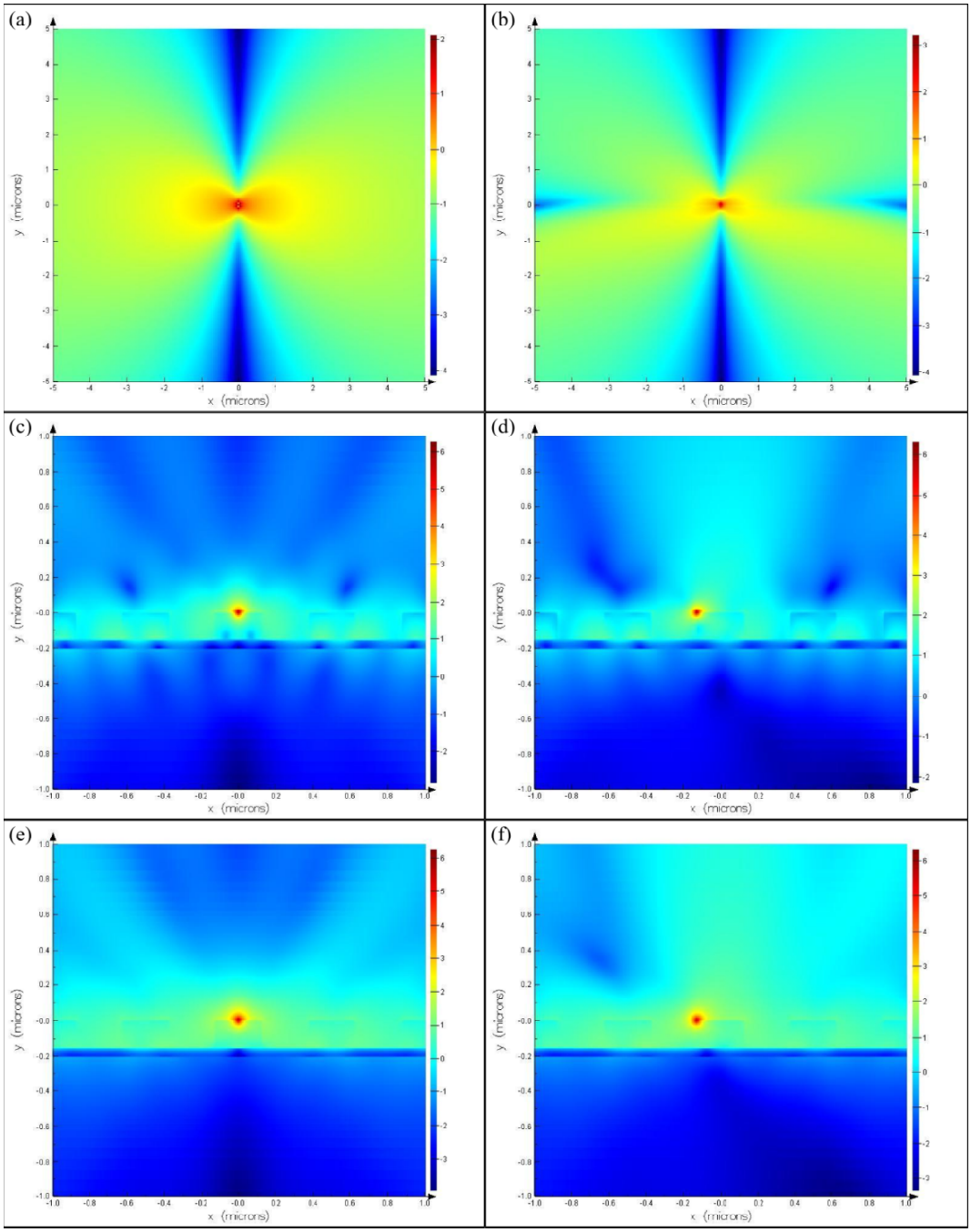

Figure 39 Electric field intensity for dipoles over various interfaces plotted on log scale. (a) dipole in free space; (b) dipole over half-space of index 1.1; dipole over center (c) and edge (d) of 550nm grating ridge on Au film; (e) and (f) same grating on Cr

In order to observe the influence of physical parameters on the fluorescence lifetime a series of simulations were performed with the dipole placed above the center of the grating ridge. For each set of simulations the orientation of the dipole was fixed to be perpendicular to the grating surface, in-plane along the grating ridge, or in-plane across the grating ridge to observe distinctions caused by the orientation of the dipole. The material configuration for the simulations was a substrate of index 1 or 1.5 with a 50nm layer of gold onto which rectangular dielectric regions with an index of 1.5 are placed to represent the grating structure. In all simulations the background index is taken to be air and fixed at 1. The emission wavelength of the dipole is set at 641nm to correspond to the quantum dots used in the experiment with the dielectric constant of gold taken from [14]. In order to represent a single dipole placed within the structure rather than a series of coherent sources a finite number of ridges is considered and PML are used at the boundaries of the simulation region to attenuate any fields which leave the region of interest. Before examining the behavior of emitters over a grating, a series of simulations were performed emulating a dipole centered above a single ridge with varying width and a height of 155nm. These simulations provide an illustration of how response to the periodic modulation of the grating differs from a single structure and underscore the significance of using a grating rather than individual uncoupled ridges. The results of these simulations are presented in Figure 40 and show that the lifetime exhibits an oscillatory behavior as the width of the ridge expands away from the dipole location. This behavior can be understood as interactions between the emitter and fields which are reflected from the sides of the ridge.

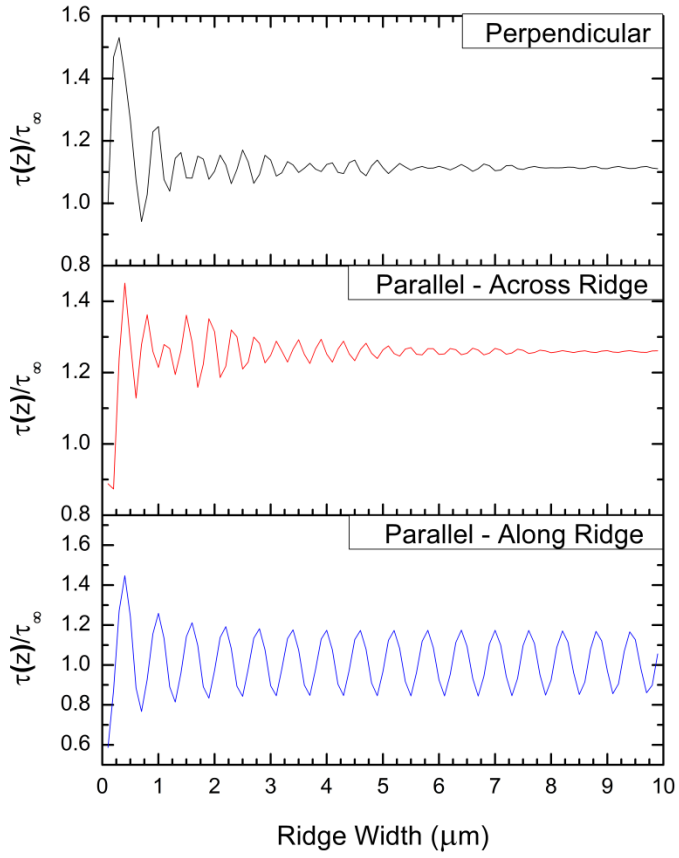

Figure 40 Fluorescence lifetime modification for a dipole centered above a single square dielectric ridge with varying width with a 50nm gold layer underneath and a glass substrate. All values are normalized to a dipole in free space.

For large widths the lifetime modification clearly depends on the dipole orientation and can be associated with each orientation coupling differently to the underlying metal layer and substrate. It is clear from these simulations that the orientation of the dipole has a significant impact on how the fluorescence lifetime behaves. Further simulations were then performed where the parameters of a grating were varied to observe their influence on emitter lifetime. As a first test, simulations of gratings with a varying number of grating ridges were performed in order obtain convergence of the simulation results. A 50% duty cycle grating with 550 nm periodicity was

simulated and the calculated lifetime modification plotted as a function of grating cycles. PML boundary conditions were used at the sides of the simulation region and offset from the sides of the grating in order to avoid coupling of reflections back into the structure. The resulting curves are plotted in Figure 41 and show that the change in fluorescence lifetime should converge for all orientations if over 20 cycles are included.

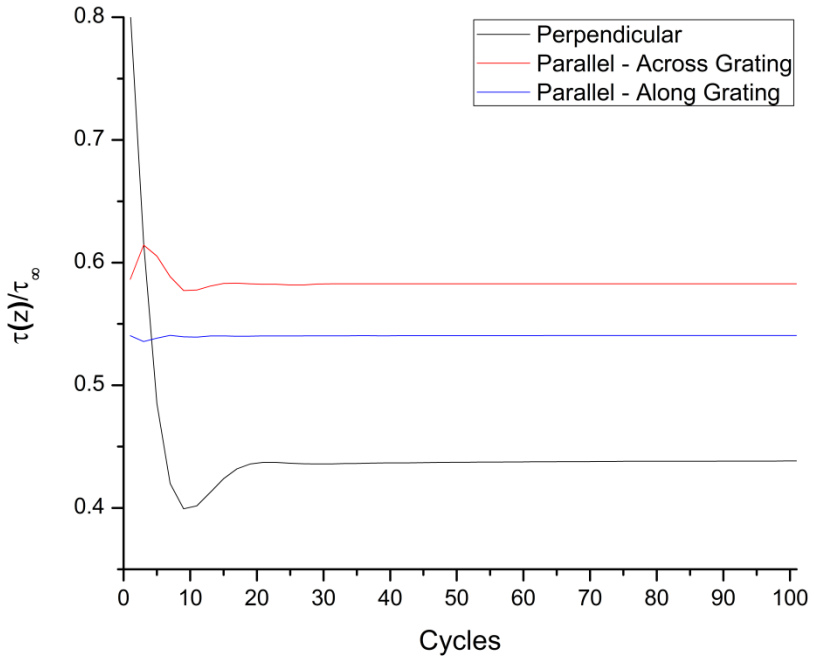

Figure 41 Lifetime modification of fluorescent emitters centered above a 550nm periodicity grating on a 50nm gold film and glass substrate. Convergence in the results is obtained for gratings which include more than 20 cycles of the grating within the simulation region. All values are normalized to a dipole in free space.

Based on this finding subsequent simulations were performed using a grating containing 21 cycles to ensure accuracy in the simulation results. For the first series of simulations the behavior of the fluorescence lifetime with respect to vertical separation between the dipole and grating was examined. In these simulations a

grating pitch of 1 micron was selected in order to demonstrate how surface corrugations perturb the dipole away from the coupling point around 500-600nm. Results were obtained with and without the presence of a glass substrate to see how the addition of glass underneath the metal film affected the simulation.

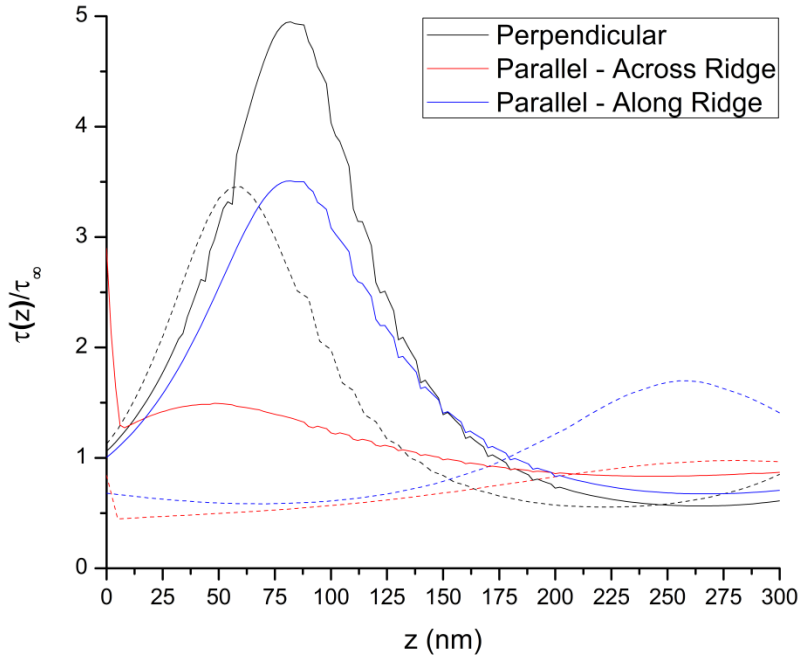

Figure 42 Modification of dipole lifetime as a function of the dipole-grating separation z for three orthogonal orientations on a 1 micron grating for a dipole situated above the center of the ridge. Results for a structure with (solid) and without (dashed) the glass substrate are shown. All values are normalized to a dipole in free space.

It is clear from the simulation results that emitters placed in close proximity to this type of dielectric grating on a metal film exhibit behavior which is very different from a planar metal interface which was described previously in Figure 23. This is expected since the grating structure provides a richer distribution of photonic modes for the emitter to interact with. The clear difference between the behavior for a system with and without the glass substrate was not anticipated and suggests the

possibility that the gold layer could be thin enough to support modes which are coupled between the upper and lower interfaces. This result is in contrast with the experimental measurements which indicated little variation between different thicknesses of gold. In practice, the excitation of these coupled modes may be inhibited by surface roughness.

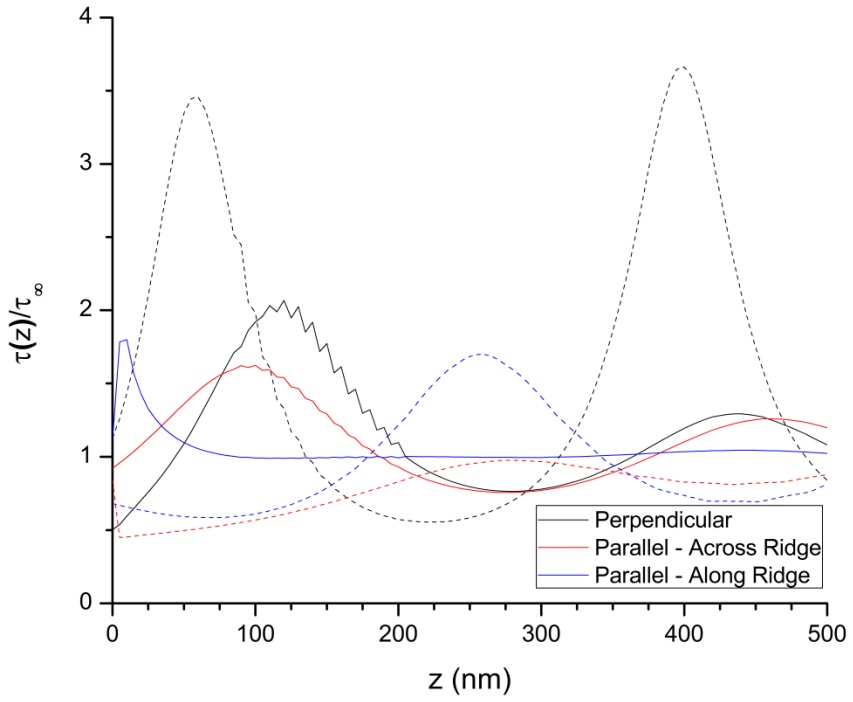

Figure 43 Modification of dipole lifetime as a function of the dipole-surface separation z for three orthogonal orientations with the dipole placed above the edge (solid) and center (dashed) of the grating ridge. All values are normalized to a dipole in free space.

An additional set of simulations was performed with the dipole above the center and edge of the grating ridge without the glass substrate underneath to provide an idea of how the lateral placement of the dipole affects these results. Data from this simulation is shown in Figure 43 and demonstrates that for these two most extreme cases the behavior of the dipole is significantly altered depending on its positioning

across the grating ridge. Having established that dipole orientation, position, and substrate material can all impact its lifetime, a series of simulations emulating the parameter sweeps in the experiment were performed. The dipole placement was fixed above the center of the grating ridge to facilitate comparison. The results of these simulations are shown in Figure 44 - 46 and show that the lifetime behavior depends strongly on the dipole orientation as well as the physical parameters of the grating geometry. However, this effect is mitigated if an isotropic combination of different dipole orientation responses is considered rather than the individual orientations. A response of this type would be relevant if the orientation of the emitter were to rotate and sample different directions before decaying such as in the results presented in [60] or for a distribution of randomly oriented emitters scattered along the center of the ridge. The result of applying such a condition to the simulation results is illustrated by a dotted black line in the figures. These curves show that the strong variations in fluorescence lifetime observed for clearly defined emitter orientations is significantly reduced for an ensemble of randomly oriented sources. As a result, it would appear that in order to observe strong couplings between dipoles and dielectric surface gratings some measure of control would need to be exercised over the dipole orientation. The results presented thus far have served to investigate the behavior of an emitter placed at either the center or edge of the grating ridge. Unlike this simplified situation the samples used in the experiment are randomly distributed and oriented across the surface of the grating which makes them unlikely to conform to such a simplified model.

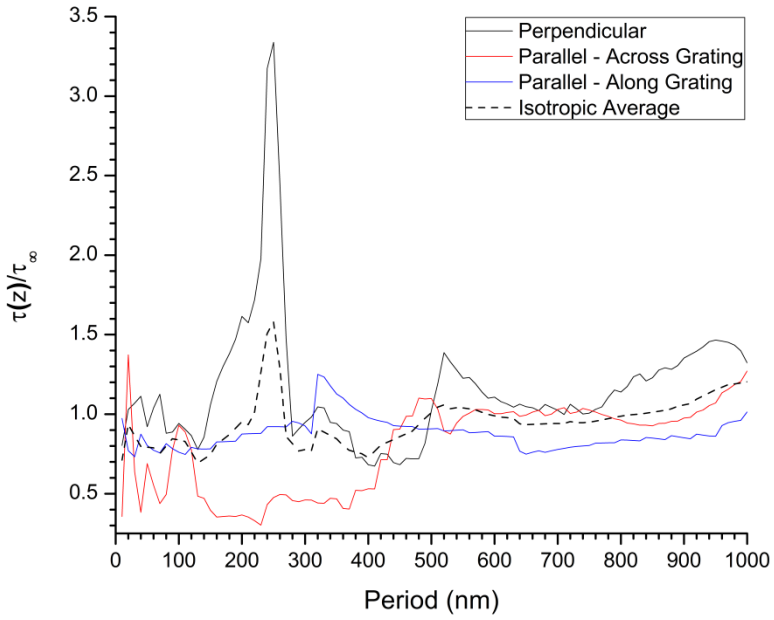

Figure 44 Lifetime modification of fluorescent emitters centered above a 50% duty cycle square dielectric grating as a function of grating periodicity. All values are normalized to a dipole in free space.

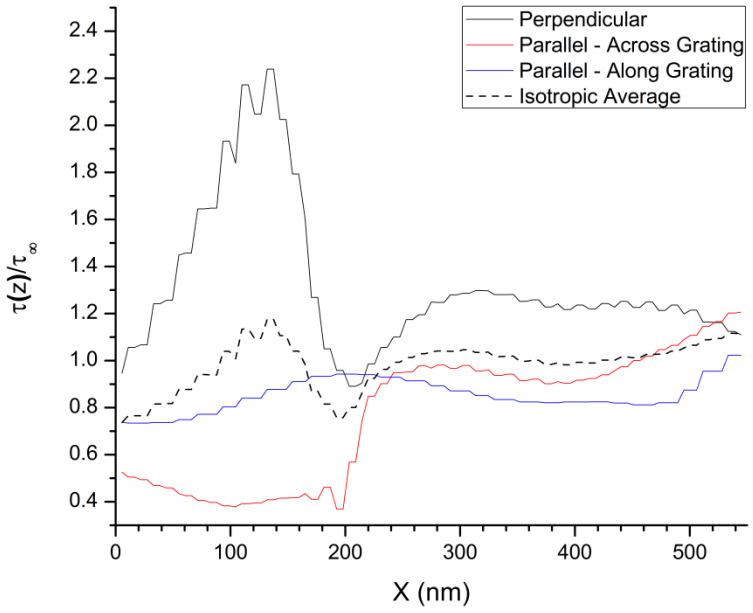

Figure 45 Lifetime modification of fluorescent emitters centered above a 550nm square dielectric grating as a function of grating gap width. All values are normalized to a dipole in free space.

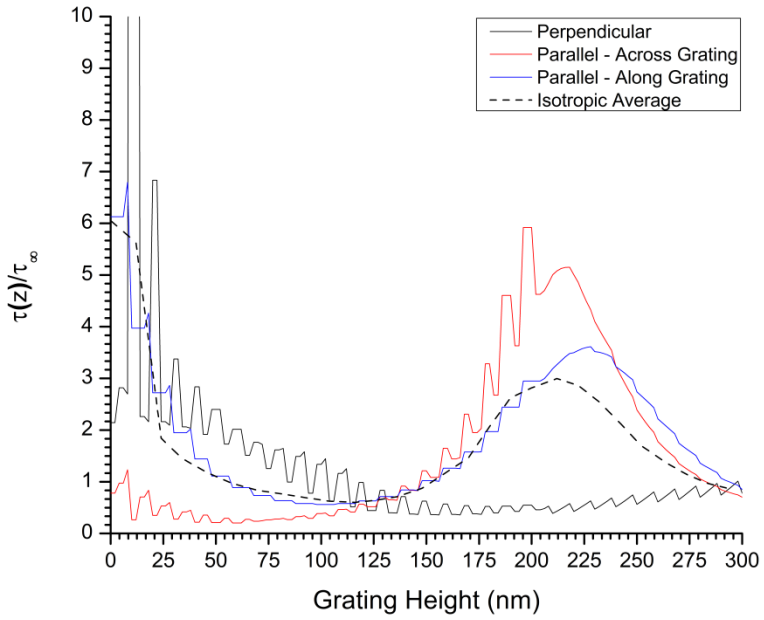

Figure 46 Lifetime modification of fluorescent emitters centered above a 550nm square dielectric grating as a function of grating height. All values are normalized to a dipole in free space.

In order to expand the simulations to better represent the experimental conditions, the effect that the lateral dipole position has on the lifetime behavior is an additional parameter to be considered. Unfortunately, performing a complete series of simulations to simultaneously represent this parameter along with variations in the grating structure would be both time consuming and difficult to visualize. Instead, a series of simulations using a fixed 50% duty cycle for the gratings were used to examine the effect of the lateral grating position for the periodicities used in the experiment presented in Section 5.7. An example of the results from these simulations is shown in Figure 47 for a grating with periodicity of 550nm and a 50% duty cycle.

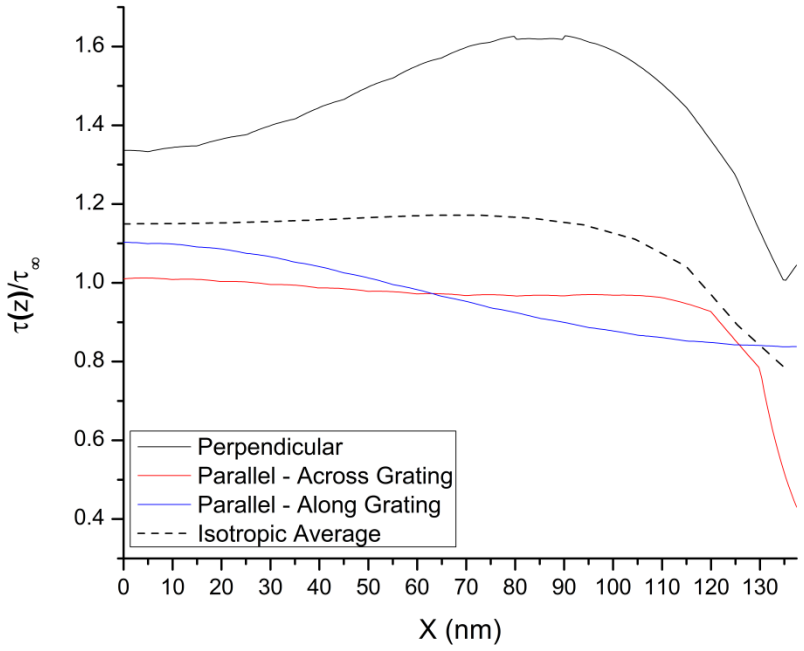

Figure 47 Lifetime modification of fluorescent emitters centered above a 550nm square dielectric grating with 50% duty cycle as a function lateral dipole separation from the center of the grating ridge. All values are normalized to a dipole in free space.

It is clear that depending on the dipole orientation the lateral placement of the emitter across the ridge can either significantly perturb its lifetime or have little effect as seen above for a dipole oriented parallel to the plane of the grating and across the ridge. Once again an isotropic combination of the different orientations has been calculated and represented on the graph as a dotted black line. We can see from the figure that similar to the previous simulations an isotropic combination of the results reduces the variations in the emitter lifetime once again. Finally, in order to obtain a reasonable estimate for the lifetime behavior of a dipole on the experimental samples the average lifetime is taken across the ridge in the lateral direction for each polarization and then the three resulting values are averaged with each other to account for the random

orientation and location of the individual sources. The results, which are shown in Figure 48, show that the overall lifetime modification as a function of periodicity which is measured from the experimental samples may not vary as significantly as one would presume from the previous simulations. Observation of the drastic variations predicted by the earlier simulations would require control of both dipole orientation and placement on the surface.

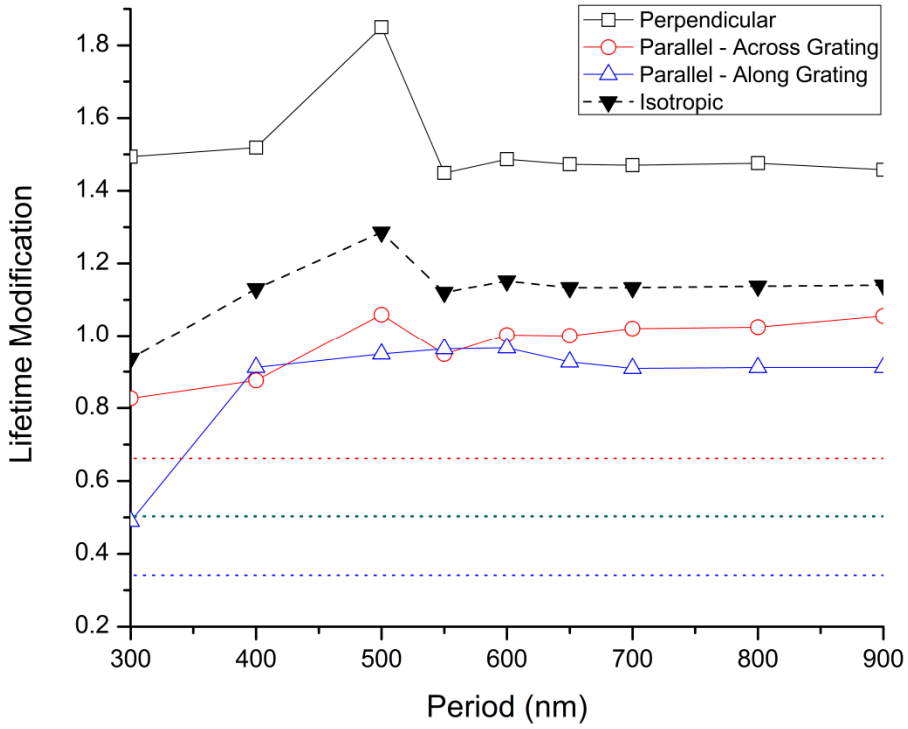

Figure 48 Average lifetime modification for a fluorescent emitter placed above gratings of varying periodicity. The isotropic combination of the lifetime modification for the three dipole orientations is given by the black dashed line. Values for dipoles on uniform PMMA film are indicated by the dotted lines. All values are normalized to a dipole in free space.

6.2 Time Correlated Photon Measurements

6.2.1 Measurement System and Fitting Procedure

Measurements of the fluorescence lifetime for quantum dots deposited on the grating structures presented in Chapter 5 were made using a time correlated single photon counting (TCSPC) system. In this technique, the sample is exposed to short pulses from the exciting source which are synchronized to single photon counting hardware which registers the temporal location of detected photons relative to the pulse timing. Ideally, the pulse repetition rate is selected such that the spacing between pulses is much longer than one lifetime allowing the system to fully relax between cycles.

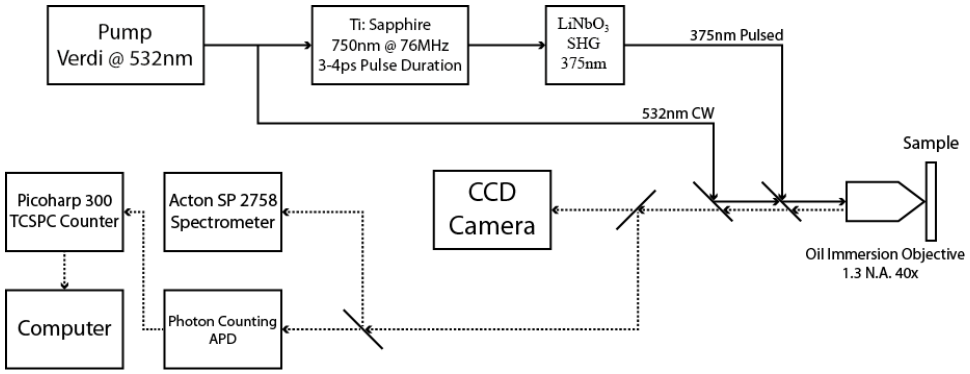

Figure 49 Schematic of the time correlated single photon counting system used in these measurements.

The TCSPC system used here to determine fluorescence lifetime belongs to the Nanophotonics and Quantum Information Research Group here at University of Maryland and we thank Professor Edo Waks for allowing us access to make these measurements. Excitation in this system is provided by frequency doubling of 750nm pulses from a mode locked Ti:Sapphire laser running at 76MHz resulting in a pulse train of 3-4ps pulses at 375nm. In addition to this signal the pump signal which is provided by a CW Verdi system at 532nm is available for spectral measurements and identification of fluorescence on the sample. These outputs are delivered to the

sample through an oil immersion objective with 1.3 NA and the resulting fluorescence signal is sent back through a dichroic element to the detection stage. A small amount of the return signal is split off into a CCD camera to allow focusing of the objective onto the sample surface and the remainder is passed to either an Acton 2758 Spectrometer or a single photon counting APD. In order to generate the decay curves the signal from the APD is connected to a Picoharp 300 TCSPC counter unit which is then connected to a computer to display the results. It is important to note here that the excitation used for TCSPC measurements is at 375nm rather than the 532nm excitation used in previous experiments. While excitation of surface plasmons is possible at this wavelength the quality of such surface modes is poor due to high absorption and it is highly likely that most plasmon coupling in these measurements should come from coupling between excited QDs and the metal interface. Measurements of the dark count from the system demonstrate that the background level from the detection stage was insignificant with a range of less than 50 counts for a 400 second measurement. Due to the high repetition rate of the source used in this system successive pulses arrive before the emitters are able to full relax. As a consequence, the sources are not able to fully return to their base level and the observed signal consists of multiple pulses arriving consecutively within the observation window. In order to extract both the time constants and corresponding contribution amplitudes from these curves the individual pulse responses were time shifted by integer pulse periods and overlapped to produce a single decay curve which was then used to perform the fitting. Since each pulse response represents an identical emission probability distribution the use of such a measure is possible

without perturbing the results from the fitting. Due to the overlapping decay curves it is not possible to obtain the values of interest directly from a simple biexponential fit. In order to remedy this problem it is necessary to consider the response from an infinite series of exponential decay curves with the same time constant repeating at intervals of T and beginning at time t → -∞. Each of these pulses can be described by the form

$$f_i(t) = Ae^{-(t+iT)/\tau} \qquad [6.2.1]$$

with the curve at t = 0 equal to

$$f_o(t) = Ae^{-t/\tau} \qquad [6.2.2]$$

The total signal observed in the interval $0 \le t < T$ consists of the signal produced by the pulse plus the effects of all preceding pulses. The overall signal observed within the time interval is

$$F(t) = Ae^{-t/\tau} + \sum_{i=1}^{\infty} Ae^{-(t+iT)/\tau} = Ae^{-t/\tau}\left(1 + \sum_{i=1}^{\infty} e^{-iT/\tau}\right) = \frac{Ae^{-t/\tau}}{1-e^{-T/\tau}} \qquad [6.2.3]$$

It is clear that the decay time constant remains unperturbed by the presence of the additional pulses. The effect of pulse overlap is an increase in the amplitude which varies with the pulse repetition interval. For cases where a level of background counts is present this should be determined independently and the resulting decay response fitted to:

$$F(t) = A'e^{-t/\tau} + B \qquad [6.2.4]$$

The constant B should be fixed at the measured background value. For the case of quantum dots the use of a single decay time constant was insufficient to provide a

good fit to the measured data and so a biexponential fit was applied as previously described in Section 3.1.

6.2.2 Lifetimes on Bare Glass

Before moving on to measurements of experimental samples the lifetime behavior of samples exposed to 1μW and 15μW were compared to ensure that power levels were sufficiently low to prevent the onset of Auger recombination effects in the sample. Fitting to the resulting curves resulted in an extracted lifetime of 2.40s and 2.32ns for the short lifetime component and 13.30ns and 12.36ns for the long lifetime. Errors in the fitting parameters are roughly 0.06-0.07ns for the short lifetime component and 0.25-0.4ns for the longer component.

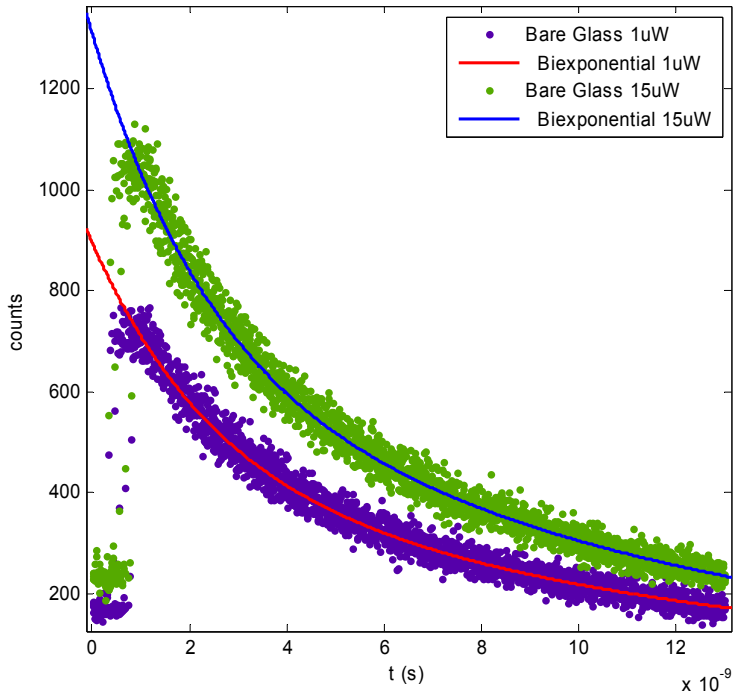

Figure 50 Fluorescence decay curves for quantum dots on bare glass exposed to 1μW and 15μW incident power at 375nm along with biexponential fits to the resulting data.

Visual examination of the curves on a linear scale and log scale give no indication of the rapid initial descent commonly associated with Auger recombination [96] in quantum dots is occurring at the higher power. Based on this result subsequent measurements were made using 1 μW of power without concern of Auger recombination in the samples.

6.2.3 Variation On SiO_2 Layers

Prior to measuring the behavior of quantum dots on and around the grating structures a series of samples were fabricated with various thicknesses of SiO_2 deposited onto a 50nm gold layer and thin glass cover slip substrate. The purpose of these samples was to provide confirmation that the behavior of quantum dot lifetimes in such a system is similar to that previously described for fluorescent dyes. Unlike the grating samples, introduction of quantum dots onto these substrates was performed by dropcasting of dots in solution onto the sample rather than spincasting due to lack of adhesion. The resulting inhomogeneity in quantum dot dispersion prevents meaningful examination of the amplitude coefficients but lifetime behavior should remain the same provided that regions of strong aggregation are avoided. The results, shown in Figure 51, show a behavior similar to that depicted in Figure 21 and 23 and confirm that these nanoparticles exhibit behavior similar to the simulations and comparable fluorescent dyes. These measurements allow further studies of quantum dots on PMMA films to be correlated directly to the simulation results.

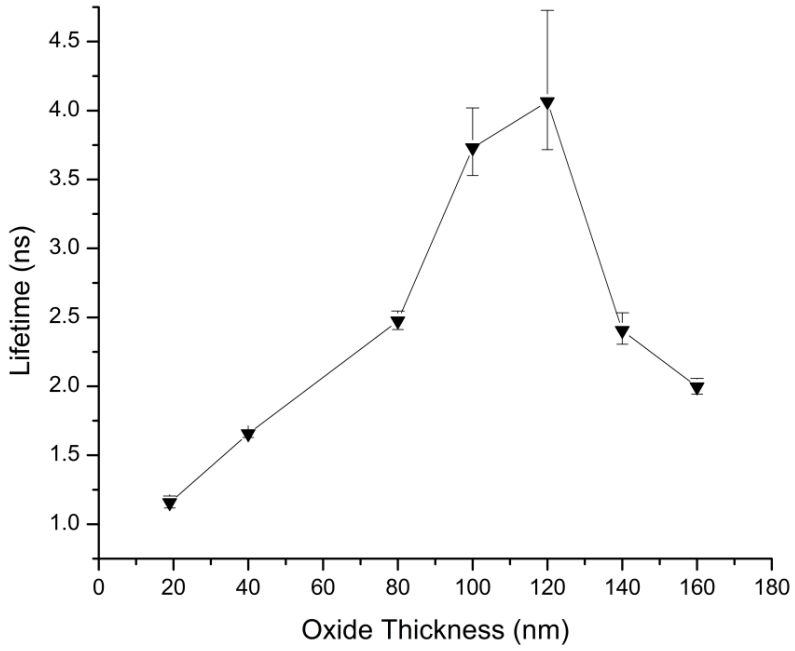

Figure 51 Fluorescence lifetime variations of quantum dots on varying thicknesses of SiO_2 deposited onto gold coated glass slides

6.2.4 Quantum Dots on Dielectric Gratings over Gold Films

6.2.4.1 Fluorescence Lifetime Measurements

Lifetime measurements of grating patterned substrates identical to those presented in Chapter 5 were performed in order to examine the effect that the presence of the gratings had on emitter behavior. When examining the samples for enhanced emission effects, the presence or lack of correlation between lifetime shifts and emission intensity is of primary interest. Additionally, spectral measurements of the sample can be used to search for spectrally resolved coupling between quantum dots and the underlying structures. If strong coupling is present in a resonant system wavelength selective coupling results in the appearance of localized peaks within the emission spectrum [97]. To begin the analysis, a series of lifetime measurements

were taken using gratings of different periodicity and duty cycle with the same spacing as those in Chapter 5. The series of decay curves were fitted and the resulting lifetime components plotted along with the contribution amplitudes for each component. The results of these observations demonstrate clearly that the short lifetime contribution is the dominant factor in emission from these quantum dots as expected since it is correlated to emission from the "Bright" singlet exciton state discussed earlier. It is also apparent that the behavior of the component amplitudes is consistent for both lifetimes and the values vary in the same fashion as the grating parameters are modulated. This can be interpreted as an indication of absorption enhancement since both components are driven by the same structure independent absorption profile. It is unclear at this time how the value of the longer lifetime, which is associated with QD surface interactions, should rely on grating modulation and further discussion of those results will be deferred for further study. Measurements of the fluorescence lifetime on gratings of varying periodicity are plotted in Figure 52 and show that the experimental measurements deviate from the simulated behavior for results measured at a periodicity of 300nm, exhibiting a higher lifetime than the curves predict. For values above 300nm both simulations and experiment exhibit a peak in the fluorescence lifetime at 500nm followed by a reduction and flattening of the lifetime. Correspondence between the experiment and simulation can be determined by dividing the measured lifetimes by the predicted lifetime modifications.

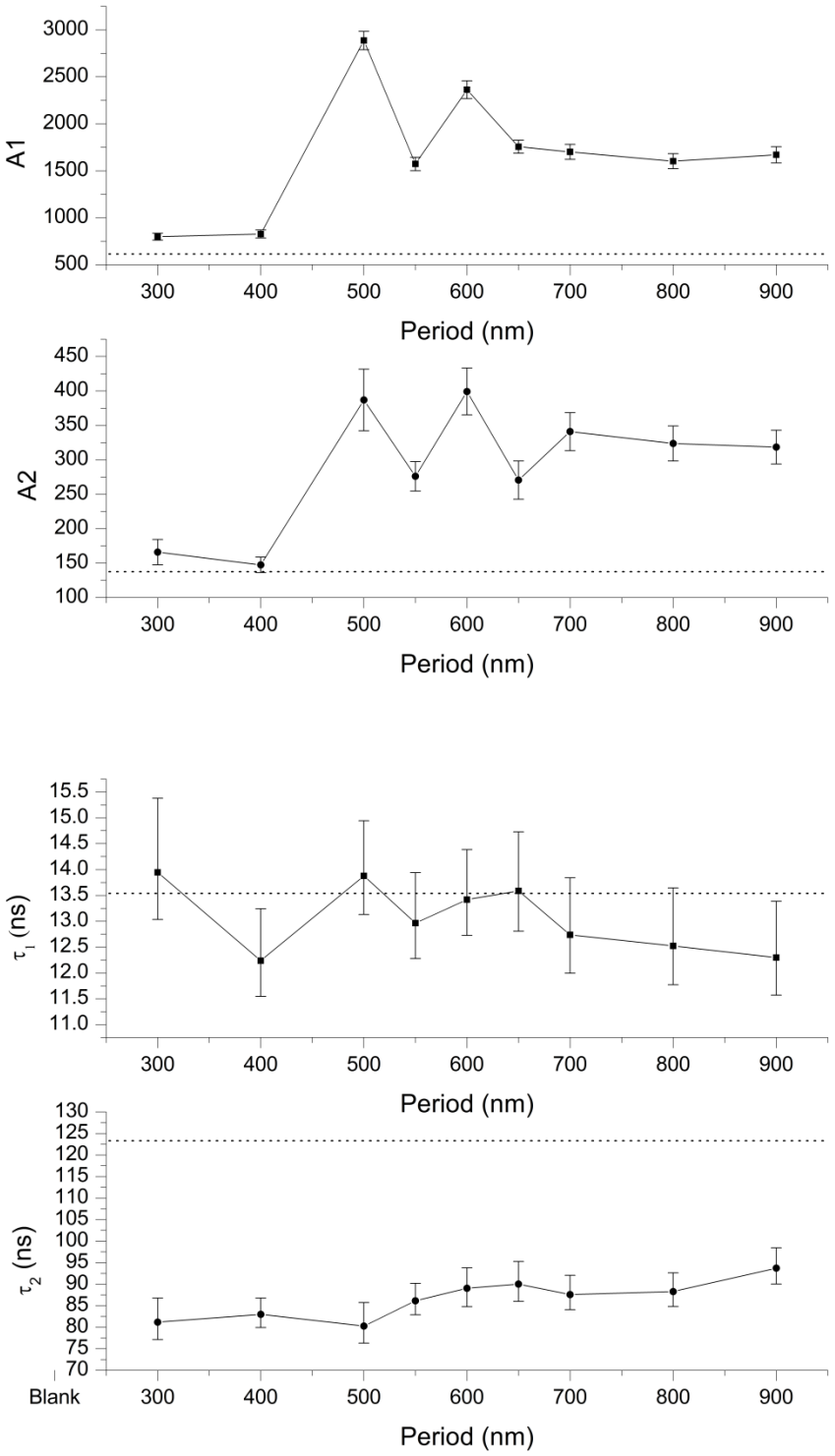

Figure 52 Lifetime component amplitude (top) and lifetime variation (bottom) for quantum dots above gratings of varying periodicity. Values for quantum dots on uniform PMMA film are denoted by the dotted lines.

In order for the simulation to accurately describe emitter response this should produce a constant lifetime for the unperturbed source. A plot of this result in Figure 53 shows that if error in the fitting coefficients is considered the values produce a nearly constant value. This suggests positive agreement between the simulated and observed behavior.

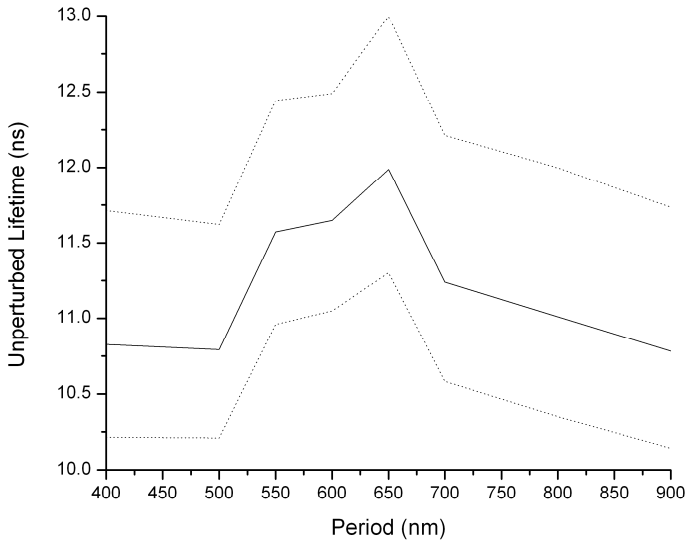

Figure 53 Values for the unperturbed fluorescence lifetime calculated by division of the measured values by the expected lifetime modification predicted by the simulation results. Upper and lower bounds are shown evaluated by considering the error in the fitted coefficients from the least squares fit.

Values obtained for quantum dots with varying duty cycle exhibit a lifetime variation which appears to oscillate as the gap width increases in approximately 150nm intervals. Such behavior is not unexpected and is likely an extension of oscillations observed in previous simulations for a single ridge of varying width. Once again, the component amplitudes vary together reinforcing support for the significant contributions from enhanced absorption effects.

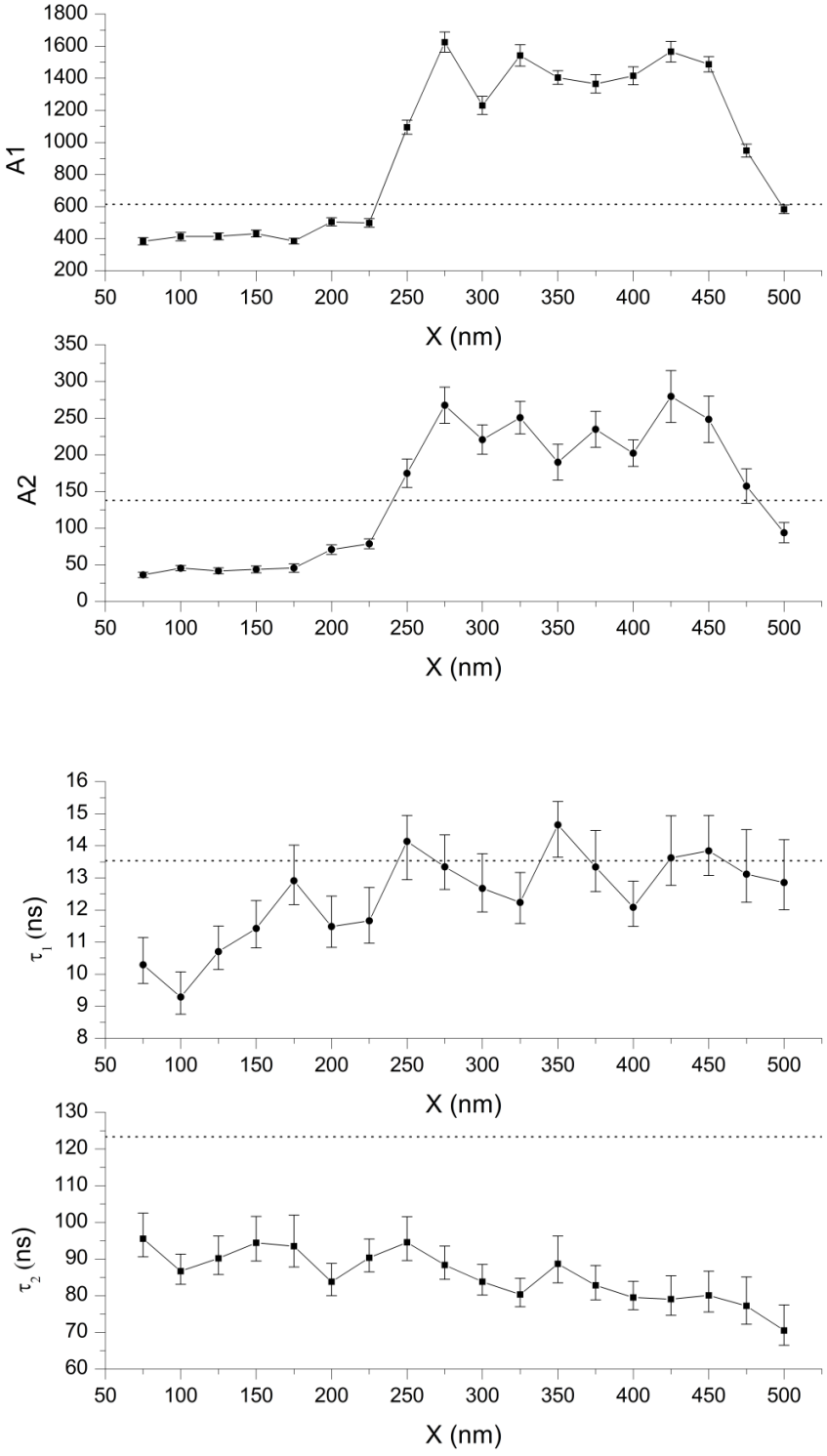

Figure 54 Lifetime component amplitude (top) and lifetime variation (bottom) for quantum dots above gratings of gap width. Values for quantum dots on uniform PMMA film are denoted by the dotted lines.

As the system is operating at a wavelength with a low probability of surface plasmon excitation, the increase in fluorescence intensity should be attributed to field enhancements from the surface grating. This conclusion is further supported by the lack of correlation between variations in lifetime and the measured fluorescence intensity. If significant emission enhancement was present changes in the lifetime should couple directly with increases in fluorescence signal. Consideration of the lifetimes and corresponding component amplitudes does not appear to illustrate a correlation between variations in lifetime and changes in amplitude. If long and short lifetime values for both measurements are considered simultaneously, no consistent variation in the lifetime can be coupled with the amplitudes to explain the increase in fluorescence intensity. Based on these results there is no evidence that emission enhancement plays a significant role in this fluorescence enhancement behavior. The enhancement mechanism in these structures can then be attributed primarily to enhanced absorption originating from plasmon excitation and the grating fields.

6.2.4.2 Emission Spectra

As a final verification of these conclusions spectral measurements of quantum dot emission were obtained using the spectrometer coupled to the TCSPC system. For these measurements the 532nm CW pump signal was used to excite the samples instead of the pulsed source which allowed for surface plasmon excitation as well as coupling between the emitters and interface. The integration time of the spectrometer was fixed at 10s with a spectral range from 600-700nm for quantitative comparison.

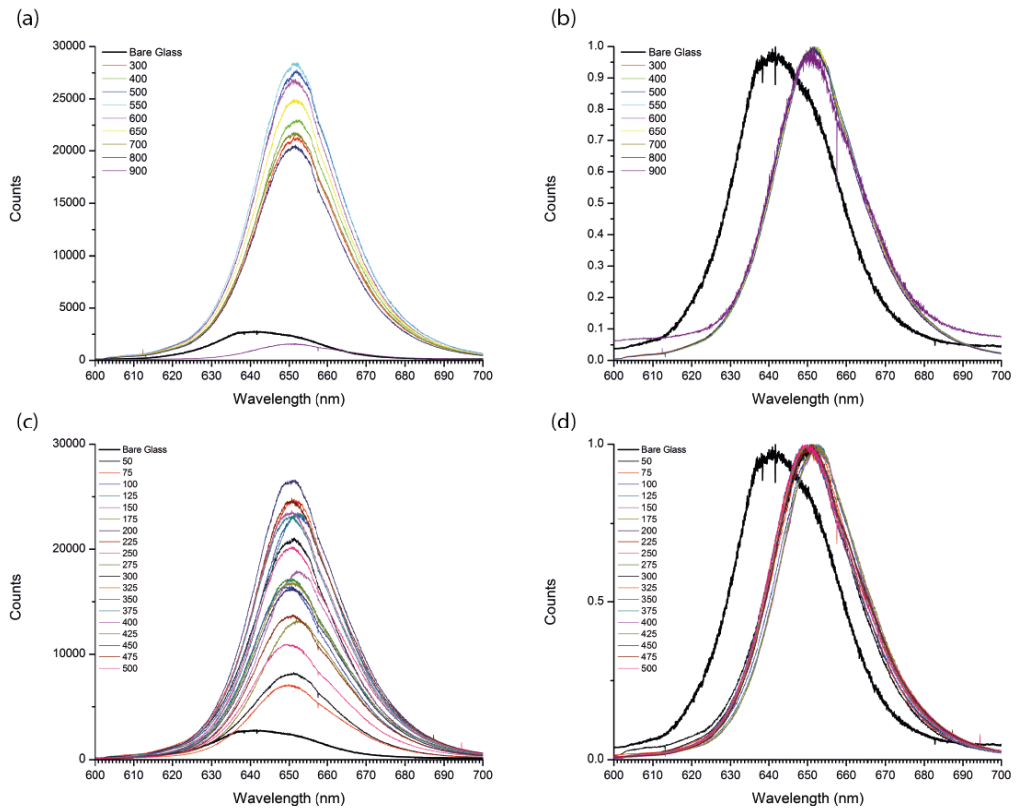

Figure 55 Emission spectrum of quantum dots deposited onto PMMA gratings over gold and excited using 532nm CW illumination. Raw spectra with varying grating periodicity (a) and duty cycle (c) are shown along with normalized versions (b) and (d).

Spectra obtained in these measurements are shown in Figure 55 for both raw data and peak normalized values. It is clear from the raw curves that the gratings have a significant impact on the amplitude of the signal collected by the system. In particular, it appears that a sizeable increase in fluorescence is obtained regardless of the grating periodicity present on the surface for gratings with a 50% duty cycle. Observations for 550nm gratings of varying duty cycle show that the duty cycle has a more significant impact on the fluorescence for a given periodicity. This supports the results from previous images and is most likely simply a manifestation of the transition from a flat dielectric into a grating and then to completely bare gold region.

Perhaps the most interesting feature of the spectral measurements is the presence of a clearly defined spectral shift from a peak value of 641nm, which is the manufacturer's specified wavelength, to approximately 651nm which was not apparent from the previous measurement methodology. Such peak shifting is known to occur for cases where off-peak emission is enhanced while emission near the normal peak is simultaneously quenched leading to an apparent shift in the overall emission spectrum. An example is presented in [97] where surface enhanced fluorescence from localized surface plasmon supporting metallic nanostructures has been shown to produce significantly modified spectral emission from fluorescent dyes. Interestingly the amplitude of the spectral peak shift does not appear to be strongly dependent on either the grating period or duty cycle with the exception of some smaller shifting with duty cycle which is not understood at this time. This behavior suggests that the shift is related solely to the presence of a metal-dielectric layer rather than the gratings themselves. The lack of localized peaks or additional features in the spectral curves besides shifting of the spectral peak indicates that the QDs are not experiencing coupling to any sharply defined resonant interactions of quantum dots to the gratings. In order to further examine the spectral behavior of the quantum dots additional analysis of the measured spectra was performed in order to extract the peak enhancement as well as the spectral peak position and peak width. Values extracted from the data for gratings of varying periodicity are shown in Figure 56. Unfortunately, data extracted from observations pertaining to enhancement with duty cycle variation produced inconsistent results and further examination is needed to verify the observed behavior.

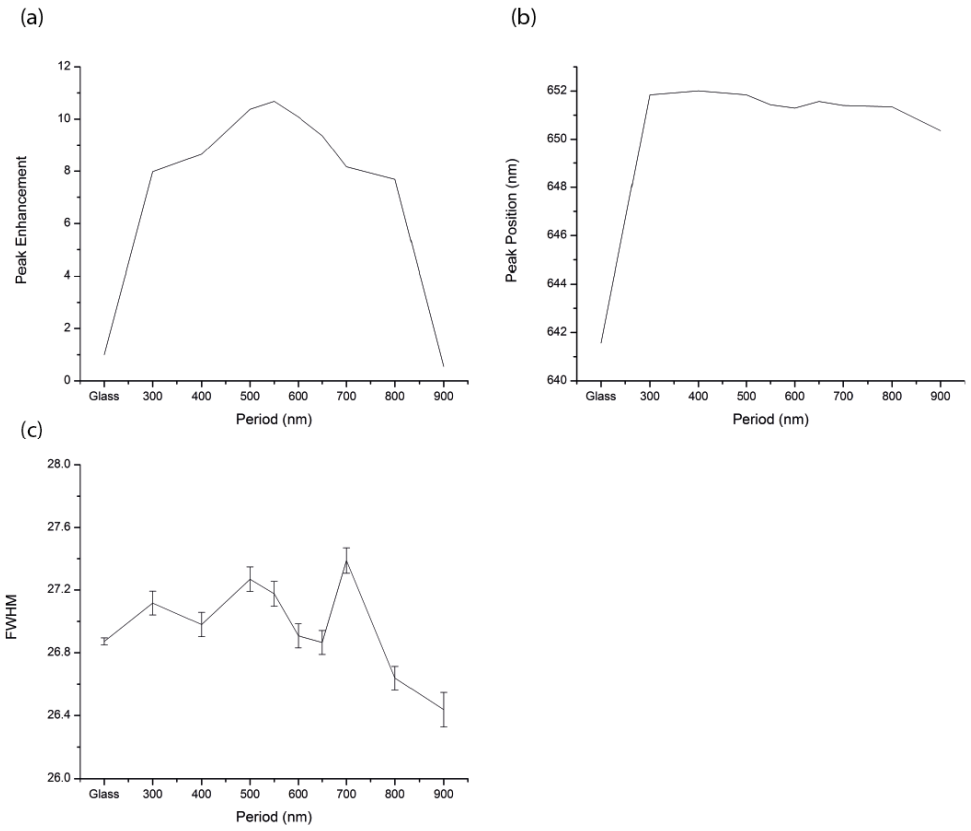

Figure 56 (a) Enhancement of spectral peak intensity for gratings relative to QDs on bare glass. (b) Peak position as a function of grating periodicity. (c) FWHM of spectral peaks as a function of grating periodicity.

Graphical examination of the peak enhancement shown in Figure 56a shows that values extracted from the spectra agree well with FOM measurements performed earlier and demonstrates a peak enhancement of 10.68 at a grating periodicity of 550nm. Interestingly, the enhancement for many gratings further from the peak remains significant. It is possible that this effect is related to the high NA of the microscope objective which can broaden the coupling range similar to comparisons between the MZFLIII and INM300. This is supported by the wide enhancement peak around 550nm however further observations would be required to fully determine the effect and are deferred for later investigation. The extracted peak position is plotted

in Figure 56b and shows that the peak exhibits an initial shift when going from glass to the grating but remains essentially constant across all of the grating periodicities. Fitting of the spectral peaks using Gaussian and Lorentzian lineshapes showed that the emission for quantum dots on bare glass corresponded more closely with a Gaussian while the shifted peaks were more Lorentzian in nature. This behavior is not unexpected and it has been demonstrated in other systems that modification of the emitter behavior can lead to significant alteration of the shape of the emission spectrum [97]. From the extracted data it appears that there may be some small variation in the peak width. However, as this variation is less than 1nm it may be considered to be effectively constant. Based on the results of these measurements along with observations of the fluorescence lifetime it is evident that when comparing quantum dots on bare glass or unpatterned PMMA and the dielectric gratings some degree of emission enhancement is present and results in modification of the emission lifetime along with shifting of the spectral peak. Once on the grating, there is little clear evidence that significant modification of the emission lifetime or spectral response can be strongly correlated to the observed variations in emission intensity. These results support the conclusion that enhanced emission effects do not provide significant contributions to the emission of quantum dots on these samples. As a result, we conclude that the fluorescence enhancement observed on these samples can be attributed to enhanced absorption from surface plasmons excited by the grating geometry along with field concentrations from the dielectric gratings.

7 Conclusions

The results and analysis in this study have demonstrated that enhancement of fluorescence from QDs can be achieved by using grating coupled SPPs excited at the surface of a gold film. Experimental investigations have shown that dispersal of QDs may be performed by deposition of a composite particle-containing film or through direct deposition of QDs onto the film surface and provide a comparison of performance between the two techniques. Observations have also been made showing that successful adhesion of particles to the grating surface are dependent on the timing of their deposition, although this problem can be alleviated through chemical modification of the surface. Through the use of SEM and AFM imagery of different regions on the surface, it has been determined that QDs deposited prior to electron beam patterning remain on the surface after exposure and development of structures. By taking advantage of this finding, a study of the relation between the observed enhanced fluorescence signal and the physical parameters of the grating structure was made possible. The results demonstrated that an optimal duty cycle for maximum emission was observed as well as the presence of an apparent threshold in film thickness for the enhancement effect to occur. Finally, further investigation of quantum dot behavior using time correlated single photon counting techniques, supported by FDTD simulations, along with spectral measurements have been used to attribute the fundamental origins of the fluorescence increase to enhanced absorption from strong fields near the interface. Based on these findings the fundamental properties of fluorescence enhancement of quantum dots over dielectric gratings on gold films have been presented and the conditions under which such enhancement can

be practically obtained determined. In spite of all this much work remains to be done in the field of fluorescence on surface plasmon supporting structures. The work presented here represents an in-depth study of a single grating geometry and surface structure configuration which is but one of several already considered in the literature. Aside from fundamental studies of the enhancement phenomena studies regarding details for the application of this technique to practical systems such as biodetection or fluorescence imaging currently remain unexplored. Additional results, not presented here, have also shown that quantum dots deposited onto similar surfaces patterned with various structures can function as probes for examining surface plasmon coupling and propagation behavior which could provide an alternative to near field scanning. The use of a material system containing PMMA and gold, both substrates with well-known surface chemistry, means that these samples could be suitable for direct integration into fluorescence imaging systems for detection of target analytes.

8 Bibliography

[1] R.H. Ritchie, "Plasma Losses by Fast Electrons in Thin Films," *Physical Review*, vol. 106, pp. 874-881, 1957.

[2] M.K. Hossain et al., "Surface Plasmon Excitation and Surface-Enhanced Raman Scattering Using Two-Dimensionally Close-Packed Gold Nanoparticles," *J. Phys. Chem. C*, vol. 113, no. 27, pp. 11689-11694, 2009.

[3] J.C. Tsang, J.R. Kirtley, and J.A. Bradley, "Surface-Enhanced Raman Spectroscopy and Surface Plasmons," *Phys. Rev. Lett.*, vol. 43, pp. 772-775, 1979.

[4] A. Campion and P. Kambhampati, "Surface-Enhanced Raman Scattering," *Chem. Soc. Rev.*, pp. 241-250, 1998.

[5] A. Merlen, V. Gadenne, J. Romann, L. Patrone, and J.C. Valmalette, "Surface enhanced Raman spectroscopy of organic molecules deposited on gold sputtered substrates," *Nanotechnology*, vol. 20, 2009.

[6] I. Smolyaninov, Y.J. Hung, and C.C. Davis, "Magnifying Superlens in the Visible Frequency Range," *Science*, vol. 315, pp. 1699-1701, 2007.

[7] J.A. Dionne, E. Verhagen, A. Polman, and H.A. Atwatr, "Are negative index materials achievable with surface plasmon waveguides? A case study of three plasmonic geometries.," *Optics Express*, vol. 16, pp. 19001-19017, 2008.

[8] L. Martin-Moreno, F.J. Garcia Vidal, H.J. Lezec, A. Degiron, and T. Ebbesen, "Theory of highly directional emission from a single subwavelength aperture surrounded by surface corrugations," *Phys. Rev. Lett.*, vol. 90, 2003.

[9] T.W. Ebbesen, H.J. Lezec, H.F. Ghaemi, T. Thio, and P.A. Wolff, "Extraordinary optical transmission through sub-wavelength hole arrays," *Nature*, vol. 391, pp. 667-669, 1998.

[10] T. Thio, K.M. Pellerin, R.A. Linke, H.J. Lezec, and T.W. Ebbesen, "Enhanced light transmission through a single subwavelength aperture," *Opt. Lett.*, vol. 26, pp. 1972-1974, 2001.

[11] A.V. Andreev, M.M. Nazarov, J.R. Prudnikov, A.P. Shkurinov, and P. Masselin, "Noncollinear excitation of surface electromagnetic waves: Enhancement of nonlinear optical surface response," *Physical Review B*, vol. 69, 2004.

[12] V.B. Svetovoy, P.J. van Zwol, G. Palasantzas, and J. Th. M. De Hosson, "Optical Properties of gold films and the Casimir force," *Phys. Rev. B*, vol. 77, 2008.

[13] P.B. Johnson and Christy R.W., "Optical Constants of the Noble Metals," *Phys. Rev. B*, vol. 6, no. 12, pp. 4370-4379, 1972.

[14] E. D. Palik, *Handbook of Optical Constants of Solids*. New York, NY: Academic Press, 1998.

[15] Robert C. Weast, Ed., *Handbook of Chemistry and Physics*. Boca Raton: CRC, 1988.

[16] W. Knoll, Winspall, Max Planck Institute for Polymer Research, Material Science Group; Mainz, Germany. http://www.mpip-mainz.mpg.de.

[17] J. Homola, S.S. Yee, and G. Gauglitz, "Surface plasmon resonance sensors: review," *Sensors and Actuators B - Chemical*, vol. 54, no. 1-2, pp. 3-15, 1999.

[18] J. Homola, "Present and future of surface plasmon resonance biosensors," *Analytical and Bioanalytical Chemistry*, vol. 377, no. 3, pp. 528-539, 2003.

[19] H. Raether, *Surface Plasmons on Smooth and Rough Surfaces and on Gratings*. New York: Springer, 1988.

[20] H.L. Offerhaus, B. ven den Bergen, F.B. Segerink, J.P. Korterik, and N.F. van Hulst, "Creating Focused Plasmons by Noncollinear Phasematching on Functional Gratings," *Nano Letters*, vol. 5, no. 11, pp. 2144-2148, 2005.

[21] K. Okamoto, A. Scherer, and Y. Kawakami, "Surface plasmon enhanced light emission from semiconductor materials," *Phys. Stat. Sol.*, vol. 5, no. 9, pp. 2822-2824, 2008.

[22] K. Okamoto, S. Vyawahare, and A. Scherer, "Surface-plasmon enhanced bright emission from CdSe quantum-dot nanocrystals," *J. Opt. Soc. Am. B*, vol. 28, no. 8, pp. 1674-1678, 2006.

[23] P.P. Pompa et al., "Metal-enhanced fluorescence of colloidal nanocrystals with nanoscale control," *Nature Nanotechnology*, vol. 1, pp. 126-130, 2006.

[24] S.S. Kim, S.I. Na, J. Jo, D.Y. Kim, and Y.C. Nah, "Plasmon enhanced performance of organic solar cells using electrodeposited Ag nanoparticles," *Applied Physics Letters*, vol. 93, no. 7, 2008.

[25] R.A., White, J. Pala, E. Barnard, J. Liu, and M.L. Brongersma, "Design of Plasmonic Thin-Film Solar Cells with Broadband Absorption Enhancements," *Advanced Materials*, vol. 21, no. 34, pp. 3504-3509, 2009.

[26] S. Madaan. (2007) nanoHUB.org. [Online]. http://nanohub.org/resources/2520

[27] C.B. Murray, D.J. Norris, and M.G. Bawendi, "Synthesis and characterization of nearly monodisperse CdE (E=S,Se,Te) semiconductor nanocrystallites," *J. Am. Chem. Soc.*, vol. 115, no. 19, pp. 8706-8715, 1993.

[28] B.O. Dabbousi et al., "(CdSe)ZnS Core-Shell Quantum Dots: Synthesis and Characterization of a Size Series of Highly Luminescent Nanocrystallites," *J Phys. Chem. B*, vol. 101, p. 94639475, 1997.

[29] S.W. Lee, C. Mai, C.E. Flynn, and A.M. Belcher, "Ordering of quantum dots using genetically engineered viruses," *Science*, vol. 296, pp. 892-895, 2002.

[30] L. Qu and X. Peng, "Control of photoluminescence properties of CdSe nanocrystals in growth," *J. Am. Chem. Soc.*, vol. 124, pp. 2049-2055, 2002.

[31] L. Manna, W.D. Yang, J. Wickham, E. Scher, et al. X.G. Peng, "Shape control of CdSe nanocrystals," *Nature*, vol. 404, pp. 59-61, 2000.

[32] L. Manna, E.C. Scher, and A.P. Alivisatos, "Synthesis of soluble and processable rod-, arrow-, teardrop-, and tetrapod-shaped CdSe nanocrystals.," *J. Am. Chem. Soc.*, vol. 122, pp. 12700-12706.

[33] M.A. Hines and P. Guyot-Sionnest, "Synthesis and characterization of strongly luminescing ZnS-capped CdSe nanocrystals," *J. PHys. Chem.*, vol. 100, pp. 468-471, 1996.

[34] A.L. Efros and A.L. Efros, "Intersubband absorption of light in a semiconductor sphere," *Soviet Physics - Semiconductors*, vol. 16, pp. 772-775.

[35] D.J. Norris, A. Sacra, C.B. Murray, and M.G. Bawendi, "Measurement of the size dependent hole spectrum in CdSe quantum dots," *Phys. Rev. Lett.*, vol. 72, pp. 2612-2615, 1994.

[36] A.I. Ekimov, F. Hache, M.C. Schanne-Klein, D. Ricard, and C. Flytzanis, "Absorption and intensity-dependent photoluminescence measurements on CdSe quantum dots: assignment of the first electronic transitions," *J. Opt. Soc. Am. B*, vol. 75, pp. 3728-3731, 1993.

[37] V.I. Klimov, D.W. McBranch, C.A. Leatherdale, and M.G. Bawendi, "Electron and hole relaxation pathways in semiconductor quantum dots," *Physical Review B*, vol. 60, no. 19, pp. 740-749, 1999.

[38] M. Nimral et al., "Observation of the dark excitons in CdSe quantum dots.," *Phys. Rev. Lett.*, vol. 75, pp. 3728-3731, 1995.

[39] A.L. Efros and M. Rosen, "Band-edge exciton in quantum dots of semiconductors with a degenerate valence band: dark and bright exciton states," *Phys. Rev. B*, vol. 54, pp. 4843-4856, 1996.

[40] S.A. Crooker, T. Barrick, J.A. Hollingsworth, and V.I. Klimov, "Multiple temperature regimes of radiative decay in CdSe nanocrystal quantum dots: intrinsic limits of the dark-exciton lifetime," *Applied Physics Letters*, vol. 82, pp. 2793-2795, 2003.

[41] P. Tamarat, B. Lounis O. Labeau, "Temperature Dependence of the Luminescence Lifetime of Single CdSe/ZnS Quantum Dots," *Physical Review Letters*, vol. 90, no. 25, 2003.

[42] V.I. Klimov, A.A. Mikhailovsky, D.W. McBranch, C.A. Leatherdale, and M.G. Bawendi, "Quantization of Multiparticle Auger Rates in Semiconductor Quantum Dots," *Science*, vol. 287, pp. 1011-1013, 2000.

[43] Y. Louyer, L. Biadala, Ph. Tamarat, and B. Lounis, "Spectroscopy of neutral and charged exciton states in single CdSe/ZnS nanocrystals," *Applied Physics Letters*, vol. 96, 2010.

[44] E. Faulques, F. Massuyeau, Q. Wang, D.K. Seo, and S. Jobic, "Mapping emissive channels of quantum dots: Influence of size and environment on energy transfer in the time domain," *Applied Physics Letters*, vol. 97, 2010.

[45] W.Z. Lee et al., "Recombination dynamics of luminescence in colloidal CdSe/ZnS quantum dots," *Nanotechnology*, vol. 17, pp. 1517-1521, 2005.

[46] X. Wang, L. Qu, J. Zhang, X. Peng, and M. Xiao, "Surface-Related Emission in Highly Luminescent CdSe Quantum Dots," *Nano Letters*, vol. 3, no. 8, pp. 1103-1106, 2003.

[47] M.G. Bawendi, P.J. Carroll, W.L. Wilson, and L.E. Brus, "Luminescence properties of CdSe quantum crystallites: Resonance between interior and surface localized states," *J. Chem. PHys.*, vol. 2, pp. 946-954, 1992.

[48] G.W. Shu et al., "Photoluminescence of Colloidal CdSe/ZnS Quantum Dots Under Oxygen Atmosphere," *IEEE Transactions on Nanotechnology*, vol. 4, no. 5, pp. 632-636, 2005.

[49] P. Guyot-Sionnest, B. Wehrenberg, and D. Yu, "Intraband relaxation in CdSe nanocrystals and the strong influence of the surface ligands," *The Journal of Chemical Physics*, vol. 123, 2005.

[50] S.A. Empedocles, R. Neuhauser, K. Shimizu, and M.G. Bawendi, "Photoluminescence from Single Semiconductor Nanostructures," *Advanced Materials*, vol. 11, no. 15, pp. 1243-1256, 1999.

[51] A. Javier, D. Magana, T. Jennings, and G.F. Strouse, "Nanosecond exciton recombination dynamics in colloidal CdSe quantum dots under ambient conditions," *Applied Physics Letters*, vol. 83, no. 7, pp. 1423-1425, 2003.

[52] B.R. Fisher, H. Eisler, N.E. Scott, and M.G. Bawendi, "Emission Intensity Dependence and Single-Exponential Behavior in Single Colloidal Quantum Dot Fluorescence Lifetimes," *J. PHys. Chem. B*, vol. 108, 143-148 2004.

[53] U. Resch-Genger, M. Grabolle, S. Cavaliere-Jaricot, R. Nitschke, and T. Nann, "Quantum dots versus organic dyes as fluorescent labels," *Nature Methods*, vol. 5, no. 9, pp. 763-775, 2008.

[54] Graz University of Technology. Fluorophores.org.

[55] www.nn-labs.com.

[56] X. Wu et al., "Immunofluorescent labeling of cancer marker Her2 and other cellular argets with semiconductor quantum dots," *Nature Biotechnology*, vol. 21, pp. 41-46, 2003.

[57] W.W. Yu, L. Qu, W. Guo, and X. Peng, "Experimental Determination of the Extinction Coefficient of CdTe, CdSe, and CdS Nanocrystals," *Chem. Mater.*, vol. 15, pp. 2854-2860, 2003.

[58] I.L. Medintz, H.T. Uyeda, E.R. Goldman, and H. Mattoussi, "Quantum dot bioconjugates for imaging, labelling and sensing," *Nature Materials*, vol. 4, pp. 435-446, 2005.

[59] Y.J. Hung, I.I. Smolyaninov, C.C. Davis, and H.C. Wu, "Fluorescence enhancement by surface gratings," *Optics Express*, vol. 14, pp. 10825-10830, 2006.

[60] W.L. Barnes, "Topical Review - Fluorescence near interfaces: the role of photonic mode density," *Journal of Mondern Optics*, vol. 45, pp. 661-699, 1998.

[61] R. Ruppin and O.J.F. Martin, "Lifetime of an emitting dipole near various types of interfaces including magnetic and negative refractive materials," *Journal of Chemical Physics*, vol. 121, no. 22, pp. 11358-11361, 2004.

[62] W. Lukosz and R.E. Kunz, "Fluorescence Lifetime of Magnetic and Electric Dipoles Near a Dielectric Interface," *Optics Communications*, vol. 20, no. 2, pp. 195-198, 1977.

[63] W. Lukosz and R.E. Kunz, "Light emission by magnetic and electric dipoles close to a plane interface. I. Total radiated power," *J. Opt. Soc. Am.*, vol. 67, no. 12, pp. 1607-1615, 1977.

[64] W. Lukosz and R.E. Kunz, "Light emission by magnetic and electric dipoles cloe to a plane dielectric interface. II. Radiation patterns of perpendicular oriented dipoles," *J. Opt. Soc. Am.*, vol. 67, no. 12, pp. 1615-1619, 1977.

[65] W. Lukosz, "Light emission by magnetic and electric dipoles close to a plane dielectric interface. III. Radiation patterns of dipoles with arbitrary orientation," *J. Opt. Soc. Am.*, vol. 69, no. 11, pp. 1495-1503.

[66] E. Fermi, "Quantum Theory of Radiation," *Rev. Mod. Phys.*, vol. 4, p. 87, 1932.

[67] E.M. Purcell, "Spontaneous Emission Probabilities at Radio Frequencies," *Phys. Rev.*, vol. 69, p. 681, 1946.

[68] K.H. Drexhage, "Influence of a Dielectric Interface on Fluorescence Decay Time," *J. Lumin*, vol. 1, no. 2, pp. 693-701, 1970.

[69] K.H. Drexhage, M. Fleck, F.P. Schafer, and W. Sperling, *Ber. Bunsenges. phys. Chem.*, vol. 20, p. 1179, 1966.

[70] K.H. Drexhage, H. Kuhn, and F.P. Schafer, *Ber. Bunsenges. phys. Chem.*, vol. 72, p. 329, 1968.

[71] K.H. Drexhage, *Sci. Am.*, vol. 222, p. 108, 1970.

[72] K.H. Drexhage, "Interaction of Light with Momomolecular Dye Layers," *Progress in Optics*, vol. 12, p. 198, 1974.

[73] S.C. Kitson, W.L. Barnes, and J.R. Sambles, "Photoluminescence from dye molecules on silver gratings," *Optics Communications*, vol. 122, pp. 147-154, 1996.

[74] R.M. Amos and W.L. Barnes, "Modification of the spontaneous emission rate of Eu3+ ions close to a thin metal mirror," *Physical Review B*, vol. 55, no. 11, pp. 7249-7254, 1997.

[75] P.T. Worthing, R.M. Amos, and W.L. Barnes, "Modification of the spontaneous emission rate of Eu3+ ions embedded within a dielectric layer above a silver mirror," *Phys. Rev. A*, vol. 59, no. 1, pp. 865-872, 1999.

[76] W. Lukosz and M. Meier, "Lifetimes and radiation patterns of luminescent centers close to a thin metal film," *Optics Letters*, vol. 6, no. 5, pp. 251-253, 1981.

[77] R.e. Kunz and W. Lukosz, "Changes in fluorescence lifetimes induced by variable optical environments," *Phys. Rev. B*, vol. 21, no. 10, pp. 4814-4828, 1980.

[78] Lumerical Solutions, Inc., FDTD Solutions, http://www.lumerical.com.

[79] G. Sun and J.B. Khurgin, "Plasmon Enhancement of Luminescence by Metal Nanoparticles," *IEEE Journal of Selected Topics in Quantum Electronics*, vol. 17, no. 1, pp. 110-118, 2011.

[80] G. Sun, J.B. Khurgin, and R.A. Soref, "Practicable enhancement of spontaneous emission using surface plasmons," *Applied PHysics Letters*, vol. 90, 2007.

[81] G. Sun, J.B. Khurgin, and R.A. Soref, "Practical enhancement of photoluminescence by metal nanoparticles," *Applied Physics Letters*, vol. 94, 2009.

[82] J.B. Khurgin, G. Sun, and R.A. Soref, "Practical limits of absorption enhancement near metal nanoparticles," *Applied Physics Letters*, vol. 94, 2009.

[83] A.V. Zayats, I.I. Smolyaninov, and A.A. Maradudin, "Nano-optics of surface plasmon polaritons," vol. 408, pp. 131-314, 2005.

[84] J.R. Lackowicz, "Radiative Decay Engineering: Biophysical and Biomedical Applications," *Anal. Biochem.*, vol. 298, pp. 1-24, 2001.

[85] J.R. Lackowicz, "Radiative Decay Engineering 3: Surface plasmon-coupled directional emission," *Anal. Biochem.*, vol. 324, pp. 153-169, 2004.

[86] I. Gryczynski, J. Malicka, Z. Gryczynski, and J.R. Lackowicz, "Radiative Decay Engineering 4: Experimental studies of surface plasmon-coupled directional emission.," *Anal. Biochem.*, vol. 324, pp. 170-182, 2004.

[87] I. Gryczynski et al., "Surface-Plasmon-Coupled Emission of Quantum Dots," *J. Phys. Chem. B*, vol. 109, pp. 1088-1093, 2005.

[88] J.H. Song, T. Atay, S. Shi, H. Urabe, and A.V. Nurmikko, "Large Enhancement of Fluorescence Efficiency from CdSe/ZnS Quantum Dots Induced by Resonant Coupling to Spatially Controlled Surface Plasmons," *Nano Letters*, vol. 5, pp. 1557-1561, 2005.

[89] O. Stranik, H.M. McEvoy, C. McDonagh, and B.D. MacCraith, "Plasmonic enhancement of fluorescence for sensor applications," *Sens. Actuators B*, vol. 107, pp. 148-153, 2005.

[90] J.R. Sambles, G.W. Bradbery, and F. Yang, "Optical excitation of surface plasmons: an introduction," *Contemporary Physics*, vol. 32, pp. 173-183, 1991.

[91] K. Tawa et al., "Optical microscope observation of fluorescence enhanced by grating-coupled surface plasmon resonance," *Optics Express*, vol. 16, pp. 9781-9790, 2008.

[92] V. Pilla, L.P., Munin, E. Avles, and M.T.T. Pacheco, "Radiative quantum efficiency of CdSe/ZnS quantum dots suspended in different solvents," *Opt. Commun.*, vol. 280, pp. 225-229, 2007.

[93] P. Klapetek, D. Necas, and C. Anderson. (2004-2009) Gwyddion User Guide. Online http://gwyddion.net.

[94] C. Rhodes et al., "Surface plasmon resonance in conducting metal oxides," *J. Appl. Phys.*, vol. 100, 2006.

[95] J.D. Jackson, *Classical Electrodynamics*, 3rd ed.: John Wiley and Sons, Inc., 1999.

[96] A.A. Mikhailovsky, D.W. McBranch, C.A. Leatherdale, M.G. Bawendi V.I. Klimov, "Quantization of Multiparticle Auger Rates in Semiconductor Quantum Dots," *Science*, vol. 287, pp. 1011-1013, 2000.

[97] E. C. Le Ru et al., "Mechanisms of Spectral Profile Modification in Surface-Enhanced Fluorescence," *J. Phys. Chem. C Letters*, vol. 111, pp. 16076-16079, 2007.

[98] B. Hecht L. Novotny, *Principles of Nano-Optics*. New York, NY: Cambridge University Press, 2006.

[99] C.A. Ward, R.J. Bell, R.W. Alexander, and G.S. Kovener, "Surface Electromagnetic Waves on Metals and Polar Insulators: Some Comments," *Applied Optics*, vol. 13, 1974.

[100] O. Labeau, P. Tamarat, and B. Lounis, "Temperature dependence of the luminescence lifetime of single CdSe/ZnS quantum dots," *Phys. Rev. Lett.*, vol. 90, 2003.

[101] V.I. Klimov, "Spectral and Dynamical Properties of Multiexcitons in Semiconductor Nanocrystals," *Annu. Rev. Phys. Chem.*, vol. 58, pp. 653-673, 2007.

[102] A.P. Alivisatos, W. Gu, and C. Larabell, "Quantum Dots as Cellular Probes," *Annu. Rev. Biomed. Eng.*, vol. 7, pp. 55-76, 2005.

[103] V. M. Agranovich and D. L. Mills, Eds., *Surface Polaritons*. Amsterdam: North-Holland, 1982.

9 Publications

Hwang, E., Smolyaninov, I.I., Davis, C.C. “Surface Plasmon Polariton Enhanced Fluorescence from Quantum Dots on Nanostructured Metal Surfaces”, Nano Letters, vol. 10, no. 3, pp. 813-820 (2010)

Ehren Hwang; Christopher C. Davis; Igor I. Smolyaninov ``Surface plasmon polariton enhanced fluorescence from quantum dots on nanostructured metal surfaces," SPIE Proceedings vol.7395, Satoshi Kawata; Vladimir M. Shalaev; Din Ping Tsai, Eds., 2009.

Yu-Ju Hung, Ehren Hwang, and Igor Smolyaninov, ``Fluorescence Enhancement by Surface Gratings," paper presented at the 2007 International Semiconductor Device Research Symposium (ISDRS), December 12-14, 2007, College Park, Maryland.

Ehren Hwang, Igor I. Smolyaninov and Christopher C. Davis, “Surface plasmon polariton enhanced fluorescence from quantum dots on nanostructured metal surfaces,” paper presented at CLEO, Baltimore, June 2-4, 2009.

Ehren Hwang, Igor I. Smolyaninov, and Christopher C. Davis, “Surface Plasmon Polariton Enhanced Fluorescence from Quantum Dots on Nanostructured Metal Surfaces,” paper presented at ISDRS, College Park, Maryland, December 2009.